(12) INTERNATIONAL APPLICATION PUBLISHED UNDER THE PATENT COOPERATION TREATY (PCT)

(19) World Intellectual Property Organization
International Bureau

(43) International Publication Date
19 December 2024 (19.12.2024)

WIPO | PCT

(10) International Publication Number
WO 2024/259099 A2

(51) International Patent Classification:
Not classified

(21) International Application Number:
PCT/US2024/033807

(22) International Filing Date:
13 June 2024 (13.06.2024)

(25) Filing Language: English

(26) Publication Language: English

(30) Priority Data:
63/472,667 13 June 2023 (13.06.2023) US

(71) Applicant: **TRUSTEES OF DARTMOUTH COLLEGE** [US/US]; 11 Rope Ferry Road, Room 6210, Hanover, NH 03755 (US).

(72) Inventors: **SCHEIDELER, William, J .**; 27 Rio Vista, Unit 301, West Lebanon, NH 03784 (US). **TIWARI, Anand, P .**; 20 Wolf Road, Apt. 122, Lebanon, NH 03766 (US).

(74) Agent: **ALFANO, Gabriella R.**; Hodgson Russ LLP, 140 Pearl Street, Suite 100, Buffalo, New York 14202-4040 (US).

(81) Designated States *(unless otherwise indicated, for every kind of national protection available)*: AE, AG, AL, AM, AO, AT, AU, AZ, BA, BB, BG, BH, BN, BR, BW, BY, BZ, CA, CH, CL, CN, CO, CR, CU, CV, CZ, DE, DJ, DK, DM, DO, DZ, EC, EE, EG, ES, FI, GB, GD, GE, GH, GM, GT, HN, HR, HU, ID, IL, IN, IQ, IR, IS, IT, JM, JO, JP, KE, KG, KH, KN, KP, KR, KW, KZ, LA, LC, LK, LR, LS, LU, LY, MA, MD, MG, MK, MN, MU, MW, MX, MY, MZ, NA, NG, NI, NO, NZ, OM, PA, PE, PG, PH, PL, PT, QA, RO, RS, RU, RW, SA, SC, SD, SE, SG, SK, SL, ST, SV, SY, TH, TJ, TM, TN, TR, TT, TZ, UA, UG, US, UZ, VC, VN, WS, ZA, ZM, ZW.

(84) Designated States *(unless otherwise indicated, for every kind of regional protection available)*: ARIPO (BW, CV, GH, GM, KE, LR, LS, MW, MZ, NA, RW, SC, SD, SL, ST, SZ, TZ, UG, ZM, ZW), Eurasian (AM, AZ, BY, KG, KZ, RU, TJ, TM), European (AL, AT, BE, BG, CH, CY, CZ, DE, DK, EE, ES, FI, FR, GB, GR, HR, HU, IE, IS, IT, LT, LU, LV, MC, ME, MK, MT, NL, NO, PL, PT, RO, RS, SE, SI, SK, SM, TR), OAPI (BF, BJ, CF, CG, CI, CM, GA, GN, GQ, GW, KM, ML, MR, NE, SN, TD, TG).

Published:
— *without international search report and to be republished upon receipt of that report (Rule 48.2(g))*

WO 2024/259099 A2

(54) Title: NANOPOROUS THREE-DIMENSIONAL TRANSITION METAL OXIDE AND CARBON COMPOSITE ELECTRODES FOR EFFICIENT ELECTROCATALYSIS

(57) Abstract: An electrocatalyst electrode having a strut lattice structure fabricated of a polymer and a composite disposed on the strut lattice structure that includes at least one transition metal oxide, which may include copper oxide, cobalt oxide, or nickel oxide. The composite and the strut lattice structure are 3D and free-standing. The electrocatalyst electrode includes one or more pores that are vertically aligned to form channels and to facilitate bubble release. The composite is used for alkaline hydrogen evolution reaction (HER) and oxygen evolution reaction (OER).

NANOPOROUS THREE-DIMENSIONAL TRANSITION METAL OXIDE AND CARBON COMPOSITE ELECTRODES FOR EFFICIENT ELECTROCATALYSIS

CROSS REFERENCE TO RELATED APPLICATIONS

[0001] The present application claims priority to and benefit of U.S. Provisional Patent Application No. 63/472,667, filed June 13, 2023, the entire disclosure of which is incorporated herein by reference.

FIELD OF THE DISCLOSURE

[0002] This disclosure relates to electrodes.

BACKGROUND OF THE DISCLOSURE

[0003] Alkaline water electrolysis (AWE) offers a promising pathway for water splitting, presenting significant potential for the development of sustainable electrocatalysts in energy devices. Furthermore, the advancement of platinum group metal (PGM)-free electrocatalysts holds promise for substantial cost reductions in large-scale applications. Nevertheless, these PGM-free electrocatalysts currently face challenges regarding their catalytic efficiency. To address this challenge, extensive studies have explored transition metal derivatives such as transition metal phosphides, transition metal nitrides, transition metal alloys, and transition metal oxides because of their moderate capacity to adsorb hydrogen, thereby enhancing kinetics. Among these derivatives, transition metal oxides (TMO) show promise owing to their robust stability in alkaline environments. However, due to their low electrical conductivity and poor kinetics, there persists a substantial disparity in their water splitting performance when compared to that of PGMs.

[0004] Several nanostructure-scale approaches have been proposed to enhance the water-splitting activity of TMO. These approaches include altering the electronic structure through the introduction of heteroatoms, inducing chemical defects via oxygen vacancies, and increasing porosity through synthesizing TMO with diverse nanostructures to enlarge the active surface area. However, nanostructuring approaches encounter practical limitations as they require casting nanoparticles onto current collectors using polymeric binders such as polytetrafluoroethylene or Nafion, leading to increased resistance, blocked active sites, and hindered mass transport.

[0005] Three-dimensional (3D) electrocatalyst design has become a focus of efforts to maximize utilization of active sites through mass-transport engineering of the liquid phase electrolyte and gas phase bubble production. A goal of this strategy is to provide an inexpensive, scalable, and highly effective electrocatalyst with good activity. Various wet chemical growth techniques enable the deposition nanostructures on 3D frameworks, such as nanoleaflets, nanosticks formed from spheres, and nanowires for efficient water splitting performance. However, the limited adhesive force between the catalytically active materials and the 3D substrate results in easy detachment from the substrate during prolonged, high-current electrocatalysis. This limitation restricts their effective performance to lower current densities, rendering them inadequate for meeting the demands of industrial water splitting, which commonly operates at higher current densities. Additionally, the gas bubbles generated during water splitting on these 3D structures can obstruct a significant number of catalytically active sites, leading to an increase in the device resistance and limited mass transfer, impacting the overall efficiency of water splitting. The mesoscale architecture of the electrode can be important to the overall efficiency of new earth-abundant electrocatalysts for large-scale water splitting.

[0006] The sluggish kinetics of electrocatalysts in alkaline media cause stability issues and issues of low active site density, restricting the conversion of renewably generated electricity into hydrogen. Synergistic efforts with free-standing 3D nanoporous structuring, heterostructuring, and atomic doping/defecting of active materials may be an effective way to improve the kinetics and resolve stability issues. Atomic doping and introduction of defects may increase the active site density through lattice strain and free-standing 3D structures may provide an increased number of reaction sites to ensure higher stability by quickly removing the adsorbed atomic hydrogen at the catalytic active sites.

[0007] Therefore, new materials and techniques are needed.

BRIEF SUMMARY OF THE DISCLOSURE

[0008] The present disclosure provides an electrocatalyst electrode including a strut lattice structure fabricated of a polymer and a composite disposed on the strut lattice structure that includes at least one transition metal oxide. The composite and the strut lattice structure may be 3D and free-standing.

[0009] In embodiments of the present disclosure, the at least one transition metal oxide may include copper oxide, cobalt oxide, nickel oxide, titanium oxide, zinc oxide, manganese oxide, molybdenum oxide, tungsten oxide, iron oxide, or vanadium oxide.

[0010] In embodiments of the present disclosure, the composite may include a mixture of one or more of the at least one transition metal oxide.

[0011] In embodiments of the present disclosure, the composite may define one or more pores having pore sizes from 10 μm to 1 mm.

[0012] In embodiments of the present disclosure, the one or more pores may be vertically aligned to form channels.

[0013] In embodiments of the present disclosure, the one or more pores may be configured to facilitate bubble release.

[0014] In embodiments of the present disclosure, the strut lattice structure may have an octet, body-centered cubic, simple cubic, or Kelvin cell lattice.

[0015] In embodiments of the present disclosure, wherein the composite may be a coating on the strut lattice structure.

[0016] In embodiments of the present disclosure, the composite may be used for alkaline hydrogen evolution reaction (HER) and oxygen evolution reaction (OER).

[0017] In embodiments of the present disclosure, the HER may demonstrate an overpotential of 155 mV at a current density of 10 mA/cm2 and a Tafel slope of 134 mV/dec.

[0018] In embodiments of the present disclosure, the OER may demonstrate an overpotential of 1.42 V at a current density of 10 mA/cm2 and a Tafel slope of 55 mV/dec.

[0019] The present disclosure further provides a method including stereolithography 3D printing a free-standing strut lattice structure with a periodic pore structure, infusing the strut lattice structure with a metal salt by soaking the strut lattice structure in a concentrated solution of the metal salt dissolved in water, and annealing the strut lattice structure at a temperature from 400 °C to 700 °C. The strut lattice structure may be fabricated of a polymer.

[0020] In embodiments of the present disclosure, the strut lattice structure may have an octet, body-centered cubic, simple cubic, or Kelvin cell lattice.

[0021] In embodiments of the present disclosure, one or more pores in the periodic pore structure may have dimensions from 10 μm to 1 mm.

[0022] In embodiments of the present disclosure, a duration of the infusing may be from 24 to 96 hours.

[0023] In embodiments of the present disclosure, the infusing may occur at a temperature from 60 °C to 100 °C.

[0024] In embodiments of the present disclosure, the annealing may be configured to convert the strut lattice structure to a 3D lattice with graphitic or glassy carbon and a metal/metal oxide coating.

[0025] In embodiments of the present disclosure, oxygen stoichiometries and surface morphologies of the strut lattice structure may be modified by changing the temperature and a time of the annealing.

[0026] In embodiments of the present disclosure, the metal/metal oxide coating may include at least one transition metal oxide, wherein the at least one transition metal oxide comprises copper oxide, cobalt oxide, nickel oxide, titanium oxide, zinc oxide, manganese oxide, molybdenum oxide, tungsten oxide, iron oxide, or vanadium oxide.

[0027] In embodiments of the present disclosure, the metal/metal oxide coating may include a mixture of one or more of the at least one transition metal oxide.

DESCRIPTION OF THE DRAWINGS

[0028] For a fuller understanding of the nature and objects of the disclosure, reference should be made to the following detailed description taken in conjunction with the accompanying figures.

[0029] FIG. 1 is a chart showing overpotentials versus Tafel slope for an embodiment disclosed herein and for previous composites.

[0030] FIGS. 2(a)-2(i) display morphological characterization of different 3D-nanoporous composites at 400 °C, wherein 2(a)-2(c) display SEM images of reduced cobalt oxides and carbon composites, 2(d)-2(f) display SEM images of reduced copper oxides and carbon composites, and 2(g)-2(i) display SEM images of reduced nickel oxides and carbon composites.

[0031] FIGS. 3(a)-3(i) display morphological characterization of different 3D-nanoporous composites at 450 °C, wherein 3(a)-3(c) display SEM images of reduced cobalt oxides and carbon

composites, 3(d)-3(f) display SEM images of reduced copper oxides and carbon composites, and 3(g)-3(i) display SEM images of reduced nickel oxides and carbon composites.

[0032] FIGS. 4(a)-4(i) display morphological characterization of different 3D-nanoporous composites at 700 °C, wherein 4(a)-4(c) display SEM images of reduced cobalt oxides and carbon composites, 4(d)-4(f) display SEM images of reduced copper oxides and carbon composites, and 4(g)-4(i) display SEM images of reduced nickel oxides and carbon composites.

[0033] FIGS. 5(a)-5(c) shows XRD analysis characterizing crystal structures of all products and an effect of variable thermal annealing step temperatures.

[0034] FIGS. 6(a)-6(c) display graphical representation of the electrocatalytic performance for OER. 6(a) displays LSV curves of 3D-nanoporous composites synthesized at 700 °C with the scan rate of 10 mV/sec. 6(b) displays Tafel slopes of 3D-nanoporous composites. 6(c) displays Nyquist plot for 3D-nanoporous composites. All electrochemical experiments were performed in 1.0 M KOH.

[0035] FIGS. 7(a)-7(c) display graphical representation of electrocatalytic performance for HER. 7(a) displays LSV curves of 3D-nanoporous composites synthesized at 450 °C with the scan rate of 10 mV/sec. 7(b) displays LSV curves of 3D-nanoporous composites synthesized at 400 °C with the scan rate of 10 mV/sec. 7(c) displays Nyquist plot for 3D-nanoporous composites at 150 mV. All electrochemical experiments were performed in 1.0 M KOH.

[0036] FIGS. 8(a)-8(o) display fabrication and microstructural characterization of the present disclosure. 8(a) displays a graphical scheme of the micro stereolithography (SLA) printing. 8(b) displays an SLA-printed large-scale production of 3D electrodes comprised of microlattices. 8(c) displays a schematic of polymer infusion additive manufacturing (PIAM) process, disclosed herein. 3D polymer scaffolds are converted to transition metal and transition metal oxide interfaces on carbon 3D microlattices. The optical images of the PIAM process for microlattices are shown vertically above their respective schematics. 8(d)-8(f) display SEM images of Cu/CuO_x on carbon and 8(g)-8(i) display SEM images of Co/CoO_x on carbon microlattices. 8(j)-8(l) display EDS elemental mapping of Cu/CuO_x on carbon and 8(m)-8(o) display EDS elemental mapping of Co/CoO_x on carbon microlattices.

[0037] FIGS. 9(a)-9(f) display graphical representation of phase and chemical characterization of polymer infusion additive manufacturing. XRD patterns of 9(a) CuO_x/C and

$Cu/CuO_x/C$, and 9(d) CoO_x/C and $Co/CoO_x/C$ microlattices. XPS spectra and fitting curves of 9(b) and 9(c) CuO_x/C and $Cu/CuO_x/C$ microlattices, and 9(e) and 9(f) CoO_x/C and $Co/CoO_x/C$ microlattices.

[0038] FIGS. 10(a)-10(f) display electrocatalytic performance for HER of $Cu/CuO_x/C$ and CuO_x/C catalysts in 1.0 M KOH solution. 10(a) displays linear sweep voltammetry. 10(b) displays Tafel plots. 10(c) displays schematic illustration of bubble evolution on powder and 3D microlattices. 10(d) displays calculated turnover frequencies (TOFs) for H_2 per active site. 10(e) displays Nyquist plots, derived from electrochemical impedance spectroscopy. 10(f) displays long-term stability (Chronoamperometry) measurement.

[0039] FIGS. 11(a)-11(g) display electrocatalytic performance for HER of different microlattices in 1.0 M KOH solution. 11(a) displays a schematics illustration of different types of microlattices. 11(b) displays linear sweep voltammetry. 11(c) displays Tafel plots. 11(d) displays a comparison of overpotential at 10 mA/cm^2 and Tafel slopes between 3D microlattices of $Cu/CuO_x/C$ and other 3D structured electrocatalysts. 11(e) displays a schematic illustration of bubble evolution on different microlattices. 11(f) displays ECSA Plots obtained by the extraction of the double-layer capacitance (C_{dl}) from different 3D electrodes. 11(g) displays Nyquist plots, derived from electrochemical impedance spectroscopy.

[0040] FIGS. 12(a)-12(c) display electrocatalytic performance for OER of $Co/CoO_x/C$ and CoO_x/C cubic microlattices catalysts in 1.0 M KOH solution. 12(a) displays linear sweep voltammetry. 12(b) displays Tafel plots. 12(c) displays a comparison of overpotential at 10 mA/cm^2 and Tafel slopes between 3D microlattices of $Co/CoO_x/C$ and other 3D structured electrocatalysts.

[0041] FIGS. 13(a)-13(d) display bubble release dynamics. 13(a) displays a schematics illustration of different types of printed 3D microlattices and random foams and respective side view images to show the bubble release with the guide of buoyant force (F_B). 13(b) displays high-speed camera images of bubble release from printed 3D microlattices and random foams to evaluate the time for bubble release time. 13(c) displays a schematics illustration of bubble evolution in bare and with microlattices. 13(d) displays the normalized velocity of bubble in different 3D microlattices and random foams.

[0042] FIG. 14(a) displays a TEM image of $Cu/CuO_x/C$ and 14(b) displays a high-resolution transmission electron microscope image of $Cu/CuO_x/C$.

[0043] FIG. 15(a) displays XPS survey spectra of $Cu/CuO_x/C$ and 15(b) displays XPS survey spectra of $Co/CoO_x/C$.

[0044] FIG. 16 displays thermogravimetric analysis of bare, $Cu(NO_3)_2$, and $Co(NO_3)_2$ soaked microlattices.

[0045] FIGS. 17(a)-17(c) display cyclic voltammetry of cubic (17(a)), and BCC (17(b)), and Octet 3D microlattices with different scan rates (17(c)).

[0046] FIG. 18 displays long term stability (Chronopotentiometry) test of cubic $Cu/CuO_x/C$ 3D microlattices for HER.

[0047] FIG. 19 displays Nyquist plots for cubic CoO_x/C, and $Co/CoO_x/C$ microlattices for OER.

[0048] FIG. 20 displays enlarged plot of impedance vs time with the details of bubble growth and detachment on powder and 3D microlattices of $Co/CoO_x/C$ for OER activity.

[0049] FIG. 21 displays a long-term stability (chronoamperometry) test of cubic $Co/CoO_x/C$ 3D microlattices for OER.

[0050] FIG. 22 displays water contact angles of (a) 3D microlattices of $Cu/CuO_x/C$, (b) bare 3D microlattices of polymer, (c) carbonized 3D microlattices.

[0051] FIG. 23(a) displays XRD patterns of bimetallic CuCo/ $CuCoO_x$ 3D microlattices, and FIG. 23(b) displays XRD patterns of bimetallic $CoNi/CoNiO_x$ 3D microlattices.

[0052] FIG. 24 displays STEM images of bimetallic $CuCo/CuCoO_x$, 3D microlattices and respective EDS mapping.

[0053] FIG. 25 displays SEM images of bimetallic $CoNi/CoNiO_x$ 3D microlattices and respective EDS mapping.

[0054] FIGS. 26(a) and 26(b) display electrocatalytic performance for HER of bimetallic transition metal/metal oxides 3D microlattices in 1.0 M KOH solution. 26(a) displays linear sweep voltammetry. 26(b) displays Nyquist plots.

DETAILED DESCRIPTION OF THE DISCLOSURE

[0055] Although claimed subject matter will be described in terms of certain embodiments, other embodiments, including embodiments that do not provide all of the benefits and features set

forth herein, are also within the scope of this disclosure. Various structural, logical, process step, and electronic changes may be made without departing from the scope of the disclosure.

[0056] Ranges of values are disclosed herein. The ranges set out a lower limit value and an upper limit value. Unless otherwise stated, the ranges include all values to the magnitude of the smallest value (either lower limit value or upper limit value) and ranges between the values of the stated range.

[0057] The steps of the method described in the various embodiments and examples disclosed herein are sufficient to carry out the methods of the present invention. Thus, in an embodiment, the method consists essentially of a combination of the steps of the methods disclosed herein. In another embodiment, the method consists of such steps.

[0058] The embodiments disclosed herein include fabricated continuous 3D free-standing transition metal oxides (e.g., copper oxide (CuO), cobalt oxide (Co_3O_4), and nickel oxide (NiO)) and carbon composites for efficient alkaline hydrogen evolution reaction (HER) and oxygen evolution reaction (OER). The resulting 3D free-standing transition metal oxide and carbon composite catalyst delivered an efficient electrocatalytic activity for both HER and OER. For HER, chemically-modified reduced copper oxides and carbon composites showed overpotential of 155 mV at a current density of 10 mA/cm^2 and a Tafel slope of 134 mV/dec, which outperformed the other 3D noble metal free oxide electrocatalyst. Moreover, for OER, chemically modified cobalt oxide showed overpotential of 1.42 V at a current density of 10 mA/cm^2 and a Tafel slope of 55 mV/dec, surpassing the existing cobalt oxide-based 3D electrocatalysts. The overpotential is shown in FIG. 1. It is expected that demonstrated performance can be improved by alloying the metal oxides. This may be relevant for CuO_x or other metal oxides.

[0059] In addition, chemically modified reduced copper oxides and carbon composites catalyst also showed an improved durability of up to 240 hours of continuous hydrogen evolution without any significant change in overpotential and current density, which is ten times better than previous 3D catalysts. These experimental results indicate that 3D free-standing, ordered transition metal oxide and carbon composite with pore sizes of a few hundreds of micrometers expose more active sites and allow efficient discharge of gas bubbles for fast and efficient production of H_2 with high stability.

[0060] The 3D nanoporous catalysts disclosed herein also exceed the performance of existing 3D printed electrolyzer materials for HER that utilized electroplating for coating the electrodes. An advantage of the disclosed embodiments over extruded 3D printed parts based on polymer composites is that the process embodiments disclosed herein allow for greater design freedom and demonstration of catalyst materials with both high porosity and high mechanical durability. Additionally, the disclosed process is freely able to allow for mixing of multiple transition metal precursors to form more complex metal/metal oxide alloys suitable for catalyzing multiple reactions (HER, OER, CO_2 reduction, oxygen reduction reaction (ORR), hydrogen oxidation reaction (HOR) etc.).

[0061] 3D electrodes that include transition metal oxides and carbon are disclosed. The composite can serve as a highly stable and active electrocatalyst for multiple catalytic functions in efficient renewable energy systems. The disclosed 3D-printed lattice-based mesoporous electrodes offer a high-density of electrochemically active sites, facilitate transport of reactants to improve kinetics of efficient electrocatalytic activity, and enhance stability via effective bubble evolution in large-scale electrochemical reactors. Embodiments disclosed herein can be used to prepare and optimize 3D structures and are templates for conformally coating transition metal oxides. Improvements to electrochemical performance can be achieved by performing both the hydrogen evolution reaction and the oxygen evolution reaction using the 3D electrode architecture.

[0062] The precursor materials (e.g., metal salts like metal nitrates) used to coat the 3D conductive carbon lattices are earth-abundant. These precursor materials are lower cost than other metal catalyst materials, like platinum or IrO_2. Other metal oxides are possible, so the electrode design and fabrication disclosed herein can be extended to multiple material systems.

[0063] The oxygen stoichiometry of the coatings can be precisely controlled. This can tune the surface to optimize electrochemical activity. In an embodiment, oxidative or reducing post-annealing steps can be performed (e.g., heating in a tube furnace under O_2 flow or N_2/H_2 flow to adjust the oxygen stoichiometry). Temperature ranges used may be from 300 °C to 800 °C.

[0064] A 3D lattice electrode can be fabricated using stereolithography 3D printing. The stereolithography 3D printing can form a free-standing strut lattice structure with periodic pore structures. Examples of this include octet, body-centered cubic, simple cubic, and Kelvin cell lattices, though other designs are possible.

[0065] Embodiments of the present disclosure include a functional electrocatlyst electrode that may be structural in nature, which render the strut lattice as free-standing. This can use a binder-free approach, such that binder materials or supports are not used in formation. This differs from traditional electrocatalysts that are formed by mounting functional catalyst powders on support structures using binder materials that reduce the effective loading.

[0066] Embodiments of the present disclosure promote effective mass transport of the electrolyte and gas bubbles at a given operating current density. For example, finer lattices with smaller pores have higher total surface area, which can promote greater activity.

[0067] In an embodiment, dimensions of the pores may be from approximately 10 μm to approximately 1 mm or greater. For example, pore sizes from 50 μm to 1 mm may be used. Other pore sizes may be used. Pores larger than 1 mm may result in a lower performance per weight or per volume because the surface area of the electrocatalyst may be lower due to the coarse or large pore structure. However, pores up to 10 mm may be used. In an instance, hierarchical lattices can integrate smaller and larger pores (such as 10 mm). Pores smaller than 10 μm may be used, but may inhibit bubble transport in some applications. Thus, various pore sizes and pore dimensions may be used depending on the application.

[0068] Various 3D printing technologies and photopolymers can be used for the embodiments disclosed herein. Specifically, 3D printing technologies capable of making porous lattice structures can be used. Stereolithography is one 3D printing technology that can be used and that can make a porous lattice structure. The stereolithography process can have high resolution (e.g., down to 50 μm beam sizes). The resulting features can be further shrunk during an annealing process, such as being shrunk down to the 20 μm range. A stereolithography process can be faster than other 3D printing methods, particularly when scaled to high-resolution features. A stereolithography process can be scaled up to the 100's of cm^2 area that may be relevant to industrialized production of electrolyzers.

[0069] An infusion step can soak the polymer lattice in a concentrated solution of metal salts dissolved in water. The polymer may be an acrylate-based photopolymer or other material. The metal salts may be hydrated transition metal nitrates or other species. The infusion step may occur over 24-96 hours at a temperature from 60 °C to 100 °C. The metal salt will have soaked into the polymer structure at the end of the infusion step.

[0070] The concentration of the solution can range from 1 M to 3 M. A concentration that is too low will lead to low catalyst loading and lower performance. Higher concentrations are possible, but may be limited by the metal salt solubility in the solvent.

[0071] A thermal annealing step is then performed at temperatures from 400 °C to 700 °C to convert the metal oxide/polymer lattice to a 3D lattice with graphitic or glassy carbon and a high-surface area metal/metal oxide coating. The thermal annealing step can induce shrinking, which may enhance the resolution of the 3D printed structures. Isotropic shrinkage in the range of 40-70% in the dimension was observed. For example, for starting structures approximately 4 by 4 mm, the structures were approximately 2 x 2 x 2 mm after the annealing process. The thermal annealing step also can enhance surface area and improve electrochemical performance of the electrodes.

[0072] X-ray diffraction (XRD) characterization of the 3D structures demonstrates that different crystalline transition metal oxides (e.g., CoO_x, CuO_x, NiO_x) were synthesized on the carbon templates by pyrolizing the metal salt precursor. XRD spectra suggest that different transition metal oxides form with the variation of temperature during thermal annealing. CuO_x can be reduced to Cu with increasing temperature. CoO_x can be partially reduced with increasing temperature. NiO_x is not reduced at higher temperature and possesses only a NiO_x phase.

[0073] Other transition metal oxides such as TiO_x, ZnO_x, MnO_x, MoO_x, WO_x, FeO_x, VO_x, or other species may also be used. Other transition metal oxides that include iron, titanium, vanadium, manganese, molybdenum, or other materials can be used.

[0074] Morphological characterization by SEM suggests that different microscale and nanoscale surface morphologies are formed with the variation of temperature during the thermal anneal. For CoO_x, there are three different surface structures formed at different temperatures (400 °C, 450 °C, and 700 °C): planar, textured, and vertical sheets. For CuO_x, there are three different surface structures formed at different temperatures (400 °C, 450 °C, and 700 °C): planar, porous, and microrods. For NiO_x, there are different surface structures formed at different temperatures (400 °C, 450 °C, and 700 °C): planar sheets and flower-like surfaces.

[0075] The 3D structures with transition metal oxides can be formed with different oxygen stoichiometries and surface morphologies with the modulation of thermal synthesis time and temperature. The synthesis time was approximately 1-3 hours, but this may be extended to produce additional mass loss and crystallization. The synthesis temperature was from 400 °C to 700 °C, but

higher temperatures may be used with a vacuum annealing step. For example, a temperature up to approximately 900 °C may be used.

[0076] Annealing at 400 °C may be needed for adequate carbonization to make the lattice conductive. 400 °C also may be the approximate value to fully decompose the metal nitrate precursor salt to form the metal oxides.

[0077] 3D transition metal oxides were produced, which may be used as an efficient electrocatalyst for hydrogen evolution reaction (HER) and oxygen evolution reaction (OER). Experimental results show that 3D CoO_x may need a lower overpotential (1.39 V) to produce measurable OER activity (10 mA/cm^2). This low overpotential for OER is comparable to benchmark noble metal based electrocatalysts. The charge transfer resistance of the resulting 3D structures is low (1.25 Ω), which can improve kinetics for OER activity. By using a CuO_x coating on the 3D carbon lattice, the 3D CuO_x exhibited lower overpotential (66 mV) for HER, which is comparable to other earth-abundant catalysts for HER. The disclosed 3D catalyst electrodes also possess improved performance characteristics and stability compared with powders formed with identical stoichiometries.

[0078] The oxygen content of the 3D transition metal oxides may be modulated by annealing in either reducing or oxidizing environments. Post-processing also can be used to enhance the activity of the carbon lattice support material.

[0079] Other transition metal oxides that include iron, titanium, vanadium, manganese, molybdenum, or other materials can be used. These transition metal oxides can be FeO_x, TiO_x, V_2O_x, VO_x, MnO_x, MoO_x, etc. Other metals, such as Zn, In, Ir, W, or other species may also be used. These metal oxides may also have improved performance in electrocatalysis. The surface chemistry may be changed through chemical modification processes, including adjusting the time, temperature, and concentration of precursors.

[0080] Mixture of metal oxides or alloyed metal oxides may be used as catalyst materials. The mixture of the two phases may create lattice strain, leading to a higher density of active sites to enhance electrocatalytic performances. Some examples include $CoFeO_x$, $FeNiO_x$, and $CoNiO_x$, though others are possible.

[0081] Embodiments disclosed herein may enhance mechanical stability of the electrodes by directly integrating the active catalysis material and the support without additional binders and/or

current collector materials. Using a binder can lower the electrocatalytic performance because it displaces active materials and adds an insulating element. Usually, binders are not active for electrocatalytic performances and only increase the mass/thickness of the electrodes. The 3D structures disclosed herein are also more mechanically stable that powder electrocatalysts by facilitating bubble evolution.

[0082] Other transition metal oxides may be synthesized. This may use other metal salts, such as chlorides, acetylacetonates, acetates, fluorides, bromides, or other materials.

[0083] While disclosed with electrodes, the composition and structures disclosed herein may be used with other electrochemical devices, such as supercapacitors or fuel cells.

[0084] Embodiments disclosed herein provide improved stability, intrinsic activity, and active site densities compared to traditional earth-abundant electrocatalysts. This is provided through 3D structuring and chemical modification during heat treatment. The 3D structure may exhibit the smaller overpotential of 1.39 V at 10 mA/cm^{-2} in 1.0 M KOH for OER.

[0085] 3D printing may enable high-speed additive manufacturing of catalysts in a variety of shapes. These shapes may be used with specific electrolyzer equipment. In an embodiment, the 3D printing process involves optimization of support structures located at the vertices of 3D printed lattices to provide support during the printing process. The 3D printed lattice structure may be individualized based on its feature size and its overall porosity so that the micro-lattices formed have favorable mechanical properties.

[0086] In an embodiment, the lattice structure may have pores that are vertically aligned to form channels. The channels may be provided for bubble evolution. The 3D structure may include pores that facilitate bubble release, which avoids blockage of active sites on the catalyst. This may improve performance of the electrode relative to existing designs. For example, cubic lattices form channels that facilitate bubble evolution. Further, octet latices may not have such aligned pores to form a channel, which may cause slower bubble evolution.

[0087] The electrodes may have overall dimensions from 2 mm to 20 mm. The electrodes may be made into rectangular slabs, discs, or other shapes using 3D printing.

[0088] The following examples are presented to illustrate the present disclosure. They are not intended to be limiting in any matter.

EXAMPLE 1

[0089] This example provides a description of embodiments of a nanoporous 3D transition metal oxide and carbon composite electrodes for efficient electrocatalysis.

[0090] Water electrolysis serves an environmentally friendly, sustainable and renewable method to produce hydrogen. Usually, water electrolysis includes two half-reactions: hydrogen evolution reaction (HER) ($4\ H^+ + 4e^- \rightarrow 2\ H_2$) on the cathode and oxygen evolution reaction (OER) ($4OH^- \rightarrow O_2 + 2\ H_2O + 4e^-$) on the anode. An acidic medium is generally preferable for HER because a proton rich environment is favorable for hydrogen adsorption on catalyst surface. However, acidic conditions limit the use of non-platinum group metals as catalysts and causes a stability issue by inducing severe chemical corrosion of electrolyzers. On the contrary, the sluggish kinetics of the OER process cause the limiting step of water electrolysis, specifically in the associated proton-coupled electron transfer step. These factors create barriers and add cost for constructing large-scale electrolyzers. In this respect, using an alkaline medium in which non-platinum group metals such as Ni, Cu, Co, *etc.* can function as an electrocatalyst/electrode for water electrolysis in a relatively mild chemical environment could avoid these issues. However, the higher activation barrier of water dissociation makes HER sluggish in an alkaline medium. Therefore, alkaline HER/OER catalysts that contain both hydrogen adsorption sites as well as water adsorption and dissociation sites are needed.

[0091] Transition metal oxides such as NiO, Co_3O_4, CuO, *etc.* are promising alkaline electrocatalysts for water electrolysis due to their multiple redox states and incompletely filled *d* orbitals, serving as actives sites for water adsorption and dissociation in alkaline electrolytes. However, the lack of hydrogen adsorption sites in transition metal oxides restricts the electrocatalytic activity from achieving performance comparable to noble metal-based electrocatalysts. In this regard, the integration of transition metal oxides with metallic transition metals can provide more hydrogen adsorption sites to achieve enhanced electrocatalytic activity comparable to that of Pt-based electrocatalysts. However, the vulnerability to oxidation of metallic transition metals could create stability issues of the integrated electrocatalysts. In addition, the composite of transition metal oxides and metallic transition metals interfaces might not be able to fully utilize the active surface area of electrocatalysts. To this end, creating 3D electrodes with

integrated transition metal oxides with and metallic transition metals may solve the full utilization of active sites due to high specific surface area and high loading capacity of active materials. Moreover, 3D electrodes with integration of partial oxides of transition metals with active carbon can further enhance the electrocatalytic activity by decreasing the coordination number of transition metals, solving the chemical stability issues of transition metals in alkaline electrolytes as well. However, mechanical stability of these randomly assembled 3D electrodes can hamper the electrocatalytic activity of these electrodes. In this respect, continuous 3D mesostructured electrodes may solve the mechanical and chemical stability issues by facilitating fast discharge of evolved gas bubbles and by providing fresh active sites for robust electrocatalytic activity. In addition, free standing continuous 3D structured electrodes may be desirable to boost efficient electrocatalytic activity due to its amenability to be mass produced and used directly as an electrode without the need for the addition of binders or current collectors.

[0092] Embodiments of the present disclosure include a 3D continuous nanoporous free-standing microstructures of transition metal oxides (copper oxide (CuO), cobalt oxide (Co_3O_4), and nickel oxide (NiO)) and carbon composites for efficient alkaline hydrogen evolution reaction (HER) and oxygen evolution reaction (OER). The resulting 3D free standing transition metal oxide and carbon composite catalysts can deliver efficient electrocatalytic activity after partial oxidation of transition metal oxides. For HER, 3D continuous nanoporous free standing partially reduced CuO and carbon composites showed overpotential of 155 mV at a current density of 10 mA/cm^2 and a Tafel slope of 134 mV/dec, which outperformed other 3D noble metal free oxide electrocatalysts. Moreover, for OER, 3D nanoporous free standing partially reduced Co_3O_4 showed an overpotential of 1.42 V at a current density of 10 mA/cm^2 and a Tafel slope of 55 mV/dec, surpassing the recently reported cobalt oxide 3D electrocatalysts. The higher electrocatalytic activity of 3D continuous nanoporous free-standing microstructures can be attributed to the carbon composite with partial reduced transition metal oxides, which decreases the coordination number of transition metals by distorting the local structures of transition metal oxides, favoring the hydrogen adsorption. In addition, chemically modified reduced copper oxides and carbon composites catalyst also showed superior durability: up to 240 hours of continuous hydrogen evolution without any significant change in overpotential and current density. Carbon protection of the vulnerability to oxidation of partial reduced metallic transition metals enhances the chemical stability and 3D free standing,

ordered structures with porosities of a few hundreds of micrometers exposes more active sites, and allows fast discharge of gas bubbles ensures the mechanical stability of the electrode.

[0093] Continuous 3D-nanoporous composites of partially reduced transition metal oxides and active carbon showed efficient and highly stable electrocatalytic activity for alkaline HER and OER by manipulating the affinity for oxygen and hydrogen species. The use of active carbon also assisted to obtain better ion conductivity and to form the oxide of partially-reduced metallic metals. 3D-nanoporous composites were fabricated by the stereolithography technique followed by an infusion and annealing process with low-cost transition metal salts. To obtain different structures, after infusion of transition metal salts into a photo active polymer, the annealing temperatures was varied from 400 °C to 700 °C. Representative scanning electron microscopy (SEM) images of the continuous 3D-nanoporous composites fabricated at different temperatures are shown in FIGS. 2-4. It was revealed from SEM images that partially reduced cobalt oxide three different (planar, textured, and vertical sheets) surface structures were formed at different annealing temperatures (400 °C, 450 °C, and 700 °C). However, reduced copper oxide formed planar, porous, and microrods surface morphologies at 400 °C, 450 °C, and 700 °C.

[0094] Moreover, nickel oxide formed planar, sheets, and flower like structures at 400 °C, 450 °C, and 700 °C.

[0095] Additionally, SEM image of the 3D-nanoporous composites revealed that the nanoporous structure was synthesized without pore clogging or structural degradation, indicating that 3D-nanoporous composites were fabricated homogeneously on the cm^3 scale. It was also revealed that well-ordered continuous 3D-nanoporous composites had micropores with controllable sizes of approximately 100 μm. Moreover, SEM showed that the 3D-nanoporous composites had nanopores of few hundred nanometers, which may act as active sites for efficient electrocatalytic activity.

[0096] To determine the crystal structures of 3D-nanoporous composites, X-ray diffraction (XRD) analysis was performed (FIGS. 5(a)-5(c)). It was revealed from the XRD patterns that the 3D-nanoporous composites were composed of different oxides such as cobalt oxide, copper oxide, nickel oxide and carbon with peaks one to one corresponding to the standard XRD patterns. It was also revealed from XRD that with the variation of annealing temperature (400 °C to 700 °C), different oxides of transition metals were formed. It was found that with increasing the temperature,

the transition metal oxides behave quite differently. In the case of copper oxide, it was mostly reduced to copper by increasing the temperature. However, cobalt oxide was reduced partially at higher annealing temperatures. Moreover, nickel oxide was not reduced at all with increasing the temperature. The broad peak 20^0 to 30^0 in all composites revealed the presence of amorphous carbon.

[0097] The HER and OER electrocatalytic activities of the 3D-nanoporous composites of transition metal oxides and carbon were evaluated in 1.0 M KOH electrolyte using a 3-electrode system. All potentials were referenced to the reversible hydrogen electrode (RHE). First, the OER activities of the nanopatterns were evaluated by comparing linear sweep voltammetry (LSV) parameters at a scan rate of 10 mV/sec. As shown in FIG. 6(a), the overpotential to obtain a 10 $mAcm^{-2}$ current density of the 3D-nanoporous composites of cobalt oxide electrode was the smallest (1.42 V) when compared with copper oxide (1.49 V), and nickel oxide (1.66 V). Additionally, the overpotential of the 3D-nanoporous composites of cobalt oxide electrode was close to that of a state-of-the-art noble metal oxides electrocatalyst under the same conditions. It was found that the composites, which are formed at 700 °C, showed good electrocatalytic activity for OER. However, composites formed at 400 °C and 450 °C showed poor electrocatalytic activity for OER. To determine the OER kinetics, the LSV curves were fitted to obtain Tafel plots. Tafel plot analysis provided information about the rate-determining steps. FIG. 6(b) shows that the Tafel slope of 3D-nanoporous composites of cobalt oxide electrode was 51 mV/dec, which is better than that of noble metal based electrocatalysts, demonstrating the favorable OER kinetics. Moreover, the 3D-nanoporous composites of cobalt oxide electrode Tafel slope value implied a Tafel mechanism, in which the adsorption of oxygen species is fundamental. To further understand the intrinsic electrocatalytic activity of the 3D-nanoporous composites of transition metal oxides and carbon electrodes, electrochemical impedance spectroscopy measurements at an overpotential of 1.5 V were conducted to investigate the charge transfer resistance (R_{ct}). As shown in FIG. 6(c), the Nyquist plots indicated that the 3D-nanoporous composites of cobalt oxide electrode possessed the smallest charge transfer resistance ($R_{ct} = 2\ \Omega$) among all samples, revealing faster charge transfer and more favorable OER kinetics. However, 3D-nanoporous composites of copper oxide contained higher R_{ct} (5 Ω), suggesting mixed state of transition metal oxides and metallic transition metals provide better kinetics for electrocatalytic activity in alkaline electrolyte.

[0098] Like OER, electrocatalytic activity for HER was tested in 1.0 M KOH electrolyte using a 3-electrode system. FIG. 7(a) shows the LSV curves of the 3D-nanoporous composites of transition metal oxides and carbon in 1.0 M KOH electrolyte, measured at scan rate of 10 mV/sec.

[0099] Contrary to OER, it is shown in FIG. 7(a) that the 3D-nanoporous composites of copper oxide, synthesized at 450 °C had lowest overpotential 150 mV to obtain of 10 $mAcm^{-2}$ current density when compared with cobalt oxide (305 mV), and nickel oxide (350 mV). The lowest overpotential of 3D-nanoporous composites of copper oxide can be attributed to the mixed state of copper oxides and metallic copper due to its multiple redox states (Cu^{0}, Cu^{-1}, Cu^{+2} and Cu^{+3}), which expose many active catalytic sites, ensuring fast exchange of protons for hydrogen adsorption and desorption. However, 3D-nanoporous composites of cobalt oxide were not reduced at 450 °C to produce a mixed state of cobalt oxides and metallic cobalt (FIG. 5(a)). To get the efficient electrocatalytic activity HER in alkaline electrolytes, the mixed states of transition metal oxides and transition metals were used for facile charge transportation and adsorption/desorption of oxygen species. It was found that at higher annealing temperatures, 3D-nanoporous composites of copper oxide were fully reduced to copper, restricting the electrocatalytic activity in an alkaline medium (FIG. 5(b)). However, in the case of 3D-nanoporous composites of cobalt oxide, oxides were dominating, which hindered the electrocatalytic activity for HER in an alkaline medium. To see the annealing temperature effects, the HER electrocatalytic activity of the samples synthesized at a lower temperature (400 °C) were measured (FIG. 7(b)). Samples synthesized at 400 °C have only oxide states of transition metals (FIGS. 5(a)-5(c)), resulting in lower electrocatalytic activity for HER in an alkaline medium. It was also found that 3D-nanoporous composites of nickel oxide were neither good for OER or HER, confirming that a mixed state can be important for electrocatalytic activity in the alkaline medium. Similar to OER, ion conductivity and electron transfer rate can be important factors affecting the electrocatalytic activity for HER. The Nyquist plots to obtain charge transfer resistance (R_{ct}) in HER electrocatalytic activity of samples at 150 mV are shown in FIG. 7(c). The Nyquist plots reveal that 3D-nanoporous composites of copper oxide exhibit minimum charge transfer resistance (10 Ω), consistent with HER performance, further confirming the importance of the mixed oxidation state for achieving favorable HER kinetics.

[0100] Embodiments of the present disclosure include 3D-nanoporous composites of mixed state of transition metal oxides and carbon as electrocatalysts for water electrolysis in alkaline

medium. The morphological feature with the combination of micro and nano pores provides more active sites, boost the reaction kinetics, and enhance the mechanical and chemical stability of electrodes by fast discharge of evolved gas bubbles. During the electrocatalytic process, mixed state of transition metal oxides and metallic transition metals with carbon interactions enhance electrocatalytic activity. Impressively, 3D-nanoporous composites of cobalt oxides exhibit superior OER performance in alkaline with overpotential close to noble metal based electrocatalysts. In addition, 3D-nanoporous composites of copper oxide exhibit favorable HER activity. Embodiments of the present disclosure include 3D-nanoporous composites electrocatalysts used for the conversion and storage of energy.

[0101] In this example, embodiments of continuous 3D free standing transition metal oxides (copper oxide (CuO), cobalt oxide (Co_3O_4), and nickel oxide (NiO)) and carbon composites for efficient the alkaline hydrogen evolution reaction (HER) and oxygen evolution reaction (OER) were fabricated. The resulting 3D free-standing transition metal oxide and carbon composite catalyst delivered an efficient electrocatalytic activity for both HER and OER. For HER, chemically modified partially reduced copper oxides and carbon composites showed overpotential of 155 mV at a current density of 10 mA/cm^2 and a Tafel slope of 134 mV/dec, which outperformed the other 3D noble metal free oxide electrocatalyst. Moreover, for OER, chemically-modified cobalt oxide showed an overpotential of 1.42 V at a current density of 10 mA/cm^2 and a Tafel slope of 55 mV/dec, surpassing the recently reported cobalt oxide based 3D electrocatalysts. In addition, chemically modified reduced copper oxides and carbon composites catalyst also showed superior durability. Embodiment of the present disclosure demonstrated up to 240 hours of continuous hydrogen evolution without any significant change in overpotential and current density, which is 10 times better than recently reported 3D catalysts. Experimental results of this example indicated that 3D free standing, ordered transition metal oxide and carbon composite with porosities of a few hundreds of micrometers expose more active sites, and allows fast discharge of gas bubbles for fast and efficient production of H_2 with high stability.

EXAMPLE 2

[0102] This example provides a description of embodiments of 3D printed microlattices of transition metal/metal oxides for highly stable and efficient water splitting.

[0103] Developing affordable electrocatalysts is crucial for driving the sustainable energy transition to green hydrogen. This example describes a generalizable method known as polymer infusion additive manufacturing (PIAM) for transforming 3D printed photopolymers into core-shell microlattice electrodes for electrocatalytic water splitting with transition metal/metal oxides/carbon heterointerfaces. The optimized free-standing architectures integrate Cu/CuO_x on carbon ($Cu/CuO_x/C$) microlattices, yielding high electrocatalytic activity (overpotential of 145 mV at 10 mA/cm^2 and a Tafel slope of 134 mV/dec) and durability for HER (>100 hr), surpassing state-of-the-art Cu foams. Additionally, for oxygen evolution (OER), Co/CoO_x on carbon ($Co/CoO_x/C$) microlattices display favorable activity with the lowest overpotential (1.40 V to gain 10 mA/cm2) among all reported PGM-free electrodes. This example explores the gas phase mass-transport properties of these 3D microlattices via microscopic imaging of bubble evolution, finding that the outstanding electrocatalytic performance and long-term stability of microlattice electrodes leverages their mesoscale (100-300 μm) pores, providing accessibility of electrolytes, maximizing utilization of active sites, and ensuring rapid evolution of gas bubbles. Thus, embodiments of the present disclosure include a technique for manufacturing 3D mesostructured electrocatalysts with deep control of liquid and gas phase mass-transport, enhancing the efficacy of alkaline water electrolysis.

[0104] This example targeted the application of high-resolution additive manufacturing of a periodic 3D micro/mesostructured electrode to enhance bubble release and expedite the mass transfer of surrounding electrolyte to boost the rate and stability of electrochemical reactions for efficient large-scale water splitting. Additive manufacturing (AM), including 3D printing, has emerged as a promising method for producing customized structures with precise digital control. So far, 3D microstructured electrocatalysts have been prepared using direct ink writing (DIW), indirect fused deposition modeling (FDM), or selective laser melting (SLM). Extrusion-based methods like FDM and DIW offer benefits including affordability, speed, and simplicity, yet they also come with limitations such as restricted design flexibility, lower spatial resolution, weaker mechanical properties, and subpar surface smoothness. Selective Laser Melting (SLM) constitutes an integral element within the power bed fusion (PBF) methodology, widely employed in metal 3D printing due to its capacity for precise output. However, the present state of manufacturing within this process

involves high costs because of the low speed and high cost of feedstocks. In this respect, photopolymerization based 3D printing of polymers offers an alternative for producing large area high-resolution 3D microstructures at a lower cost. Methods such as stereolithography (SLA), involve selectively solidifying a monomeric resin formulation layer by layer, producing complex features down to the single micron scale for a variety of materials like ceramics and hydrogels. Additionally, the SLA method is adept at producing *microlattice*s that can simultaneously provide high surface area and high electrical conductivity along with mechanical strength. These properties make SLA a promising approach for engineering the mass-transport of porous solids, but new chemistries and synthetic approaches are required for extending this benefit to transition metal/metal oxide catalyst materials.

[0105] This example provides a description of the fabrication and architectural design of 3D free-standing microlattices integrating highly active transition metal/metal oxides via SLA (stereolithography) (shown in FIGS. 8(a) and 8(b)) for efficient electrocatalytic water splitting under alkaline conditions. This method utilizes polymer-based 3D scaffold templates designed explicitly for high gas evolution efficiency to improve electrode stability and enhance water splitting performance. These scaffolds were converted into continuous 3D microlattices of transition metal/metal oxides on carbon by a polymer infusion additive manufacturing (PIAM) method to enhance the efficiency of both the alkaline hydrogen evolution reaction (HER) and oxygen evolution reaction (OER). In the case of HER, the 3D microlattices composed of copper oxide (CuO_x) and copper (Cu) on carbon ($Cu/CuO_x/C$) exhibited high performance (overpotential of 145 mV at 10 mA/cm^2 and a Tafel slope of 134 mV/dec) exceeding that of previously reported Cu-based oxide electrocatalysts. Additionally, for OER, the 3D microlattices including cobalt oxide (CoO_x) and cobalt (Co) on carbon ($Co/CoO_x/C$) displayed an overpotential of just 1.40 V at 10 mA/cm^2, with a Tafel slope of 55 mV/dec. These results demonstrated better performance compared to recently-reported cobalt oxide-based 3D microstructured electrocatalysts. Through detailed characterization, a mass-transport mechanism was developed to explain the enhanced electrocatalytic performance of these 3D microlattices, the pore structure of which promotes electrolyte diffusion to the electrocatalyst surface and facilitates bubble evolution, enhancing the electrochemical reaction rate. A concomitant result of improved 3D mass-transport is that microlattices exhibit superior durability, enduring up to 240 hours of continuous hydrogen and oxygen evolution without significant change

in overpotential and current density. This durability is attributed to their ordered microstructures with 100 – 300 μm pores that expose more active sites and allow for fast discharge of bubbles, ensuring mechanical and chemical stability of the electrodes. The efficient and rapid discharge of bubbles from the 3D printed microlattices is influenced by both buoyancy and surface tension, resulting in more effective bubble release compared to flat surfaces due to the ordered pores that provide mesoscale aligned channels favorable for bubble propagation and electrolyte diffusion.

[0106] The polymer infusion additive manufacturing (PIAM) technique disclosed herein, derived from stereolithography, facilitates the preparation of diverse 3D microstructured transition metal derivatives from common acrylate photopolymers and metal salts. 3D architected polymer scaffolds were used as platforms for the subsequent *in situ* synthesis of transition metal and transition metal oxide interfaces on conductive graphitic carbon lattices, as depicted schematically in FIG. 8(c). Stereolithography is employed to create various 3D scaffold templates with adjustable lattice structure, pore size, and volumetric porosity. After the printing phase, the 3D scaffold templates were immersed in an aqueous solution of a metal nitrate salt precursor, facilitating its infusion into the polymer, like in a hydrogel additive manufacturing (HIAM) approach. Calcination in a vacuum converts the metal-salt-infused polymer to coatings consisting of metal oxides on carbon. Subsequent reduction in forming gas (95% N_2, 5% H_2) yields transition metal and transition metal oxide interfaces on the carbon 3D microlattices. To show the versatility of this (PIAM) technique, two different kinds of catalytic 3D microlattices of Cu/CuO_x on carbon ($Cu/CuO_x/C$), and Co/CoO_x on carbon ($Co/CoO_x/C$) were fabricated. Compared to known approaches that rely on particle-laden slurries or resin precursors, PIAM allows the exploration of a considerably broader range of catalyst compositions while ensuring the protection of the conductive carbon core. From optical microscopy images (displayed within circles in the inset of FIG. 8(c)), it was confirmed that during calcination, the polymer scaffold structures shrunk by approximately 50% but maintained the high-resolution 3D microlattice features while incorporating transition metals and transition metal oxides on carbon, ensuring the ability to design a variety of optimal architectures for enhancing mass-transport.

[0107] The morphologies of the 3D microlattices of transition metals and transition metal oxides interfaces on carbon were investigated by scanning electron microscopy (SEM). SEM imaging revealed that 3D microlattices of $Cu/CuO_x/C$, and $Co/CoO_x/C$ retained their precise lattice

shape during thermal treatment (FIGS. 8(d) and 8(g)), with beam diameters of approximately 250 μm. Cross-sectional SEM images illustrate the defect-free core-shell structures of $Cu/CuO_x/C$ (FIG. 8(e)) and $Co/CoO_x/C$ (FIG. 8(h)), a feature of this method that strategically integrates electrochemically active material onto surfaces exposed to the electrolyte. The magnified SEM of $Cu/CuO_x/C$ also shows a continuous lamellar structure originating from the layer-by-layer SLA process (FIG. 8(f)), whereas the $Co/CoO_x/C$ exhibits a similarly dense structure with micron-sized particles on the surface (FIG. 8(i)). Energy dispersive X-ray spectroscopy (EDS) mapping shows conformal distribution of Cu/CuO_x shell on carbon (FIGS. 8(j), 8(k) and 8(l)), and homogenous distribution of Co/CoO_x on carbon (FIGS. 8(m), 8(n), and FIG. 8(o)), confirming a well-defined core-shell structure of each individual beam in the 3D microlattices. Furthermore, transmission electron microscopy (TEM) characterization of the $Cu/CuO_x/C$ microlattices confirmed the homogeneous dispersion of Cu/CuO_x on carbon, with a mean size of 30-40 nm, as shown in FIGS. 14(a) and 14(b).

[0108] To understand the phase and chemical evolution of the microlattices throughout calcination and reduction processes, the phase composition was analyzed using X-ray diffraction (XRD) and the chemical composition was investigated through X-ray photoelectron spectroscopy (XPS) and thermogravimetric analysis (TGA). FIGS. 9(a) and 9(d) show the XRD measurements of calcined 3D CuO_x on carbon microlattices derived from PIAM of $Cu(NO_3)_2$ and 3D CoO_x on carbon microlattices derived from $Co(NO_3)_2$, respectively. Notably, the CuO_x/C and CoO_x/C XRD patterns show the presence of only the oxide phases of Cu and Co after calcination. Partial reduction of these metal oxides in forming gas (500 °C) converts copper oxides to Cu / CuO_x heterointerfaces ($Cu/CuO_x/C$) and cobalt oxide to Co/CoO_x heterointerfaces ($Co/CoO_x/C$), respectively. From these findings, it was evident that the mixed phase of transition metals and their oxides was formed without impurities and that the duration of post-annealing in forming gas could control the relative percentage of the metal/metal oxide to engineer its electrochemical properties.

[0109] XPS analysis of 3D microlattices of CuO_x/C, and $Cu/CuO_x/C$ showed the presence of Cu, C, and O, as illustrated in FIG. 15(a). FIGS. 9(b) and 9(c) shows the Cu 2p XPS spectra and fitting curves of CuO_x/C, and $Cu/CuO_x/C$. The binding energy of 932.1 eV was distinctive of the Cu_2O phase within copper oxide, whereas the prevailing binding energy at 940.5 eV signified CuO in the XPS spectra of CuO_x/C. After reduction, it was observed that the CuO peak disappeared in

$Cu/CuO_x/C$, and the 932.1 eV peak shifted to 932.1 eV, confirming the presence of copper in the 3D microlattices of $Cu/CuO_x/C$. Additionally, the XPS spectra of $Cu/CuO_x/C$ revealed a narrower and higher binding energy shift of the O 1s peak compared to CuO_x/C, confirming the reduction of oxygen in the copper oxide phase. The XPS survey scans of 3D microlattices of CoO_x/C, and $Co/CoO_x/C$ showed the presence of Co, C, and O, shown in FIG. 15(b). FIGS. 9(e) and 9(f) shows the Co 2p XPS spectra and fitting curves of CoO_x/C, and $Co/CoO_x/C$. The shift of the peak at 784.7 eV to 782.3 eV for Co $2p_{3/2}$, typically indicative of Co^{2+}, towards a lower binding energy, confirmed the reduction of CoO to elemental Co. The shift of the peak at 779.7 eV, which is less significant (0.5 eV), indicated the presence of Co^{3+} rather than Co^{2+}, confirming a lower degree of reduction of Co_3O_4 to elemental Co. Furthermore, the XPS analysis of $Co/CoO_x/C$ exhibited a shift in binding energy to a higher value for the O 1s peak in comparison to CoO_x/C, serving as additional confirmation of the oxygen reduction occurring within the cobalt oxide structures. During the TGA analysis of the $Cu(NO_3)_2$ precursor within the 3D microlattices, it was observed that the material retained 25.4 % of its initial mass, signifying complete conversion at 450 °C, shown in FIG. 16. In contrast, the uncoated 3D microlattices made of polymer retained 3.8 % of their original mass, reaching full conversion at 450°C. This revealed a weight ratio of 75 % Cu/CuO_x to 25 % C. However, the TGA analysis of the $Co(NO_3)_2$ precursor within the 3D microlattices revealed that the material retained 12.5 % of its initial mass, confirming a weight ratio of 87.5 % Co/CoO_x to 12.5% C.

[0110] Controlling the oxygen stoichiometry of the microlattice coating through post-annealing enabled the optimization of the mixed Cu/CuO_x phase for HER. The electrocatalytic activity of 3D-microlattices of $Cu/CuO_x/C$ was characterized in a 1.0 M KOH electrolyte. Firstly, HER activity of CuO_x/C, and $Cu/CuO_x/C$ 3D microlattices was compared with a powdered control sample of identical composition by linear sweep voltammetry (LSV) curves, shown in FIG. 10(a). Fully oxidized CuO_x/C 3D microlattices exhibited electrochemical activity for HER, but required a higher overpotential of 210 mV to produce a current density of 10 mA/cm^2 and 502 mV for a current density of 50 mA/cm^2. The reduction of CuO_x/C to form $Cu/CuO_x/C$ microlattices enhanced the HER activity, achieving a low overpotential of 145 mV at 10 mA/cm^2, which is lower than that of other 3D Cu based electrocatalysts. Moreover, when compared to powdered controls, the 3D microlattices demonstrate 3X greater electrocatalytic activity normalized by surface area. The

calculation of the surface area of microlattices follows a methodology outlined in the methods section of this example. This validated that the 3D microlattices both expose a higher abundance of active sites and decreased interface resistance between the electrolyte and the electrode, thereby boosting electrocatalytic efficiency. The Tafel plots were derived from the polarization curves to delve into the reaction kinetics occurring on each electrode, shown in FIG. 10(b). The Tafel slope of $Cu/CuO_x/C$ microlattices was 134 mV/dec^{-1}, which was approximately 4X lower than that of $Cu/CuO_x/C$ powder (392 mV/dec^{-1}), confirming that active materials coupled with appropriate 3D microstructuring facilitated the binding between the catalyst and the adsorbates, enhancing HER kinetics. The improved dynamics observed in 3D microlattices could stem from the effective release of generated gas bubbles, which creates new surface-active sites for adsorbates, as illustrated in FIG. 10(c).

[0111] To further understand how 3D porous microlattices impact the reaction kinetics, the overall turnover frequencies (TOFs) per surface site were quantified, as shown below, and results as shown in FIG. 10(d).

Calculating turn over frequency (TOF) for H_2 of pristine and nitrosulferize samples:

The structural data of Cu/CuO_x as follows:

Density of Cu/CuO_x = 6.31 g cm^{-3}. Average size of nanoparticle (determined from the Scherrer equation) = 30 nm. The shapes of the nanoparticles are approximated to spherical.

Loading amount of MXene on the electrode is 1 mg/cm^2.

Total volume of Cu/CuO_x particles present on the electrode

$= (1 \times 10^{-5}) / 6.31 = 1.6 \times 10^{-6}$ cm^3

Total number of Cu/CuO_x nanoparticles present on the electrode

$= (1.6 \times 10^{-6}) / [(4/3) (\pi) (r^3)]$

$= (1.6 \times 10^{-6}) / [4.18 \times (15 \times 10^{-7})^3]$

$= 1.1 \times 10^{11}$ particles

Surface area of one Cu/CuO_x nanoparticle

$= (4) (\pi) (r^2)$

$= (4) (\pi) (15)^2$ nm^2

$= 1.9 \times 10^{-15}$ m^2

Total surface area of all Cu/CuO_x the nanoparticles present

$= (1.1 \times 10^{11}) \times (1.90 \times 10^{-15}) = 2.1 \times 10^{-4}\ m^2$

The area of per unit cells of $Cu/CuO_x = 1.1 \times 10^{-19}\ m^2$

There are 4 Cu atoms in this unit cell.

Hence, the total number of surface Cu atoms present

$= [4 / (1.1 \times 10^{-19}\ m^2)] \times (2.1 \times 10^{-4}\ m^2)$

$= 7.6 \times 10^{15}$ atoms

We assume that all the surface Cu atoms participate in the HER. Hence, the turnover frequency of H_2 production at Overpotentials = 150 mV (current density measured = 10 mA cm^{-2}, electrolyte = 1 M KOH).

$= [(10\ mA/cm^2)\ (10^{-3})\ (0.196\ cm^2)\ (6.02 \times 10^{23})] / [(96485.3\ C/mol)\ (2)\ (7.6 \times 10^{15})]$

$= 0.83\ s^{-1}$

[0112] As shown in FIG. 10(d), the TOF value of the 3D microlattices with $Cu/CuO_x/C$ is 0.82 s^{-1} at an overpotential of 150 mV – 4X higher than that of powdered $Cu/CuO_x/C$ (0.21 s^{-1}) and higher than that of reported 3D structured Cu/CuO_x. The increased TOF aligned with the enhanced catalytic performance for HER, indicating that the improved activity of 3D microlattices may be a result of their 3D printed porous micro-architecture. Furthermore, electrochemical impedance spectroscopy (EIS) was used to calculate charge-transfer resistance (R_{ct}), shown in FIG. 10(e). The R_{ct} of the 3D microlattices composed of $Cu/CuO_x/C$ was 5X lower (7.0 Ω) than that of the powder control (36.2 Ω), which matched with the other kinetics and suggested that the formation of gas bubbles obstructs a significant portion of the catalytically active surface area within the powdered sample, leading to heightened ohmic resistance. To evaluate the electrochemical durability of the 3D $Cu/CuO_x/C$ microlattices, uninterrupted electrolysis (chronoamperometry) was conducted in 1 M KOH at a fixed potential of 210 mV versus RHE, maintaining an initial current density of 20 mA/cm^2. As depicted in FIG. 10(f), the 3D microlattice exhibited minimal reduction in activity over 120 hours of continual operation, an indication of its stability. By comparison, however, the stability of the $Cu/CuO_x/C$ powder was inferior, showing large fluctuations even under low current density. These fluctuations could arise as bubbles form on the powder surface, impeding active sites and elevating resistance between these sites and the electrolyte.

[0113] To characterize the influence of the specific 3D microarchitecture on electrocatalytic activity, various microlattices were printed, including cubic, body-centered cubic, and octet

structures, as depicted in FIG. 11(a). The highest electrocatalytic activity was observed in cubic $Cu/CuO_x/C$ microlattices, as revealed by LSV (FIG. 11(b)). The superiority of cubic architectures can be attributed to the directional structure of the microlattices, which facilitate the diffusion of electrolytes into the 3D electrodes and efficient bubble release without any obstacles. This, in turn, reduces the resistance between the electrolyte and the electrode while maximizing the utilization of active sites for electrocatalytic activity. Tafel plots from the polarization curves (FIG. 11(c)) show that cubic microlattices exhibit optimal reaction kinetics. In addition, when comparing the performance of the cubic 3D microlattices composed of $Cu/CuO_x/C$ disclosed herein with reported Cu catalysts, particularly Cu/CoO_x foams, the 3D microlattices disclosed herein demonstrated a 2X increase in electrocatalytic activity and exhibited higher kinetics, as shown in the literature comparison of the electrodes' electrochemical activity in terms of overpotential and Tafel slope (FIG. 11(d)). This demonstrates that periodic 3D electrode architectures can enhance performance beyond the limits of random porous foams.

[0114] To clarify the impact of the variable lattice structure, the electrochemically active surface area (ECSA) was extracted for the microlattices by conducting cyclic voltammetry (CV) measurements to determine the electrical double-layer capacitance (EDLC) (C_{dl}) (shown in FIGS. 17(a), 17(b), and 17(c)), which is directly proportional to ECSA. At each scan rate, the cubic 3D microlattices of $Cu/CuO_x/C$ exhibited favorable anodic and cathodic current densities and a quasi-rectangular shape, suggesting a larger active surface area and more electrochemically active sites compared to other electrodes. The plots of differences of charging current density against scan rates (FIG. 11(e)) revealed C_{dl} of 23.2, 18.6, and 2.3 mF/cm^2 for cubic, BCC, and octet $Cu/CuO_x/C$, respectively. The octet electrode exhibited a minimal C_{dl} due to its dense morphology, wherein the dense structures trapped gas bubbles, elevating resistance and limiting available active sites. These factors likely contributed to its comparatively lower HER activity. The charge-transfer resistance (R_{ct}) of the cubic lattice (7.0 Ω) was smallest compared with the BCC (9.8 Ω), and octet (25.9 Ω) (shown in FIG. 11(f)), matching the kinetics results. The optimal R_{ct} of the cubic lattice further demonstrated its efficient electron transfer ability, contributing to its favorable HER activity. Indeed, chronopotentiometry (at 200 mV) measurements of the cubic microlattices showed impressive chemical stability with little overpotential variation over 120 hrs (FIG. 18). This result is among the highest stability reported for 3D Cu based electrodes, affirming the reliability of electocatalysts

fabricated by our PIAM method. Further, FIG. 11(g) displays Nyquist plots, derived from the electrochemical impedance spectroscopy.

[0115] To generalize the polymer infusion additive manufacturing (PIAM) for electrolyzer integration as disclosed herein, cubic CoO_x/C and Co/CoO_x/C microlattices were prepared for performing OER in alkaline media (1M KOH). Additionally, the OER activity of Co/CoO_x/C microlattices were compared at variable reduction temperatures. The reduced Co/CoO_x/C microlattices annealed at 700 °C exhibited the best performance, which can achieve a low overpotential of 1.40 V *vs* RHE at 10 mA/cm^2 (shown in FIG. 12(a)). For additional context, it is highlighted that this result is even lower than that observed for the benchmark RuO_2 (1.42 V *vs* RHE at 10 mA/cm^2) and lower than the overpotential of leading PGM-free electrocatalysts. This finding that both HER and OER electrocatalyst performance can be enhanced via 3D microlattice integration reveals the advantage of these architectures in producing a greater number of active sites and reducing the resistance at the interface between the electrolyte and electrode. This superiority can be attributed to the synergistic effect of a directional 3D structure and reduction of cobalt oxide to cobalt and cobalt oxide interfaces, which facilitates the diffusion of electrolytes and improves the kinetics for OER activity.

[0116] To understand the enhanced kinetics, the Tafel plots were extracted from the polarization curves, as illustrated in FIG. 12(b). The overpotential and Tafel slope of our Co/CoO_x/C microlattice catalysts is 1.40 V *vs* RHE at 10 mA/cm^2 and 51 mV/dec^{-1} for OER activity, which is the best among the reported 3D structured and noble metal free electrocatalysts, shown in FIG. 12(c). Furthermore, EIS was measured to extract the charge transfer resistance (R_{ct}) (shown in FIG. 19). The extremely low R_{ct} of the Co/CoO_x/C microlattice was just 2 Ω, the smallest among reported OER electrocatalysts, which aligned well with the other kinetic results. Stability testing plotting the charge transfer resistance against time for both the Co/CoO_x/C and Co/CoO_x/C powder samples is shown in FIG. 20. The comparison reveals that for the 700 °C reduced Co/CoO_x/C microlattices, the R_{ct} remained unchanged. However, in the case of the Co/CoO_x/C powder, the R_{ct} gradually increased over time. This observation suggests that the efficient evolution of bubbles on the Co/CoO_x/C microlattices can also enhance the stability of the electrode. Chronoamperometry measurements of the 700 °C reduced Co/CoO_x/C microlattices operated at 1.50 V vs RHE (FIG. 21)

show robust stability by maintaining greater than 96% of its initial current density after 90 hrs continuous operation.

[0117] To gain insight into the effects of the 3D microlattice pore structure on gas phase mass transport, experiments examining gas bubble evolution in both random (FIGS. 13(a)(iv) and 13(a)(v)) and ordered microlattices were conducted (FIGS. 13(a)(i), 13(a)(ii), and FIG. 13(a)(iii)) using gas injection and high-speed imaging. Bubble propagation was tracked for both microlattices and commercially available random foams, recording images from a side view using a high-speed camera. In this configuration, N_2 gas was supplied at a flow rate of 1 mL/s through a syringe needle into slabs of 3D structured electrodes approximately 4 mm thick, comparable to the catalyst microlattice dimensions. The initial injection of gas produced singleton bubbles that then propagated through the lattice due to the upward buoyant force (F_B). Video analysis of the bubble propagation time (Δt) for cubic microlattices showed the shortest time (Δt = 100 ms) among the set of 3D printed microlattices. This bubble evolution in cubic and BCC lattices was also faster than evolution through random foams (Δt ~ 200 – 400 ms) (shown in FIG. 13(b)), and even lower than that reported for other 3D printed structures. The slower evolution of gas bubbles within random foams can be attributed to the disordered pore structure, which leads to indirect pathways and trapping in narrow cavities (shown in FIG. 13(a)). In contrast, in cubic microlattices, the bubbles move vertically in alignment with the buoyant force without undergoing scattering. FIG. 13(c) shows a definition of the bubble evolution velocity in pure electrolyte (v_0) and the velocity of evolution in porous solids such as microlattices (v_1). To quantify the ordered pore arrangement effects on the bubble release through the 3D electrode, the normalized bubble velocity (v_1/v_0) was calculated on different 3D ordered microlattices and random structures, as shown in FIG. 13(d). The normalized bubble velocity in 3D printed cubic microlattices was highest (~0.8) among 3D printed microlattices and random structures, further confirming that 3D printed cubic microlattices are efficient for bubble release for achieving favorable electrocatalytic activity. In addition, to understand the fast release of bubbles at a high reaction rate, the hydrophilicity of the $Cu/CuO_x/C$ microlattices was characterized, comparing against the carbonized and polymer microlattices. The contact angle between the gas-liquid interface and the lattice surface was determined to be 48.7°, 99.4° and 81.6° for $Cu/CuO_x/C$ microlattices, carbonized lattices, and polymer lattices, respectively (shown in FIG. 22). The surface wettability of 3D microlattices composed of $Cu/CuO_x/C$ promotes the creation of

evenly sized hydrogen bubbles, a factor in rapid bubble release and reduced charge transfer resistance.

[0118] To determine the crystal structures of 3D-nanoporous composites, X-ray diffraction (XRD) analysis was performed. It was revealed from the XRD patterns that the 3D-nanoporous composites are composed of bimetallic oxides such as copper/cobalt oxide, cobalt/nickel oxide, and carbon with peaks one to one corresponding to the standard XRD patterns, as shown in FIGS. 23(a) and 23(b).

[0119] Furthermore, scanning transmission electron microscopy (STEM), and scanning electron microscopy (SEM) characterizations of bimetallic transition metal/metal oxides (CuCo/$CuCoO_x$, and CoNi/$CoNiO_x$) microlattices confirm the homogeneous dispersion of both metals on carbon.

[0120] As shown in FIG. 24, SEM imaging revealed that 3D microlattices of bimetallic transition metal/metal oxides (CoNi/CoNiOx) retained their precise lattice shape during thermal treatment. Energy dispersive X-ray spectroscopy (EDS) mapping shows conformal distribution of CoNi/CoNiOx on carbon, as shown in FIG. 25.

[0121] Further, this example measured HER activity of bimetallic transition metal/metal oxides 3D microlattices with single transition metal/metal oxides 3D microlattices control sample of identical composition by linear sweep voltammetry (LSV) curves, shown in FIG. 26(a). Single transition metal/metal oxides 3D microlattices exhibit electrochemical activity for HER, but need a higher overpotential of 350 mV to produce a current density of 10 mA/cm^2. The bimetallic transition metal/metal oxides 3D microlattices notably enhances the HER activity, achieving a low overpotential of 230 mV at 10 mA/cm^2. The charge-transfer resistance R_{ct} of the 3D microlattices with bimetallic transition metal/metal oxides 3D microlattices is 2X lower (13.0 Ω) than that of the single transition metal/metal oxides 3D microlattices (25.0 Ω). FIG. 26(b) displays the Nyquist plots.

[0122] Embodiments of the present disclosure include a rapid and robust polymer-infused additive manufacturing 3D printing method for fabricating transition metal-based electrocatalysts for alkaline electrolysis. This example shows how the design of optimal 3D architectures and post-treatments yield microlattice electrodes with increased active sites and improved electrolytic properties of transition metal-based materials. Overall, for alkaline HER Cu/CuO_x/C has efficient

electrocatalytic activity with low overpotential (145 mV to gain 10 mA/cm^2), and for OER $Co/CoO_x/C$ electrode demonstrates exceptional activity with the lowest overpotential (1.40 V to gain 10 mA/cm^2) among all reported PGM-free electrodes. Additionally, this example demonstrated that the deeper connection between 3D electrode architecture and electrochemical stability via 120 hour continuous electrolysis, showing minimal morphological or compositional alterations. The enduring stability of these structures is credited to the rapid elimination of gas bubbles within precise, directional 3D microlattices. This underscores the method's reliability, presenting a viable alternative for fabricating free standing, integrated catalyst/electrode structures in a single scalable process with a high degree of design freedom. The suggested approach allows for the creation of electrocatalytic structures that explicitly optimize mass-transport beyond the limits of random porous architectures.

[0123] **Experimental Methods**

[0124] *Fabrication of 3D microlattices of transition metal/transition metal oxide/carbon*

[0125] First, the Kudo3D stereolithography system was utilized to print 3D polymer microlattices employing Kudo's Ultra High Resolution (UHR) positive resin based on an acrylate photopolymer. This system can be used to produce lattices with features as small as 20 micron after post-annealing processes. 3D microlattices of transition metal/transition metal oxide/carbon are fabricated by simply polymer infusion additive manufacturing. Briefly, first 3D polymer microlattices were infiltrated by respective metal salts. To prepare $Cu/CuO_x/C$, 3D polymer microlattices were infiltrated by an aqueous solution of 1 M $Cu(NO_3)_2$, while for $Co/CoO_x/C$, polymer microlattices were infiltrated by an aqueous solution of 1 M $Co(NO_3)_2$ at 90 °C for 72 hours. The infused 3D polymer structures were then calcined at 450 °C in vacuum and reduced at 500 °C in forming gas in a tube furnace. It was observed that the calcined 3D infused polymer structures formed respective oxide phases of transition metals on carbon (CuO_x/C and CoO_x/C). However, reduction lead to the formation of the transition metal/transition metal oxide on carbon ($Cu/CuO_x/C$ and $Co/CoO_x/C$).

[0126] *Chemical Composition and Microstructural Characterization*

[0127] The X-ray photoelectron spectroscopy (XPS) (Kratos, Axis Supra), powder X-ray diffraction (XRD) (Rigaku, Miniflex), transmission electron microscopy (TEM) (JEOL, 300 KV), scanning electron microscopy (SEM) (Helios 660), and thermogravimetric analysis

(TGA) were employed to explore the chemical composition, perform microstructure analysis, and assess the mass ratio analysis of 3D microlattices consisting of transition metal/transition metal oxide/carbon. TGA tests were performed in a pure N_2 atmosphere.

[0128] *Bubble Evolution Measurements*

[0129] Bubble evolution experiments were performed with a high-speed video camera focused on a slab of microlattice or foam that was 3D printed by similar methods to those used for the catalysts. Frame by frame analysis was used to assess the average bubble velocity in each respective lattice or foam system oriented perpendicular to the direction of buoyant force, an identical orientation to how each catalyst microlattice was tested electrochemically.

[0130] *Electrochemical Characterization*

[0131] Electrochemical characterization was performed with a VersaSTAT electrochemical workstation from Princeton Applied Research equipped with a three-electrode system for studying the activity of the research for the Hydrogen Evolution Reaction (HER) and Oxygen Evolution Reaction (OER). The setup included a working electrode consisting of the 3D microlattices, a reference electrode of Ag/AgCl in 3M KCl, and a counter electrode using Pt wire, all immersed in a 1.0 M KOH electrolyte solution. The 3D microlattices functioned as the working electrode without requiring any additional additives or binders. All potentials were adjusted relative to a Reversible Hydrogen Electrode (RHE) using the following formula.

$$E_{(RHE)} = E_{Ag/AgCl} + 0.059\ pH + E^{\circ}_{Ag/AgCl}, \text{ where } E^{\circ}_{Ag/AgCl} = 0.1976\ V$$

Moreover, the current was normalized based on the surface area of the calcined microlattices. Calculations of the microlattice surface area of the octet, BCC, and cubic lattices based on a graph theory model summing the surface of each individual strut element and accounting for beam intersections were utilized.

[0132] Although the present disclosure has been described with respect to one or more particular embodiments, it will be understood that other embodiments of the present disclosure may be made without departing from the scope of the present disclosure. Hence, the present disclosure is deemed limited only by the appended claims and the reasonable interpretation thereof.

CLAIMS:

1. An electrocatalyst electrode comprising:
a strut lattice structure fabricated of a polymer; and
a composite disposed on the strut lattice structure that includes at least one transition metal oxide, wherein the composite and the strut lattice structure are 3D and free-standing.

2. The electrocatalyst electrode of claim 1, wherein the at least one transition metal oxide comprises copper oxide, cobalt oxide, nickel oxide, titanium oxide, zinc oxide, manganese oxide, molybdenum oxide, tungsten oxide, iron oxide, or vanadium oxide.

3. The electrocatalyst electrode of claim 2, wherein the composite comprises a mixture of one or more of the at least one transition metal oxide.

4. The electrocatalyst electrode of claim 1, wherein the composite defines one or more pores having pore sizes from 10 μm to 1 mm.

5. The electrocatalyst electrode of claim 4, wherein the one or more pores are vertically aligned to form channels.

6. The electrocatalyst electrode of claim 4, wherein the one or more pores are configured to facilitate bubble release.

7. The electrocatalyst electrode of claim 1, wherein the strut lattice structure has an octet, body-centered cubic, simple cubic, or Kelvin cell lattice.

8. The electrocatalyst electrode of claim 1, wherein the composite is a coating on the strut lattice structure.

9. The method of claim 8, wherein the composite is used for alkaline hydrogen evolution reaction (HER) and oxygen evolution reaction (OER).

10. The method of claim 9, wherein the HER demonstrates an overpotential of 155 mV at a current density of 10 mA/cm^2 and a Tafel slope of 134 mV/dec.

11. The method of claim 9, wherein the OER demonstrates an overpotential of 1.42 V at a current density of 10 mA/cm^2 and a Tafel slope of 55 mV/dec.

12. A method comprising:
stereolithography 3D printing a free-standing strut lattice structure with a periodic pore structure, wherein the strut lattice structure is fabricated of a polymer;
infusing the strut lattice structure with a metal salt by soaking the strut lattice structure in a concentrated solution of the metal salt dissolved in water; and
annealing the strut lattice structure at a temperature from 400 °C to 700 °C.

13. The method of claim 12, wherein the strut lattice structure has an octet, body-centered cubic, simple cubic, or Kelvin cell lattice.

14. The method of claim 12, wherein one or more pores in the periodic pore structure have dimensions from 10 μm to 1 mm.

15. The method of claim 12, wherein a duration of the infusing is from 24 to 96 hours.

16. The method of claim 12, wherein the infusing occurs at a temperature from 60 °C to 100 °C.

17. The method of claim 12, wherein the annealing is configured to convert the strut lattice structure to a 3D lattice with graphitic or glassy carbon and a metal/metal oxide coating.

18. The method of claim 12, wherein oxygen stoichiometries and surface morphologies of the strut lattice structure are modified by changing the temperature and a time of the annealing.

19. The method of claim 17, wherein the metal/metal oxide coating comprises at least one transition metal oxide, wherein the at least one transition metal oxide comprises copper oxide, cobalt oxide, nickel oxide, titanium oxide, zinc oxide, manganese oxide, molybdenum oxide, tungsten oxide, iron oxide, or vanadium oxide.

20. The method of claim 19, wherein the metal/metal oxide coating comprises a mixture of one or more of the at least one transition metal oxide.

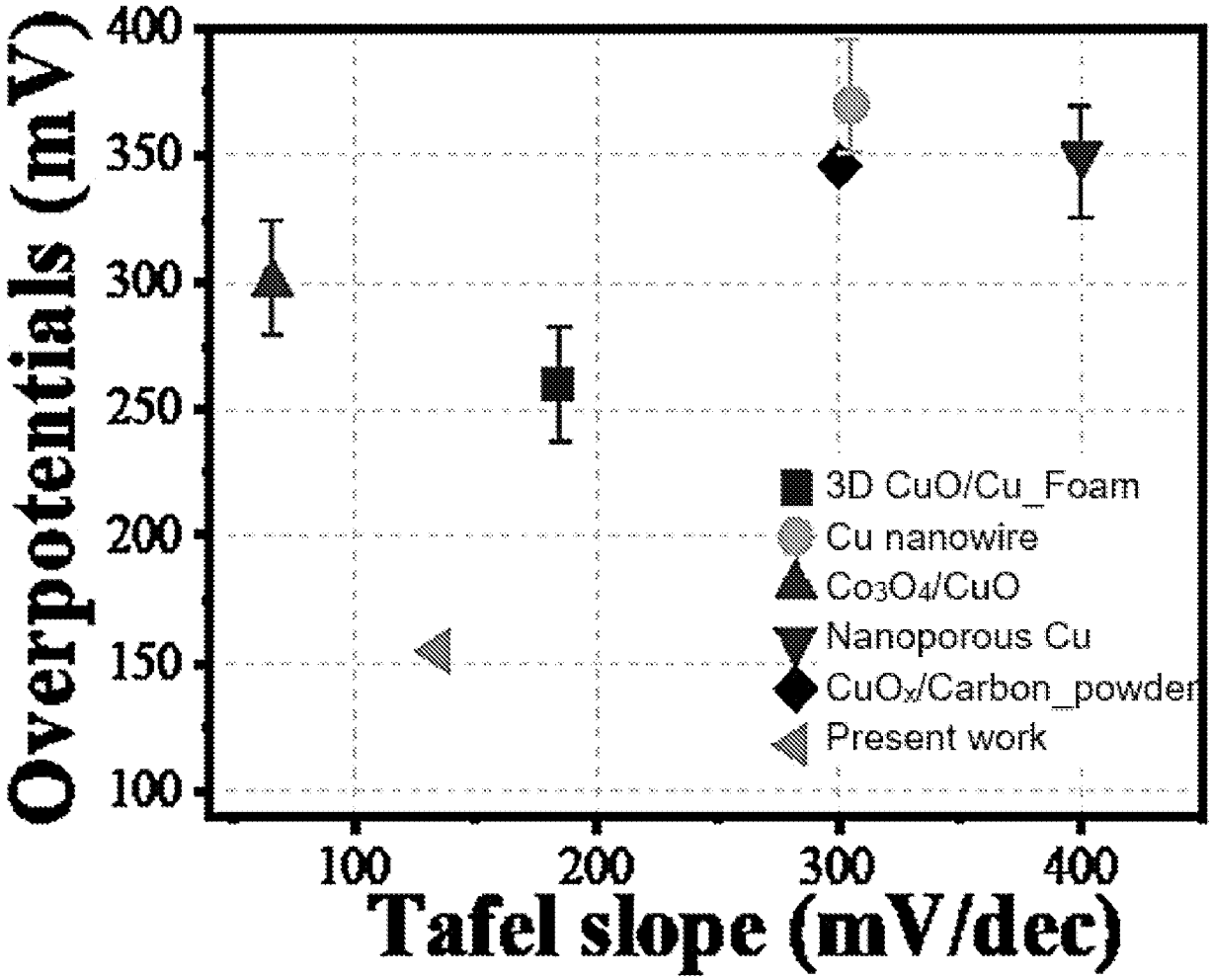
Overpotentials (mV)
400
350
300
250
200
150
100
100
200
300
400
Tafel slope (mV/dec)
3D CuO/Cu_Foam
Cu nanowire
Co3O4/CuO
Nanoporous Cu
CuOx/Carbon_powder
Present work

FIG. 1

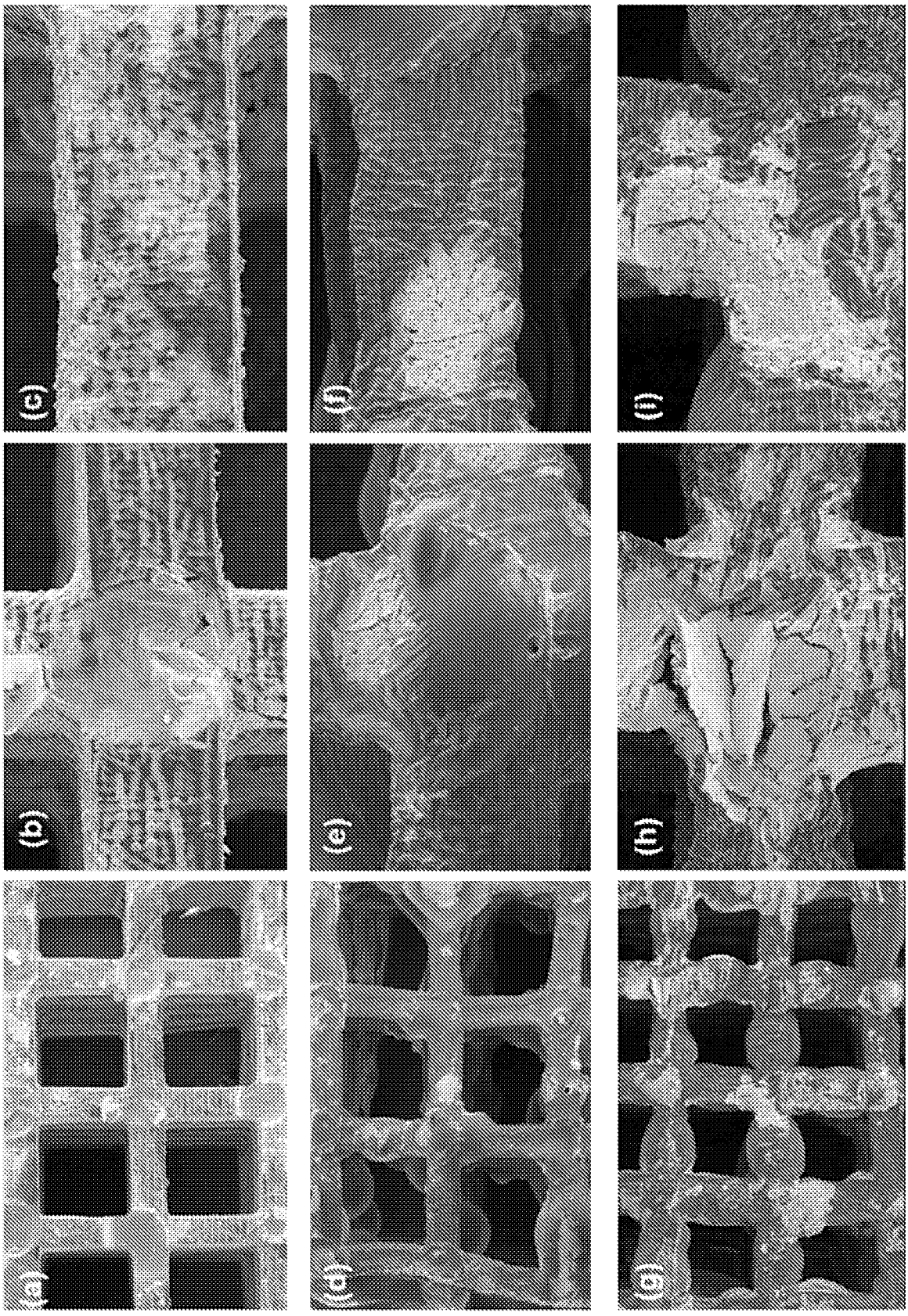

FIG. 2

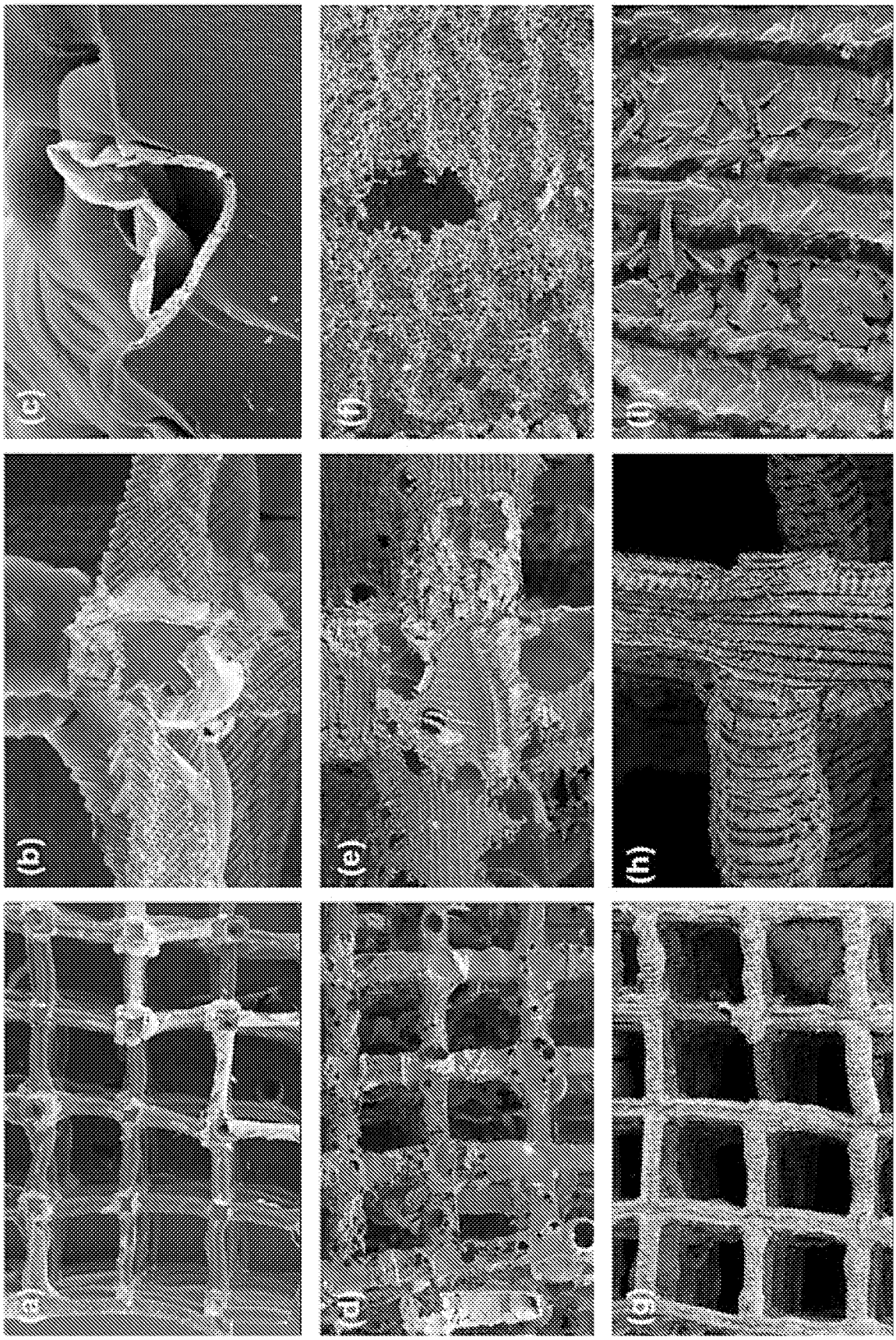

FIG. 3

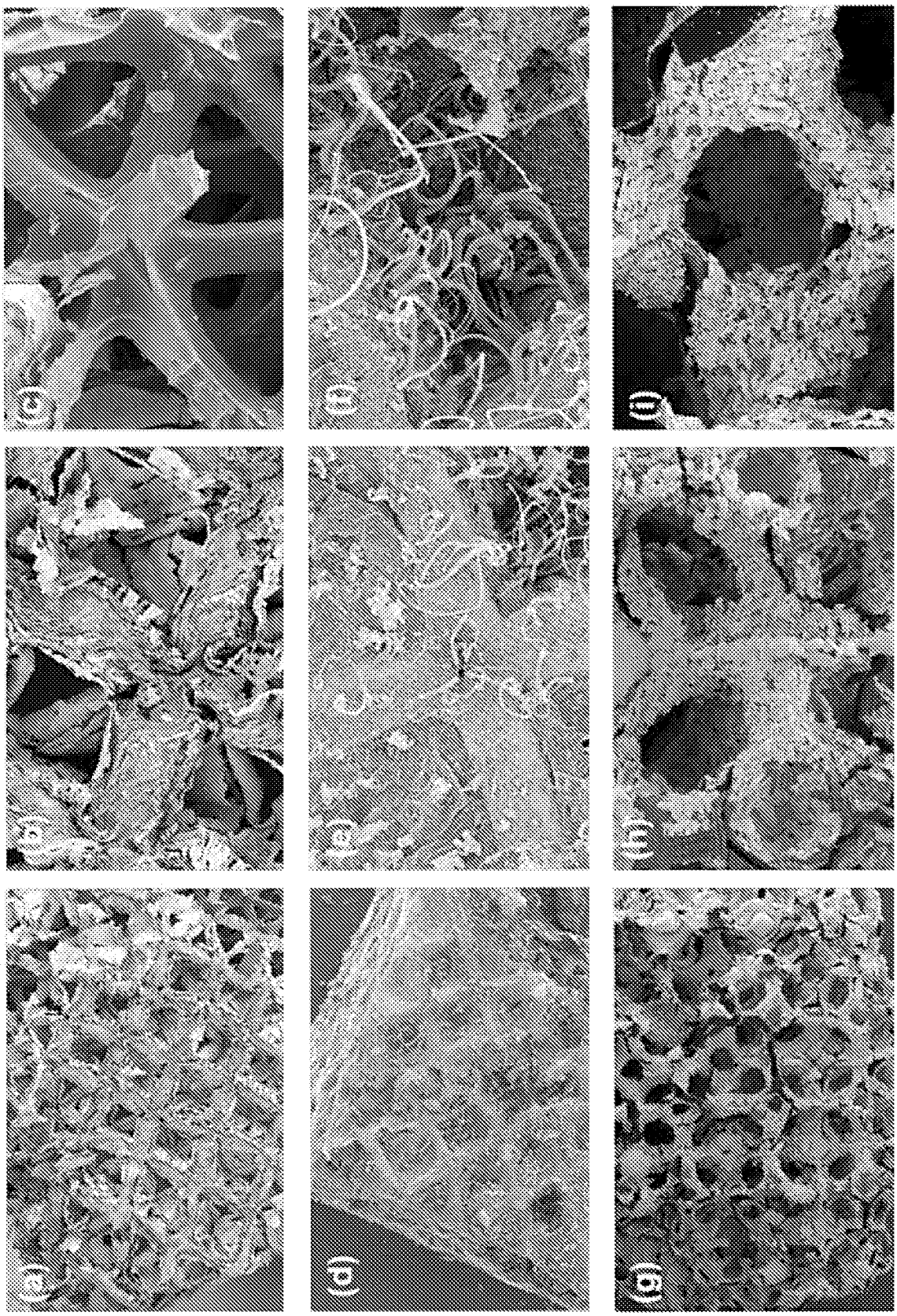

FIG. 4

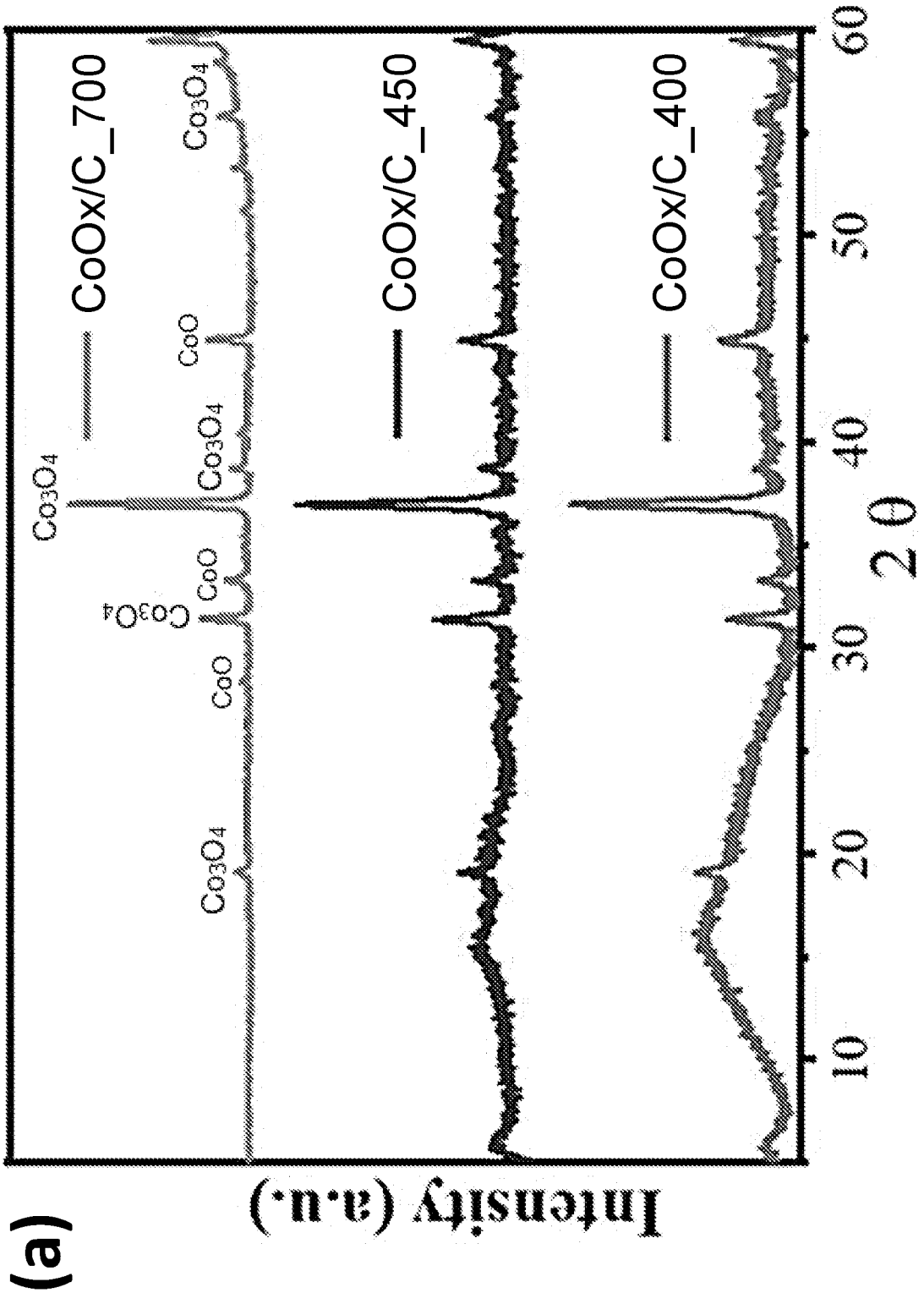
(a)
Intensity (a.u.)
2θ
10
20
30
40
50
60
CoOx/C_700
CoOx/C_450
CoOx/C_400
Co3O4
CoO

FIG. 5

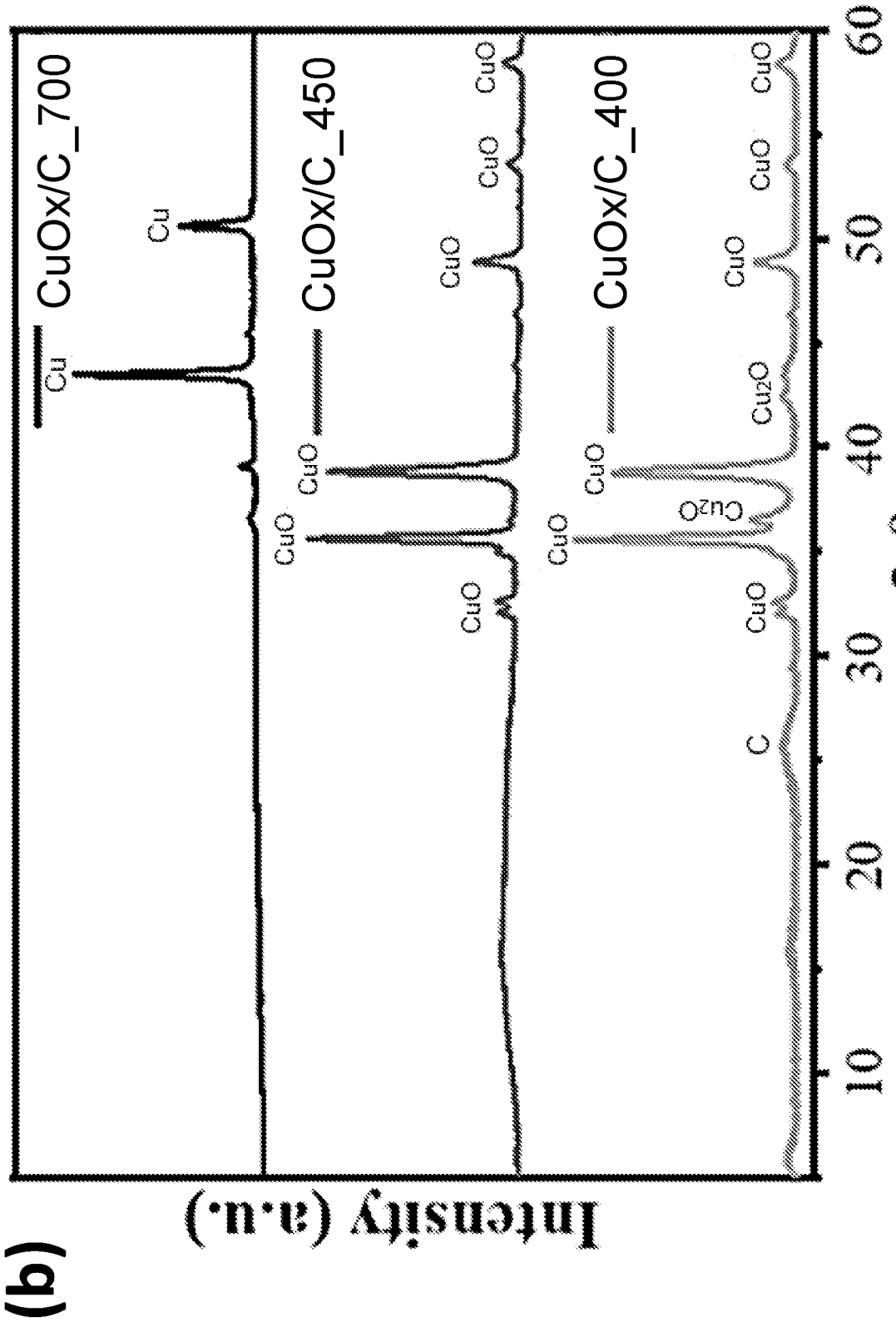

FIG. 5 (continued)

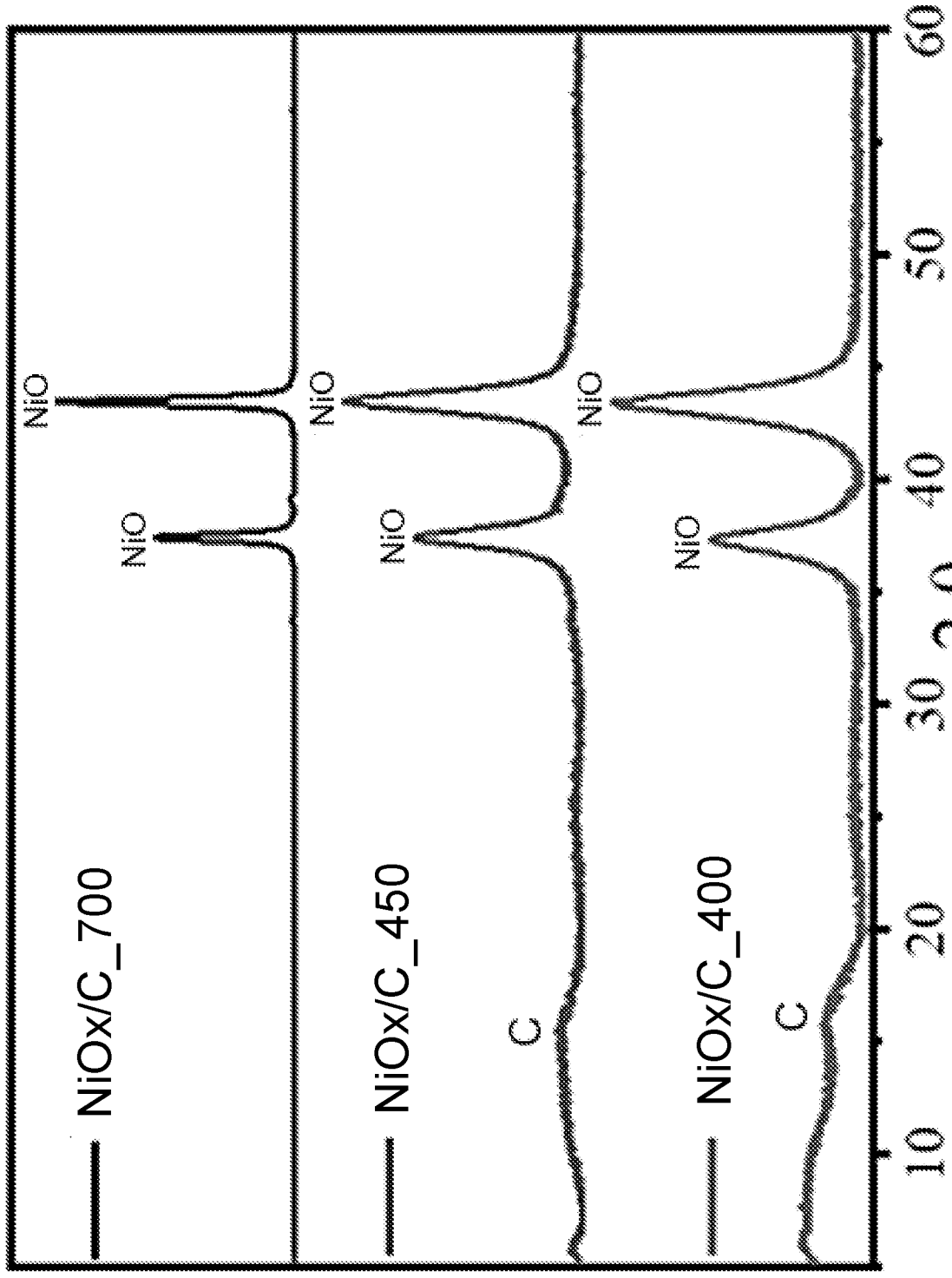

FIG. 5 (continued)

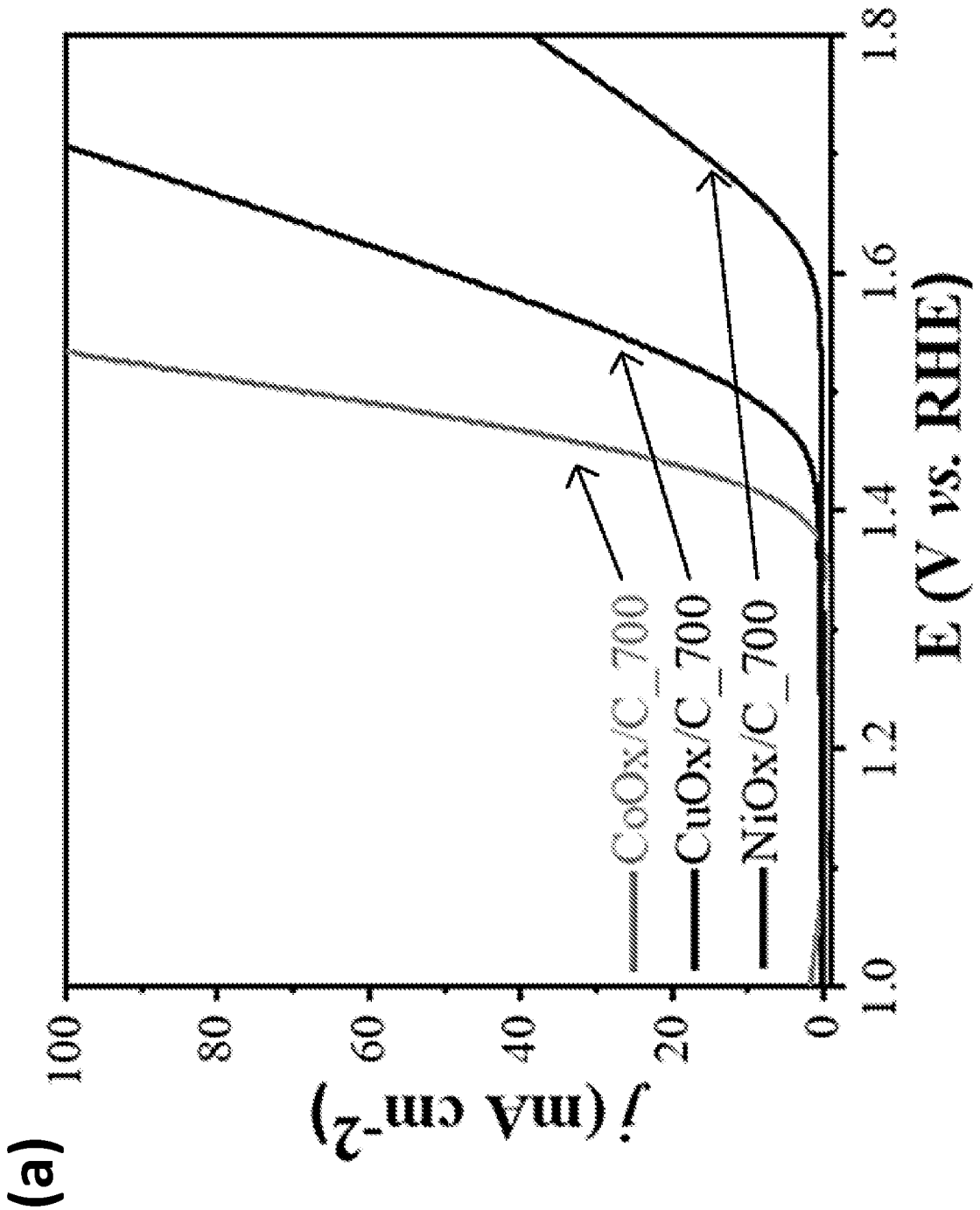
(a)
j (mA cm-2)
100
80
60
40
20
0
1.0
1.2
1.4
1.6
1.8
E (V vs. RHE)
CoOx/C_700
CuOx/C_700
NiOx/C_700

FIG. 6

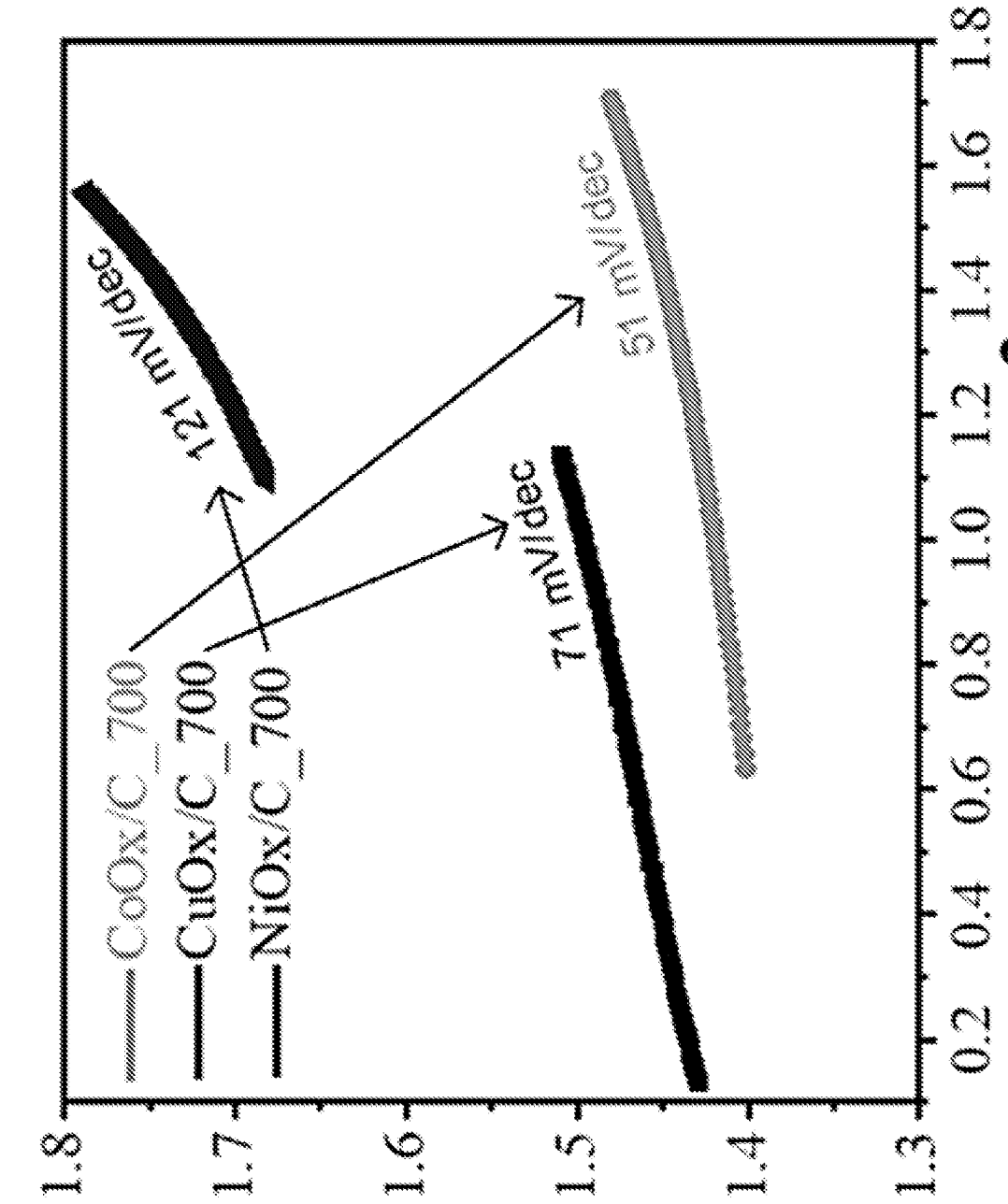

FIG. 6 (continued)

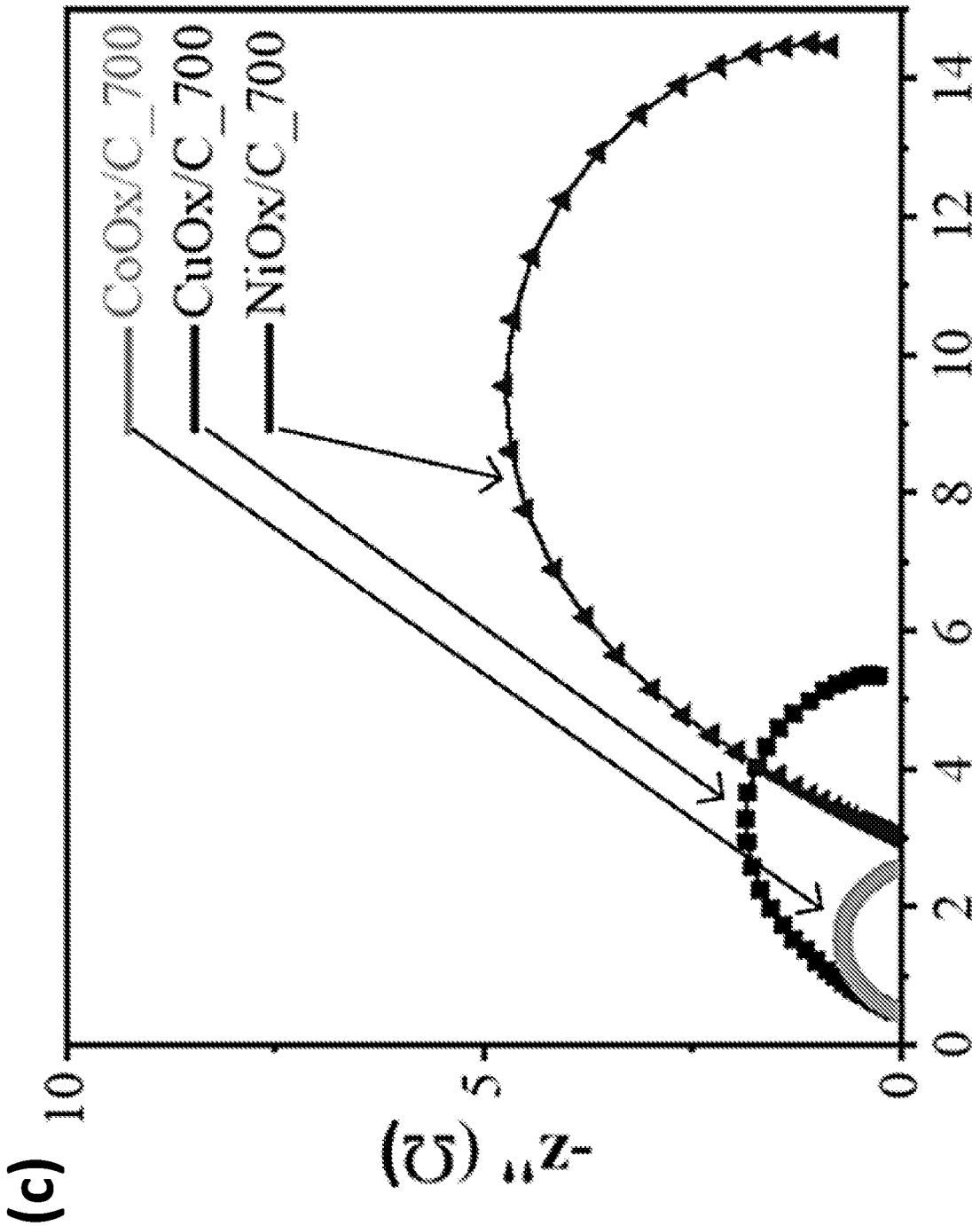

FIG. 6 (continued)

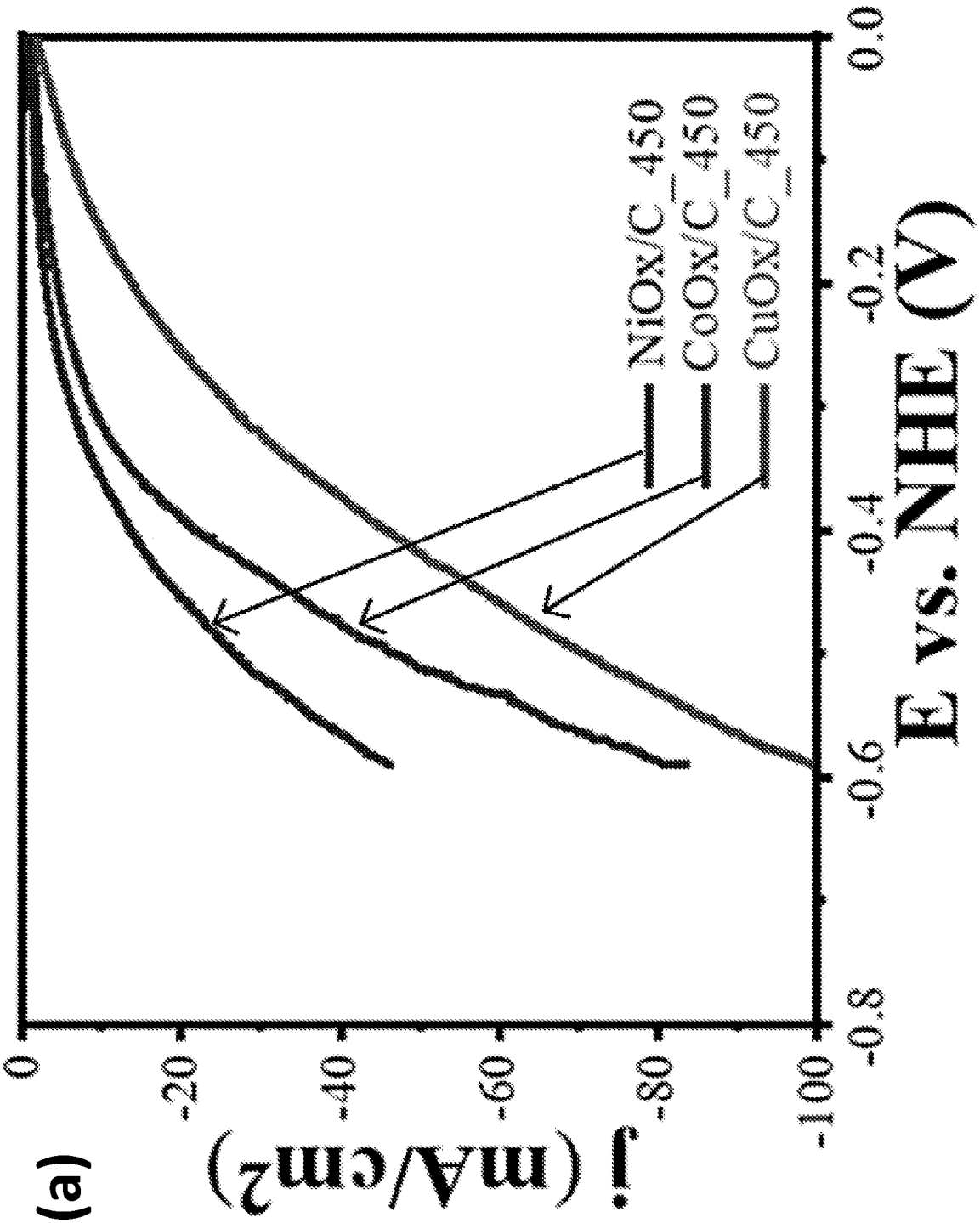
(a)
j (mA/cm²)
0
-20
-40
-60
-80
-100
-0.8
-0.6
-0.4
-0.2
0.0
E vs. NHE (V)
NiOx/C_450
CoOx/C_450
CuOx/C_450

FIG. 7

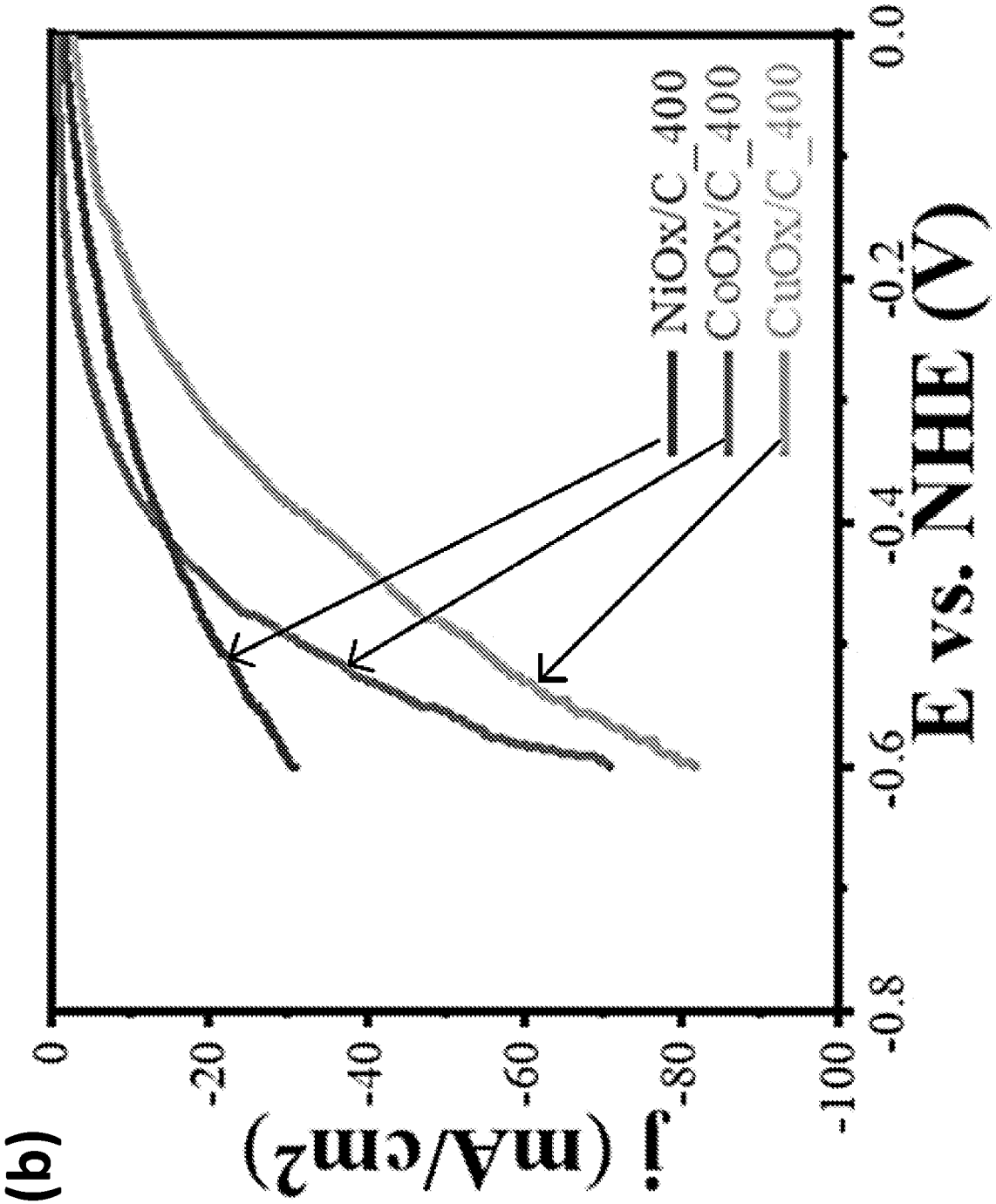

FIG. 7 (continued)

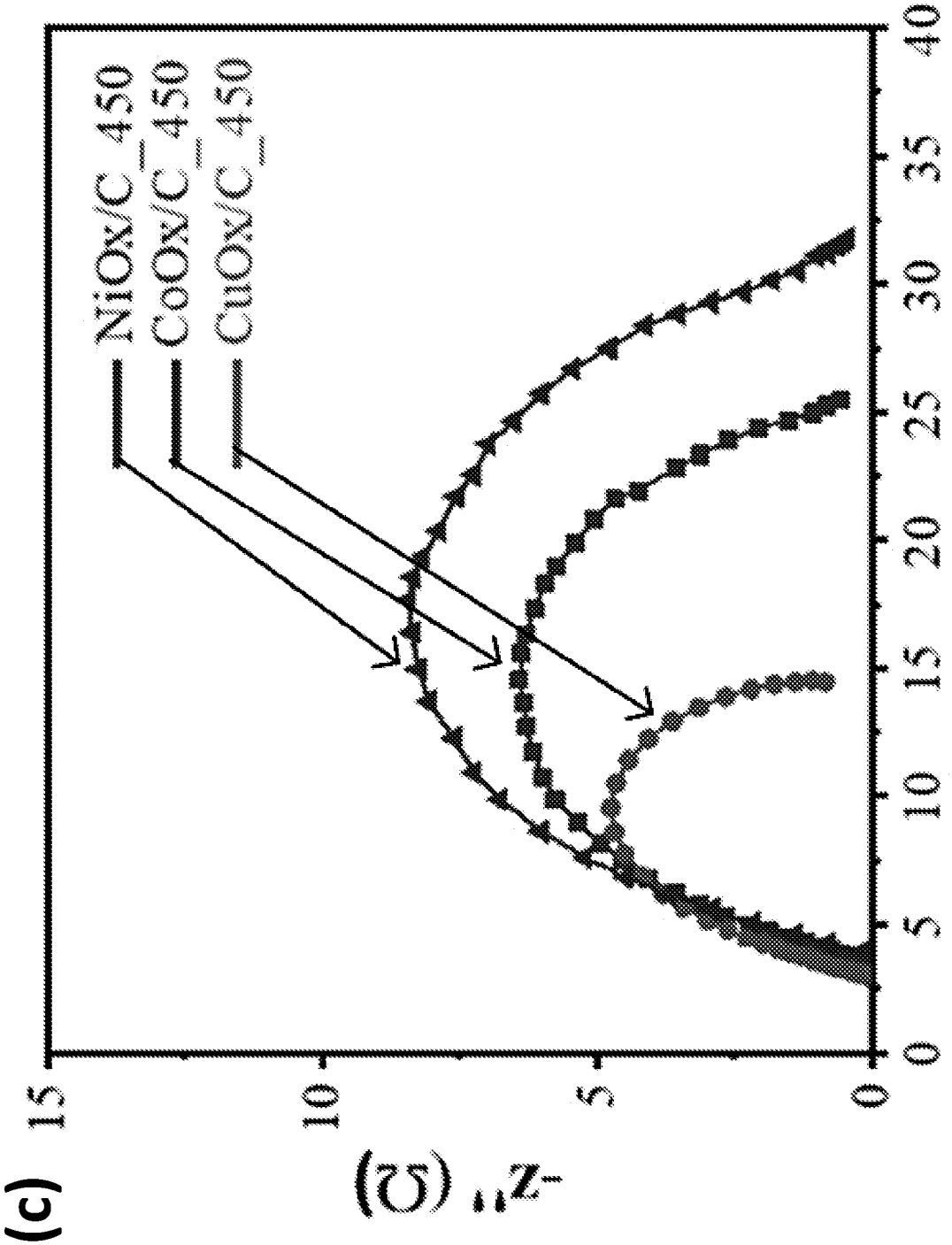

FIG. 7 (continued)

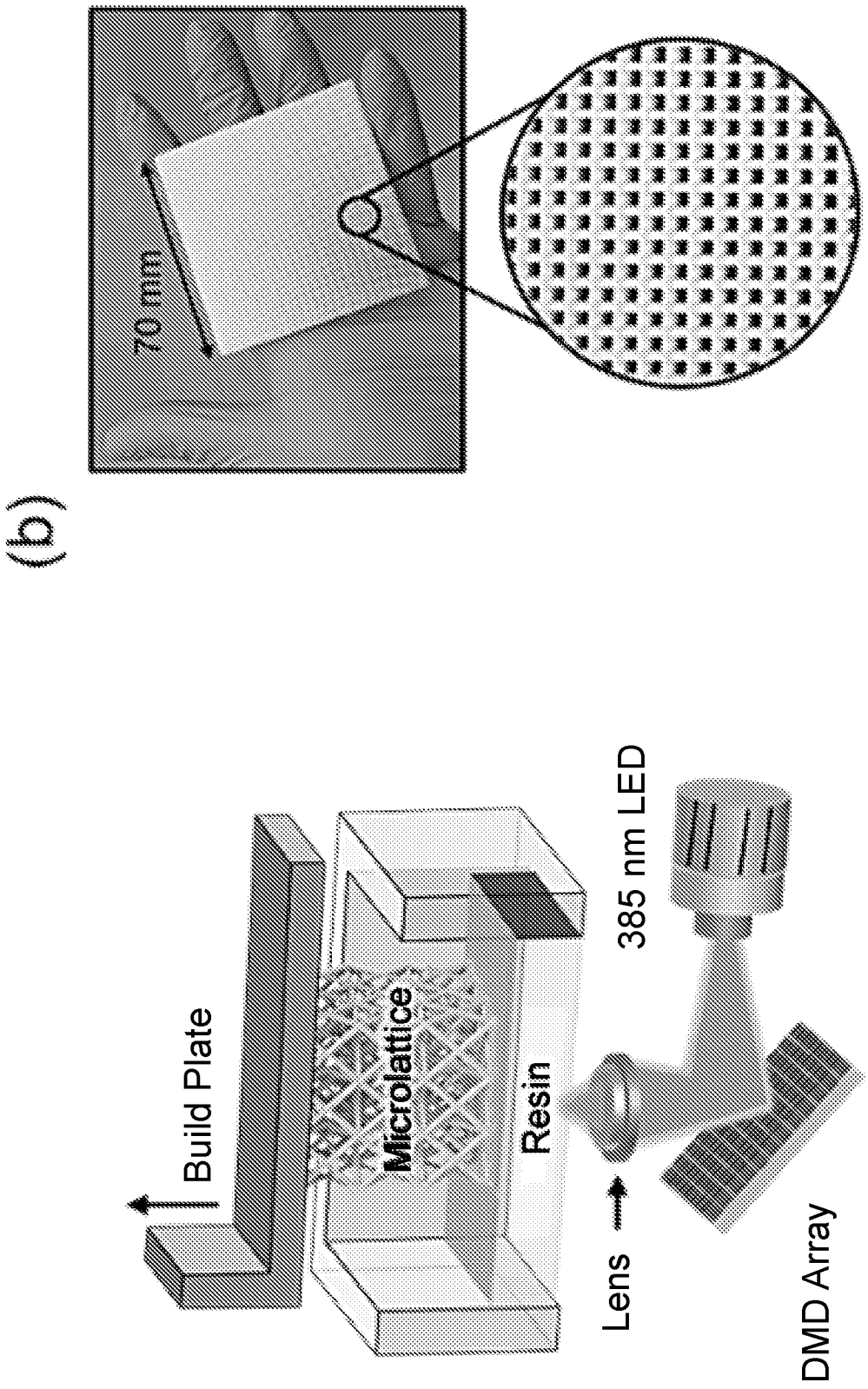
(b)
70 mm
(a)
Build Plate
Microlattice
Resin
385 nm LED
Lens
DMD Array

FIG. 8

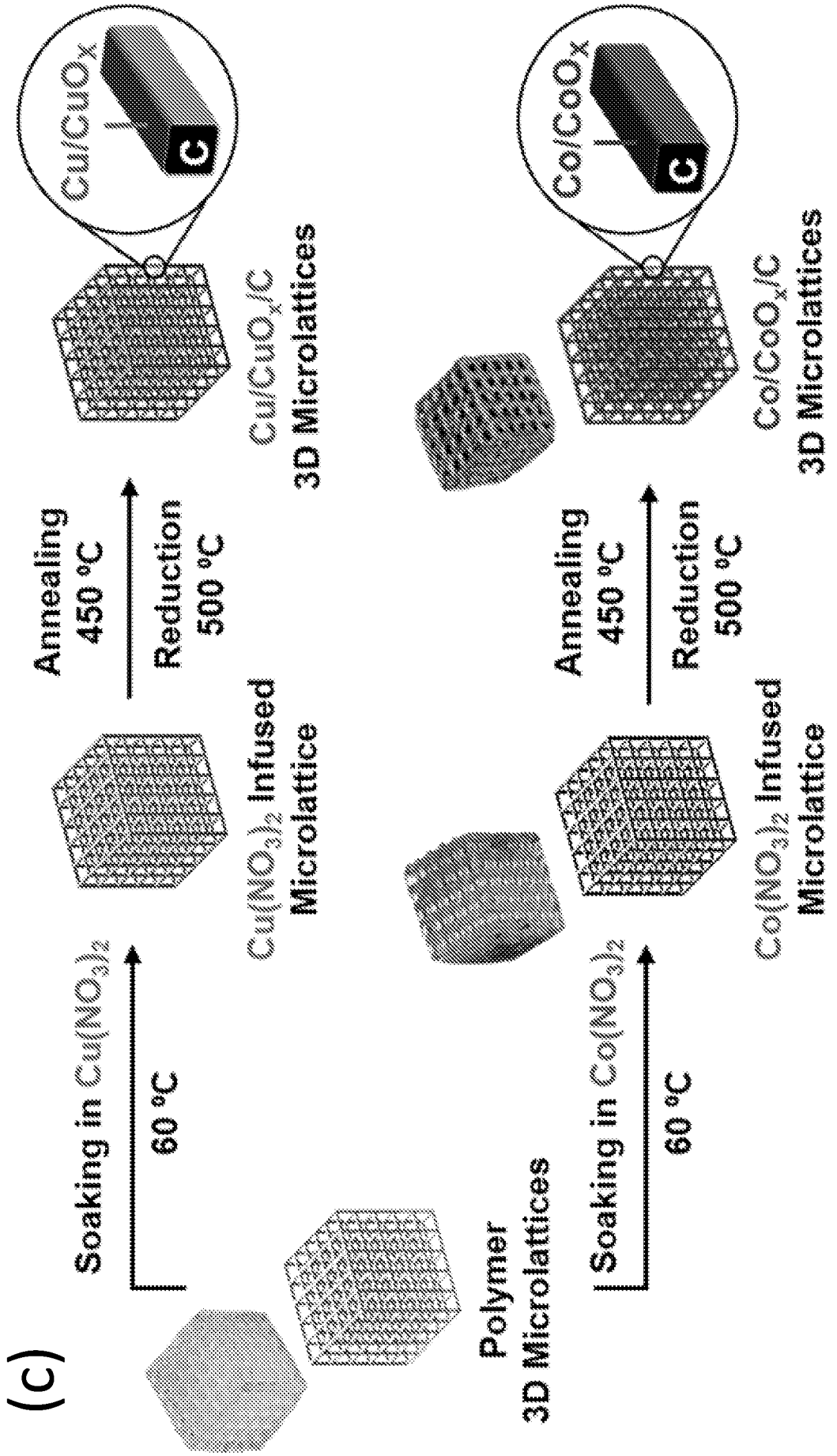

FIG. 8 (continued)

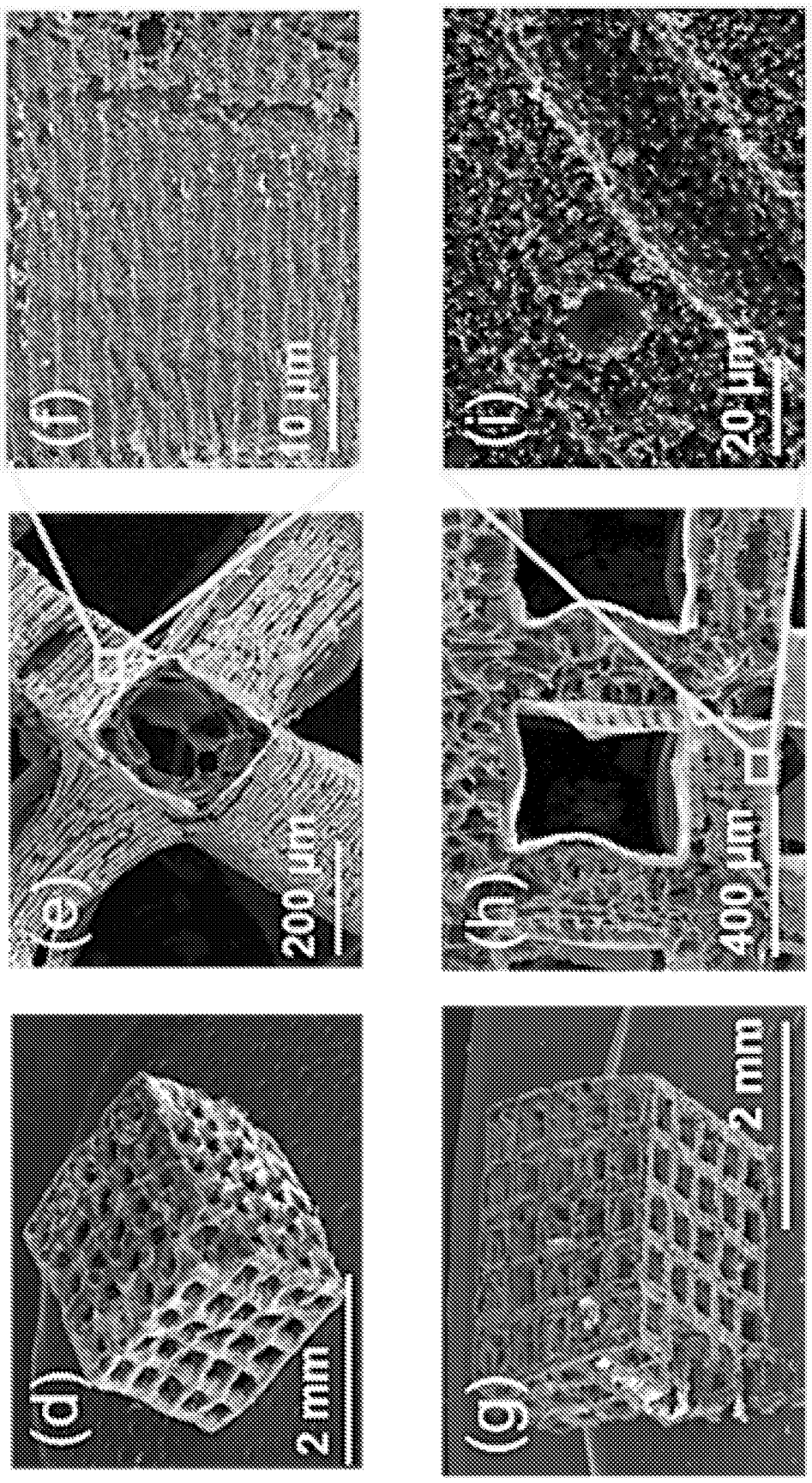

FIG. 8 (continued)

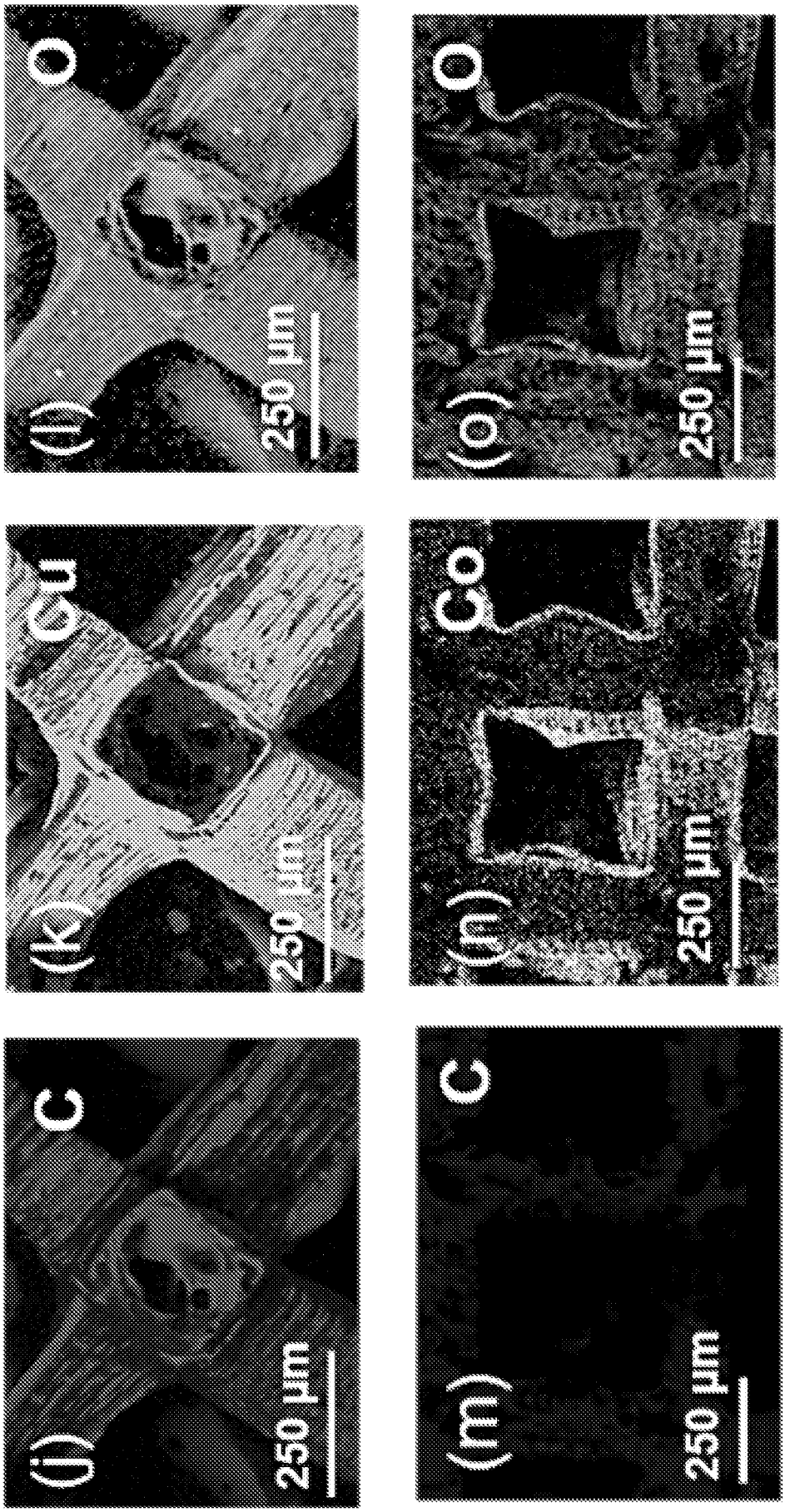

FIG. 8 (continued)

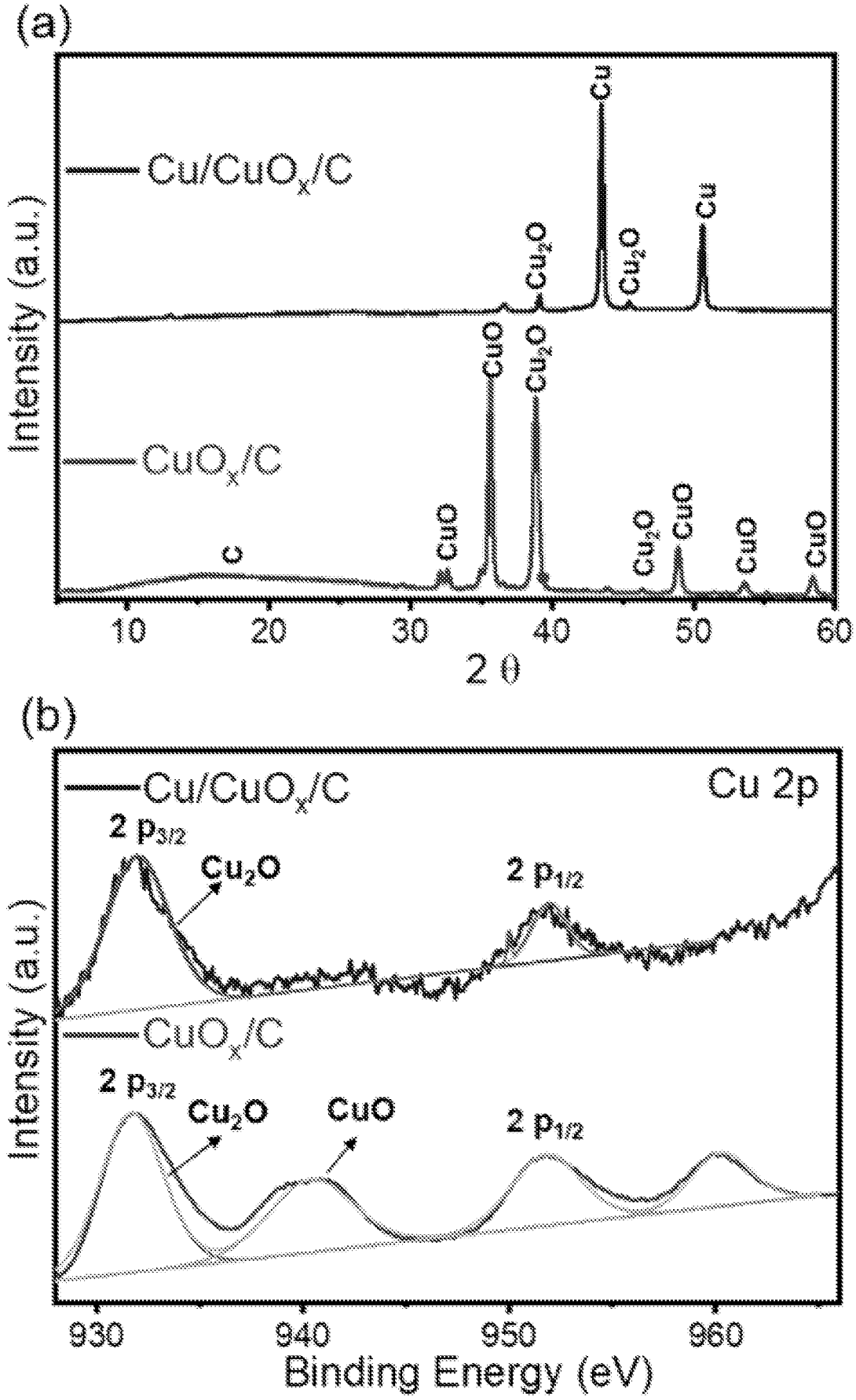
(a)
Cu/CuOx/C
CuOx/C
Intensity (a.u.)
Cu
Cu2O
CuO
C
10
20
30
40
50
60
2 θ
(b)
Cu/CuOx/C
Cu 2p
2 p3/2
Cu2O
2 p1/2
CuOx/C
CuO
930
940
950
960
Binding Energy (eV)

FIG. 9

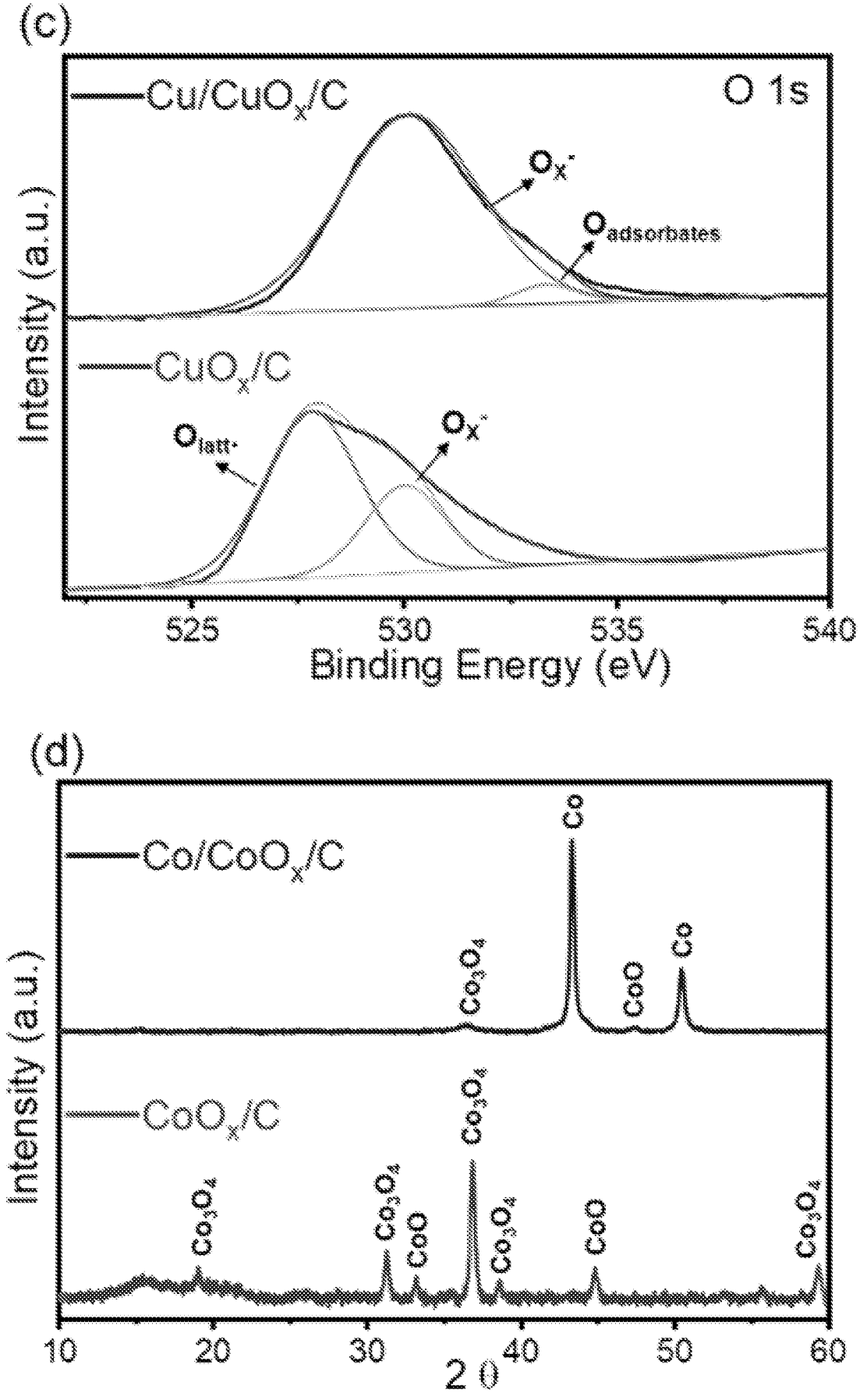

FIG. 9 (continued)

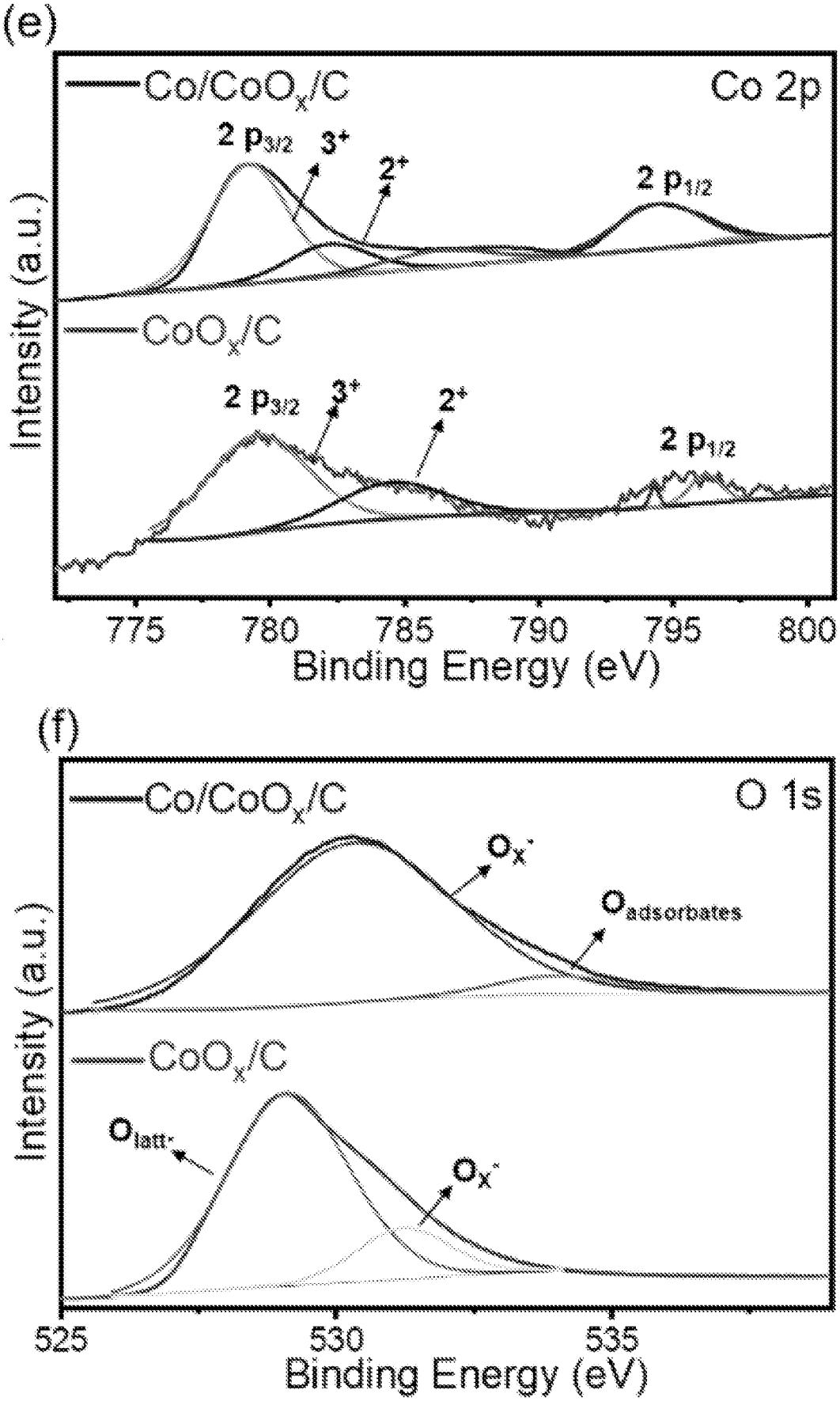

FIG. 9 (continued)

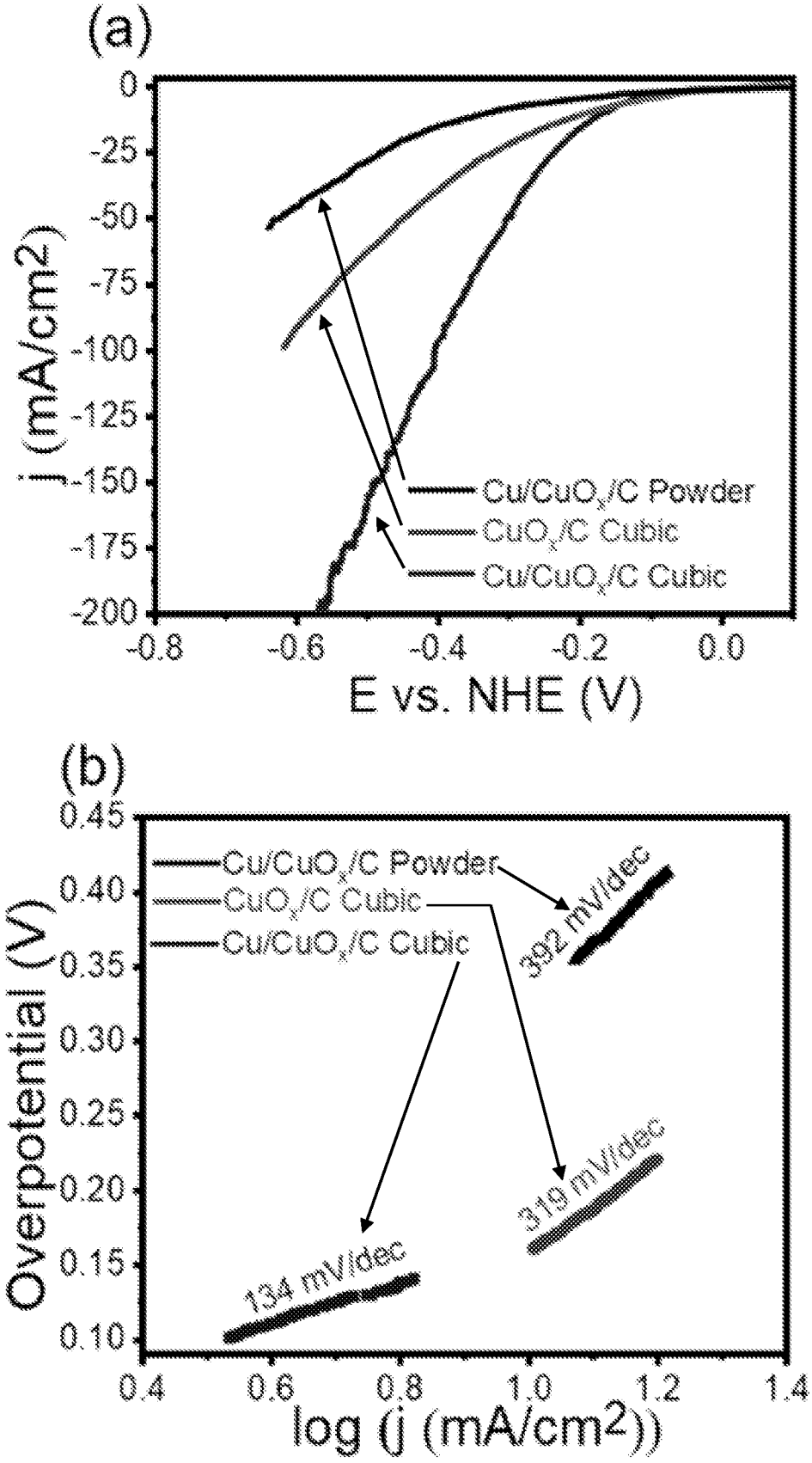
(a)
j (mA/cm2)
E vs. NHE (V)
Cu/CuOx/C Powder
CuOx/C Cubic
Cu/CuOx/C Cubic
(b)
Overpotential (V)
log (j (mA/cm2))
Cu/CuOx/C Powder
CuOx/C Cubic
Cu/CuOx/C Cubic
392 mV/dec
319 mV/dec
134 mV/dec

FIG. 10

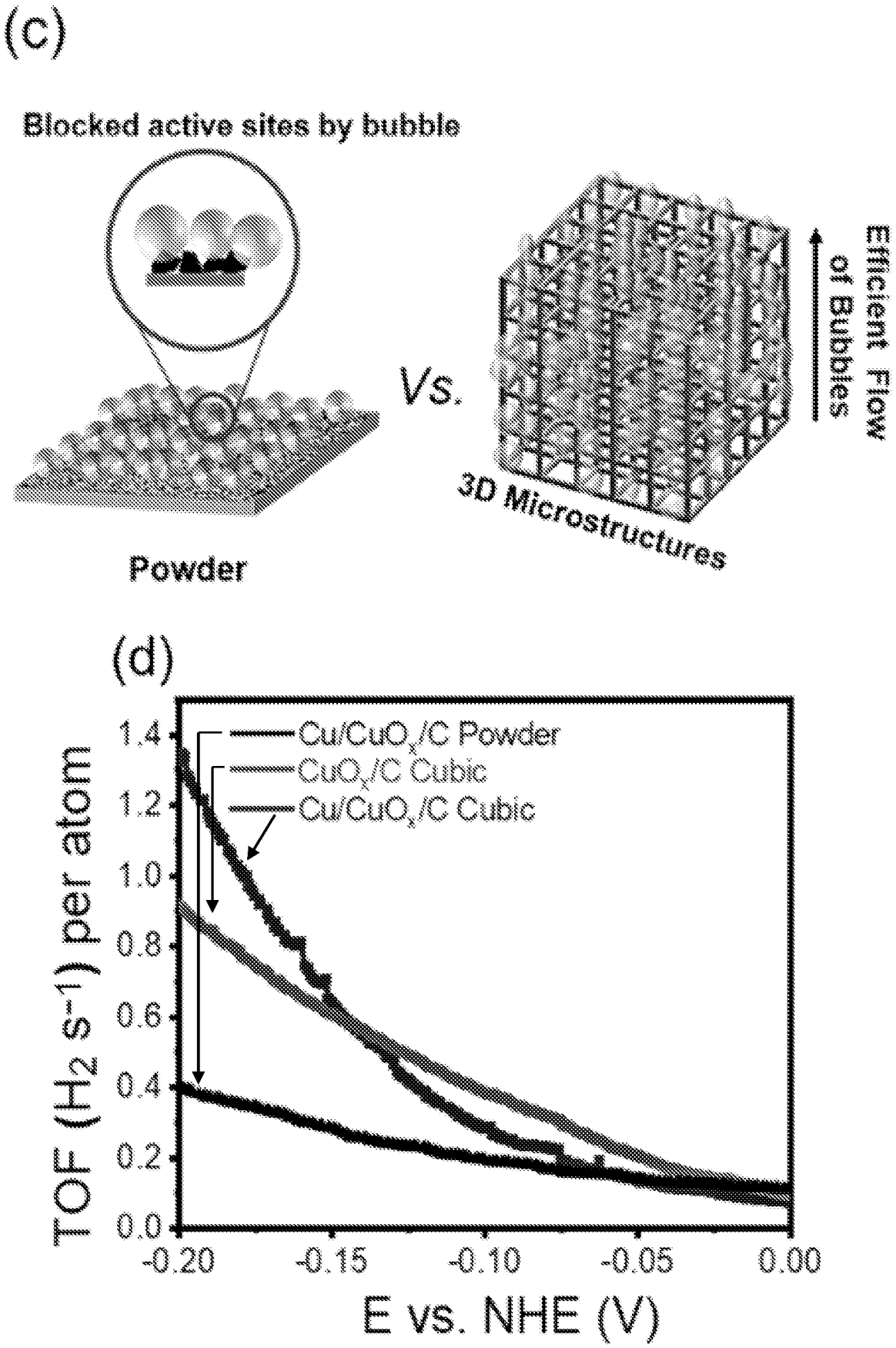

FIG. 10 (continued)

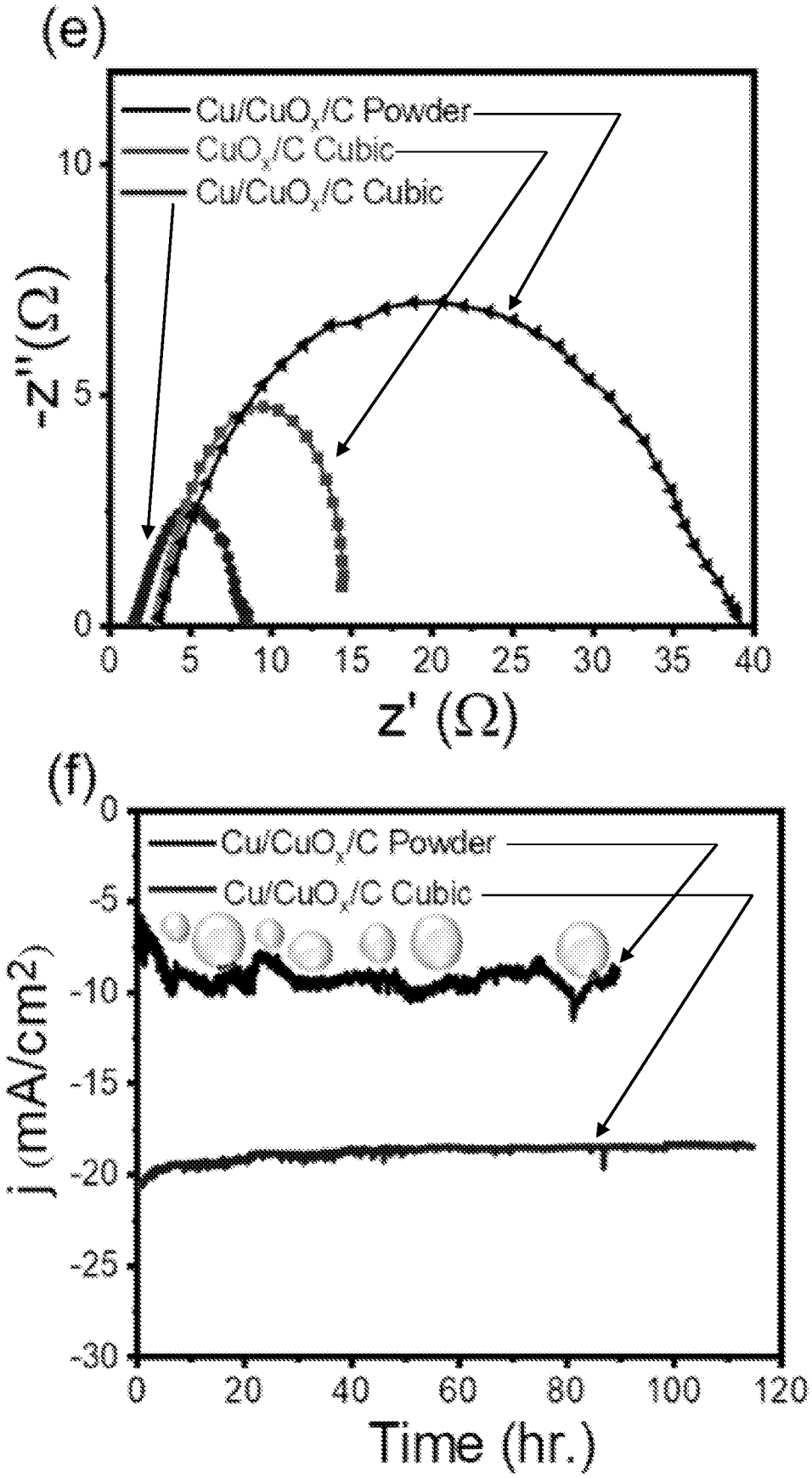

FIG. 10 (continued)

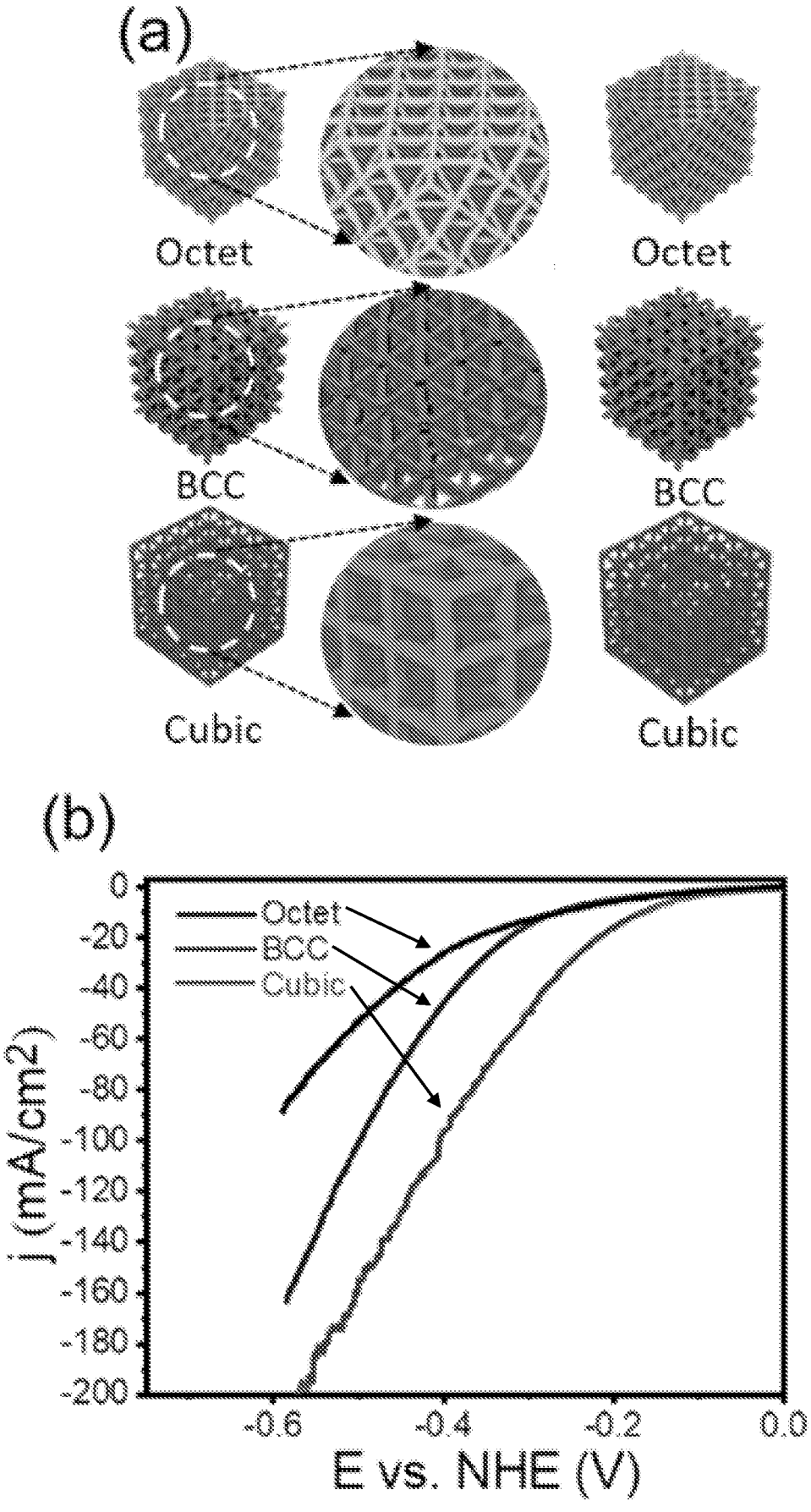
(a)
Octet
Octet
BCC
BCC
Cubic
Cubic
(b)
Octet
BCC
Cubic
j (mA/cm2)
0
-20
-40
-60
-80
-100
-120
-140
-160
-180
-200
-0.6
-0.4
-0.2
0.0
E vs. NHE (V)

FIG. 11

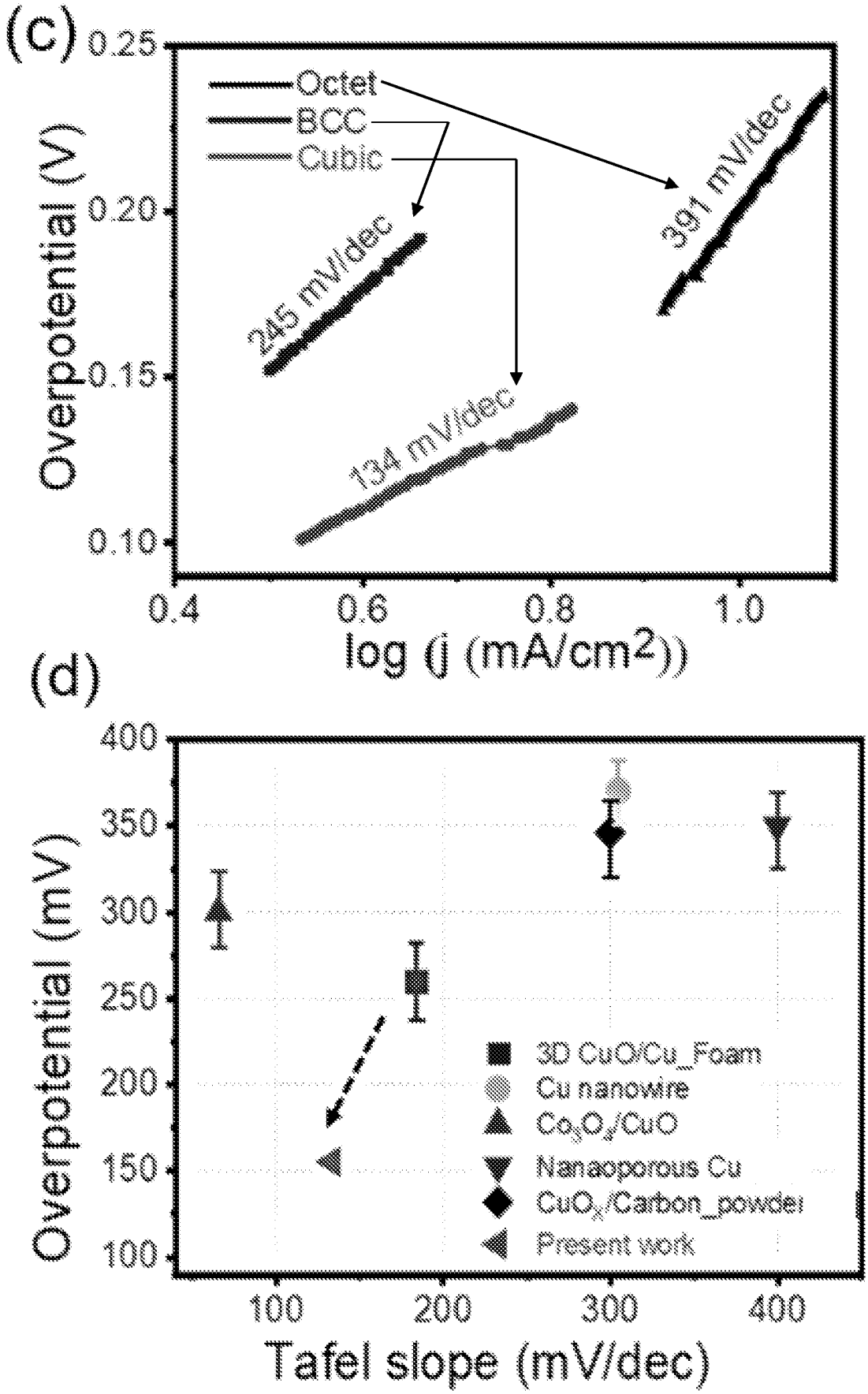

FIG. 11 (continued)

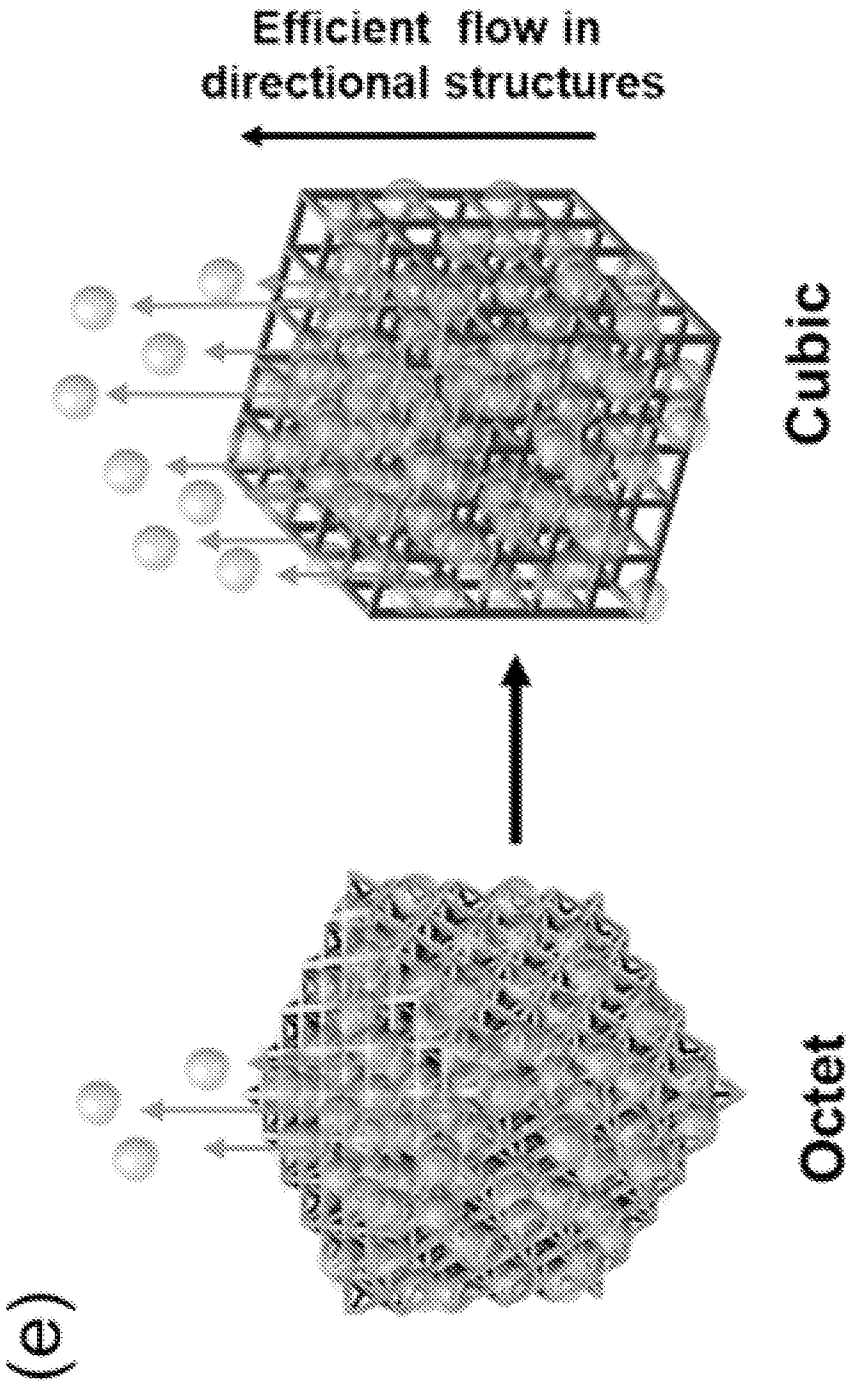

FIG. 11 (continued)

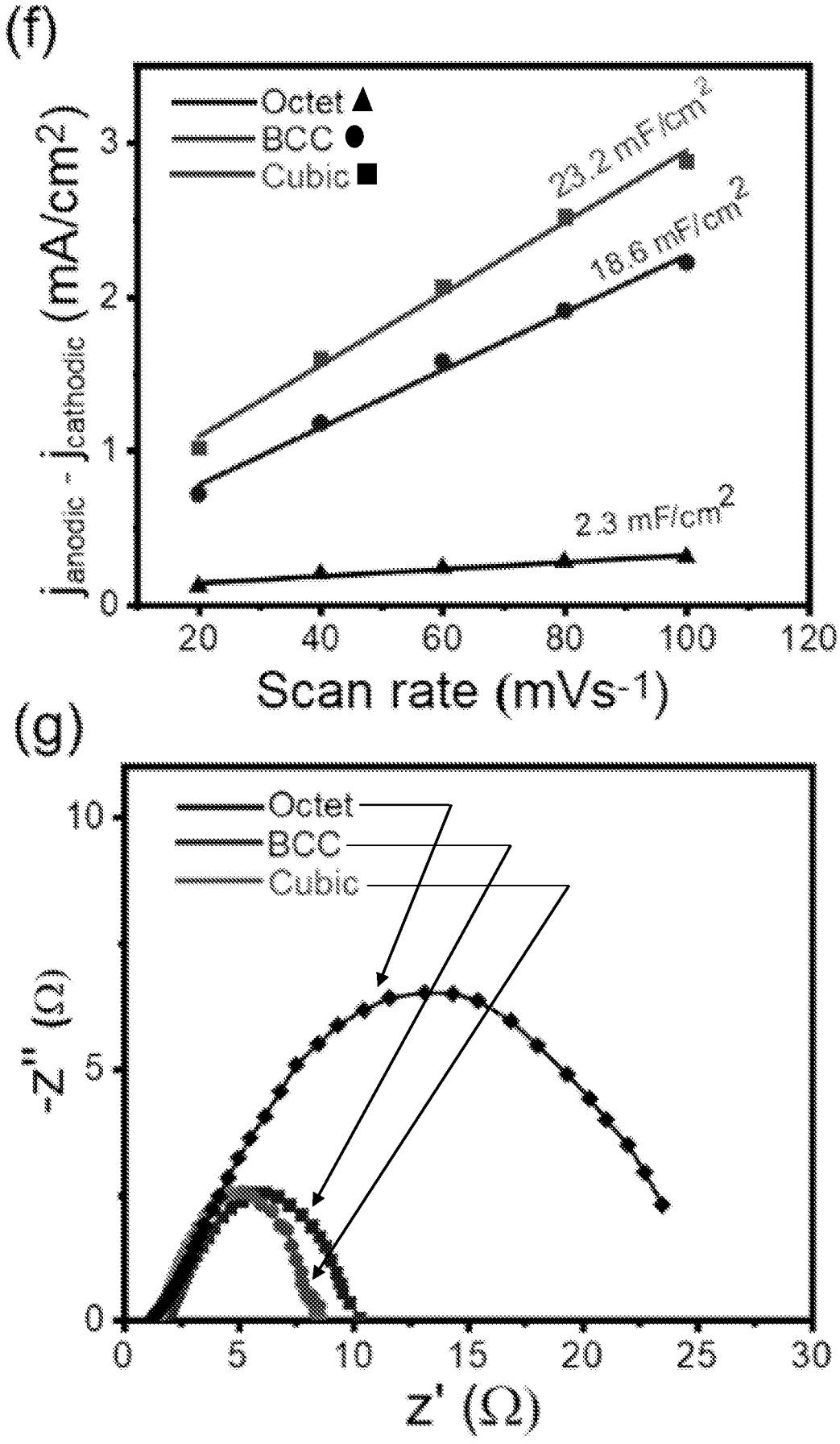

FIG. 11 (continued)

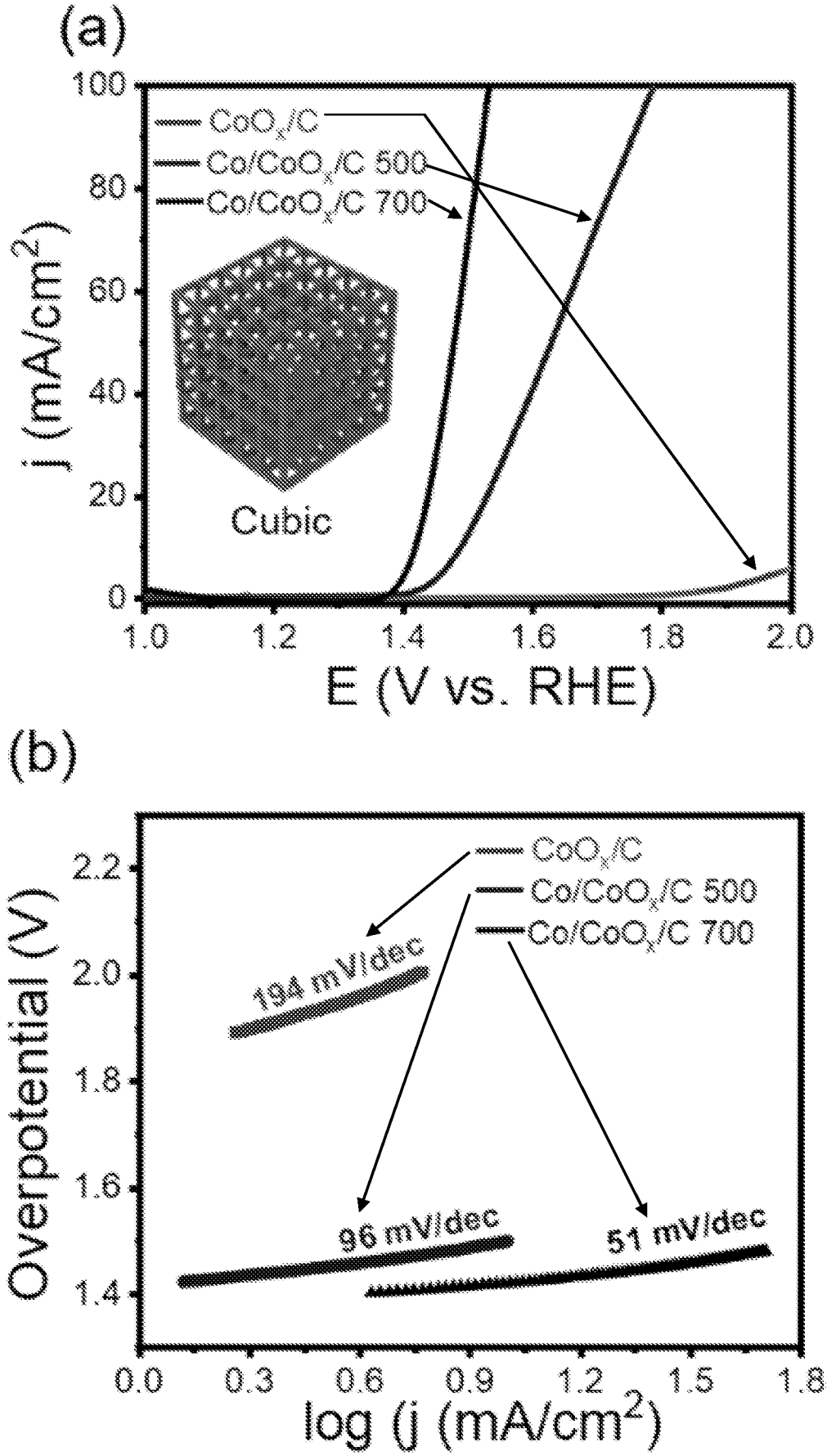
(a)
100
80
60
40
20
0
j (mA/cm^2)
CoO_x/C
Co/CoO_x/C 500
Co/CoO_x/C 700
Cubic
1.0
1.2
1.4
1.6
1.8
2.0
E (V vs. RHE)
(b)
2.2
2.0
1.8
1.6
1.4
Overpotential (V)
194 mV/dec
96 mV/dec
51 mV/dec
0.0
0.3
0.6
0.9
1.2
1.5
1.8
log (j (mA/cm^2)

FIG. 12

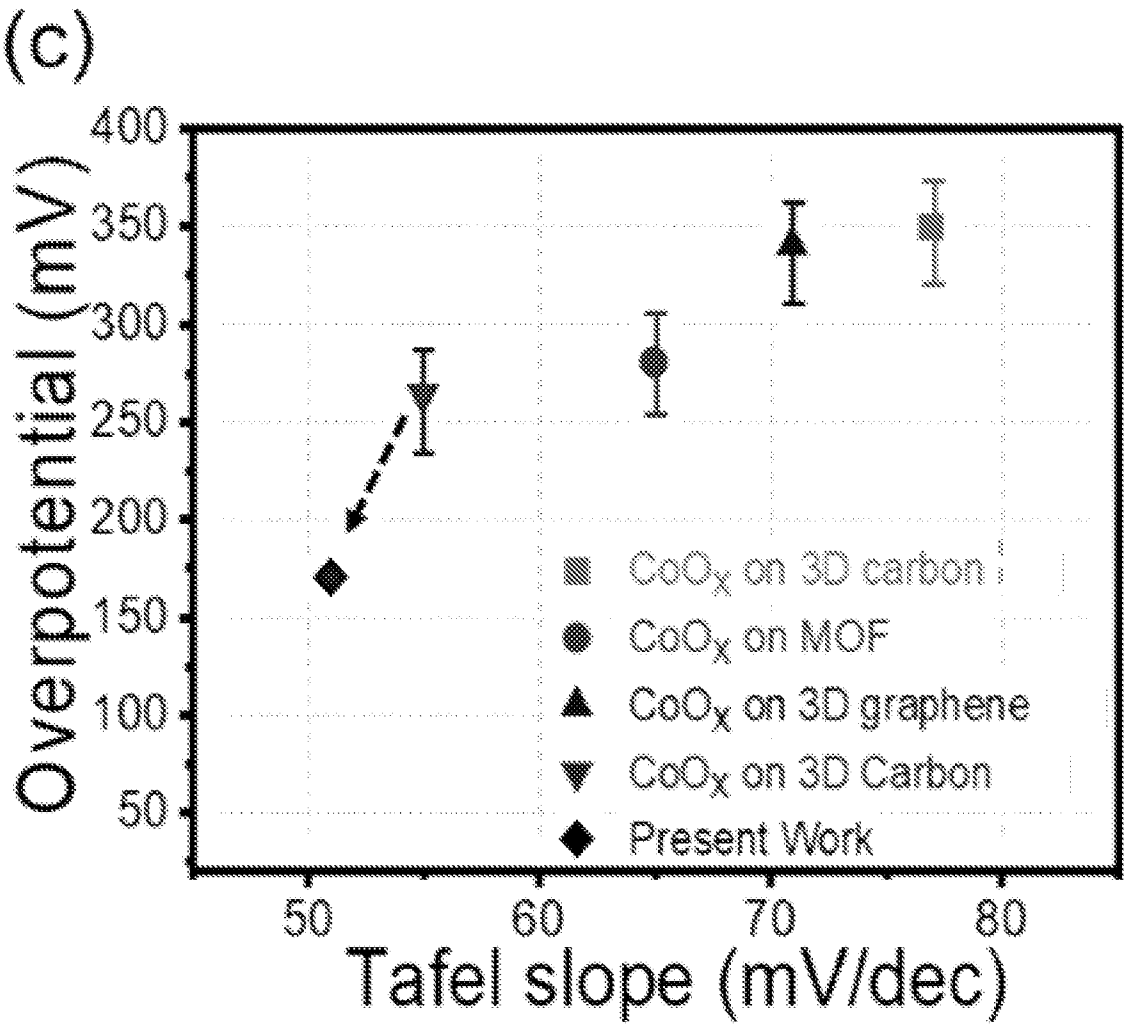

FIG. 12 (continued)

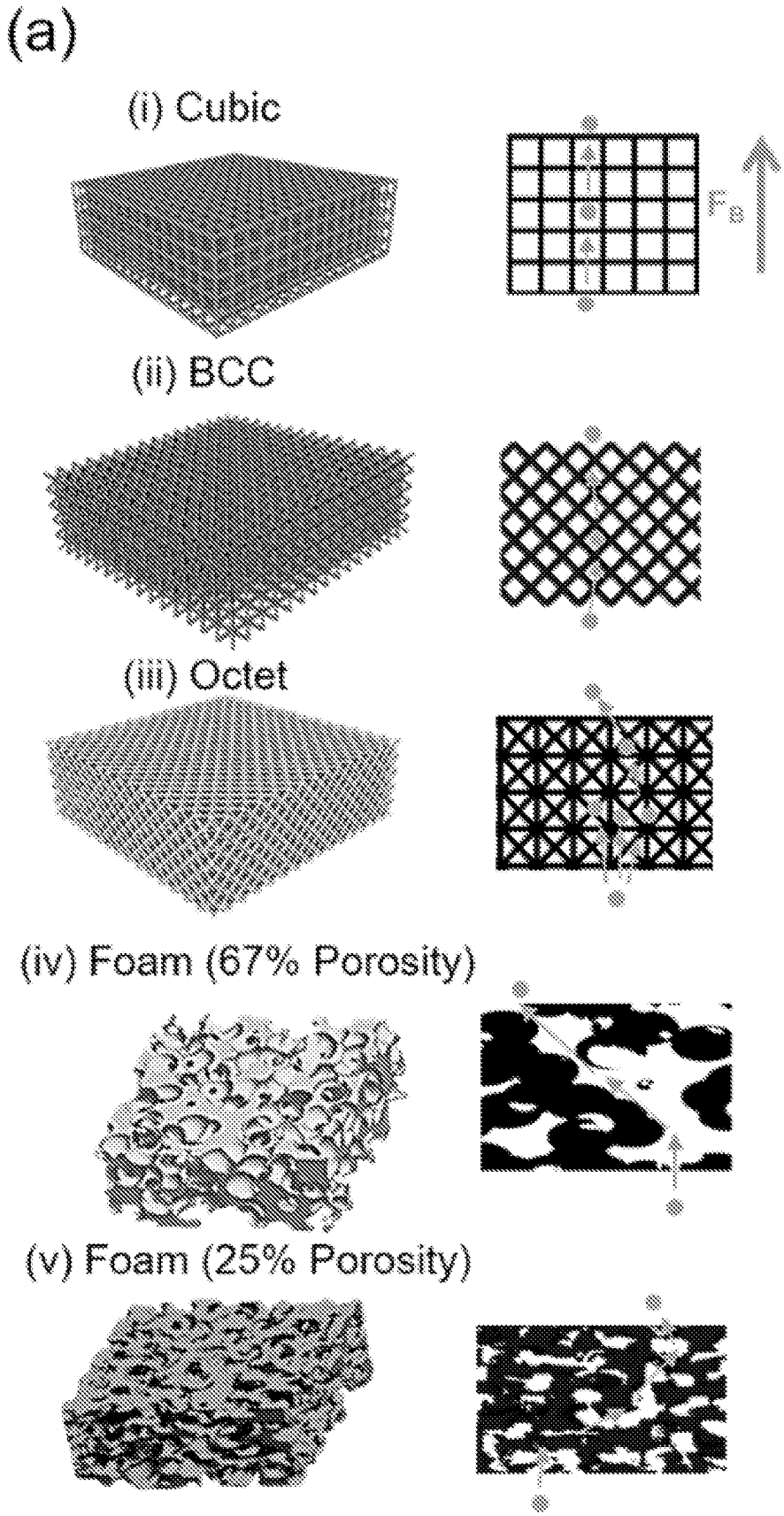
(a)
(i) Cubic
F_D
(ii) BCC
(iii) Octet
(iv) Foam (67% Porosity)
(v) Foam (25% Porosity)

FIG. 13

(b)

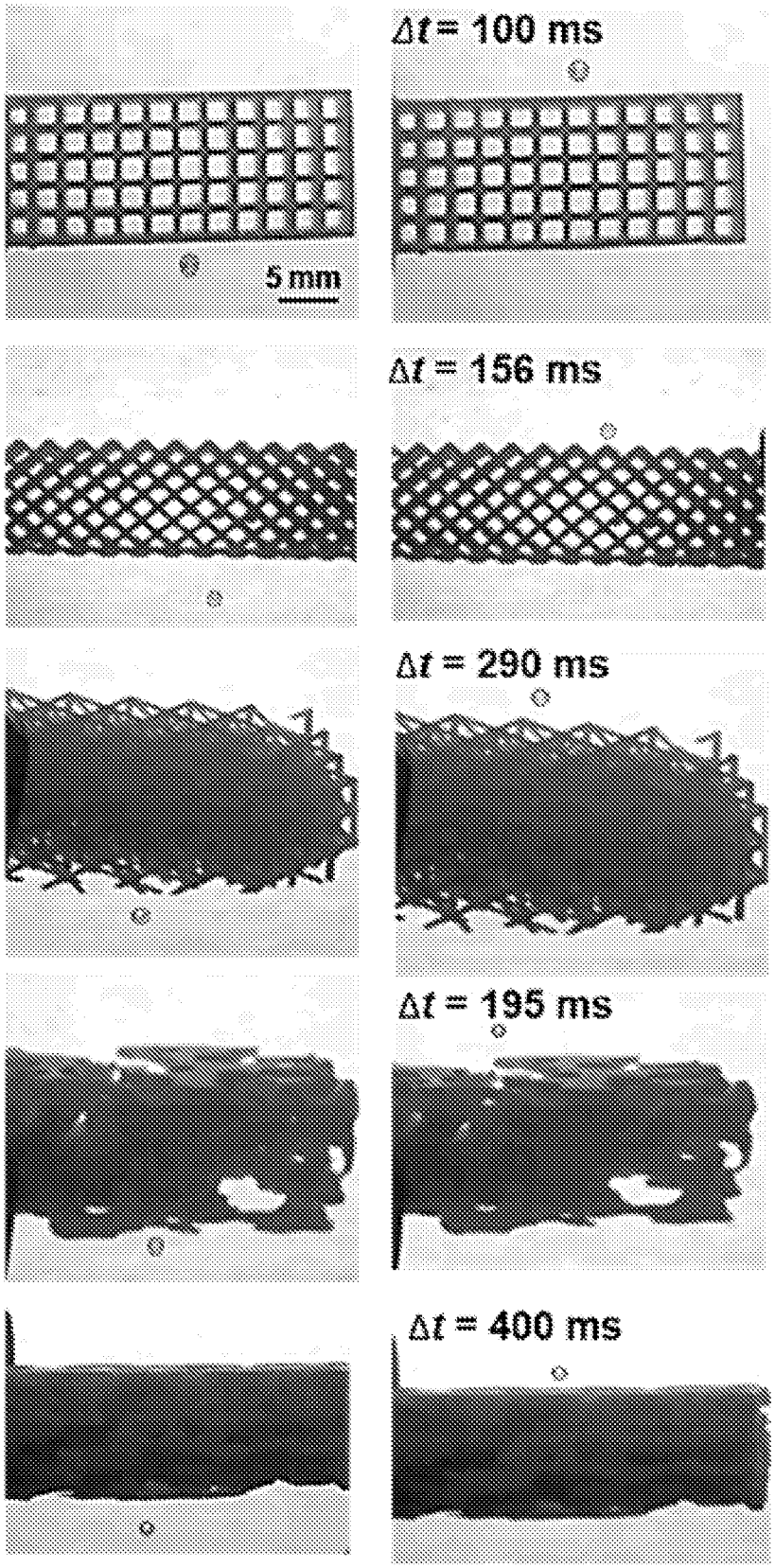

FIG. 13 (continued)

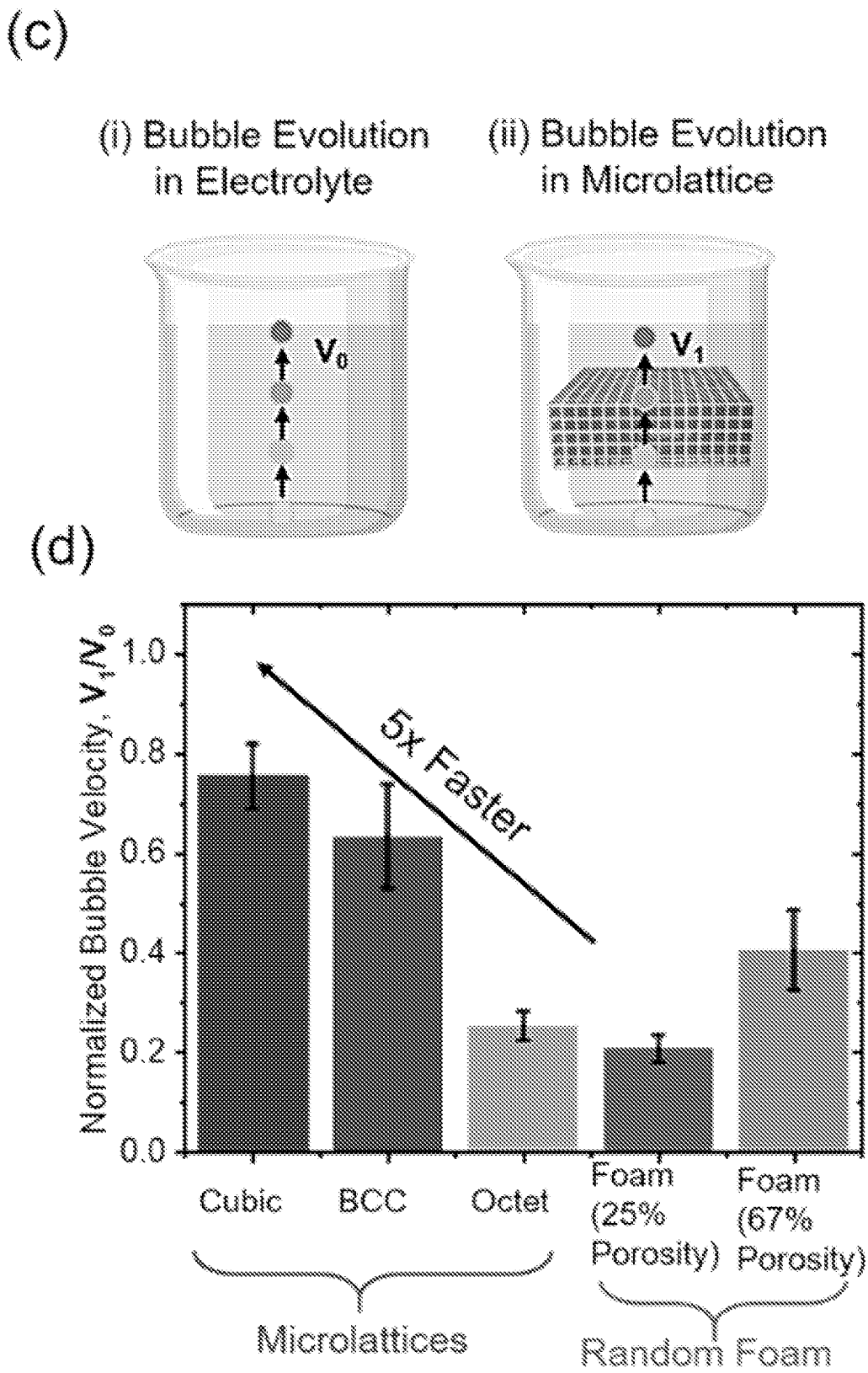

FIG. 13 (continued)

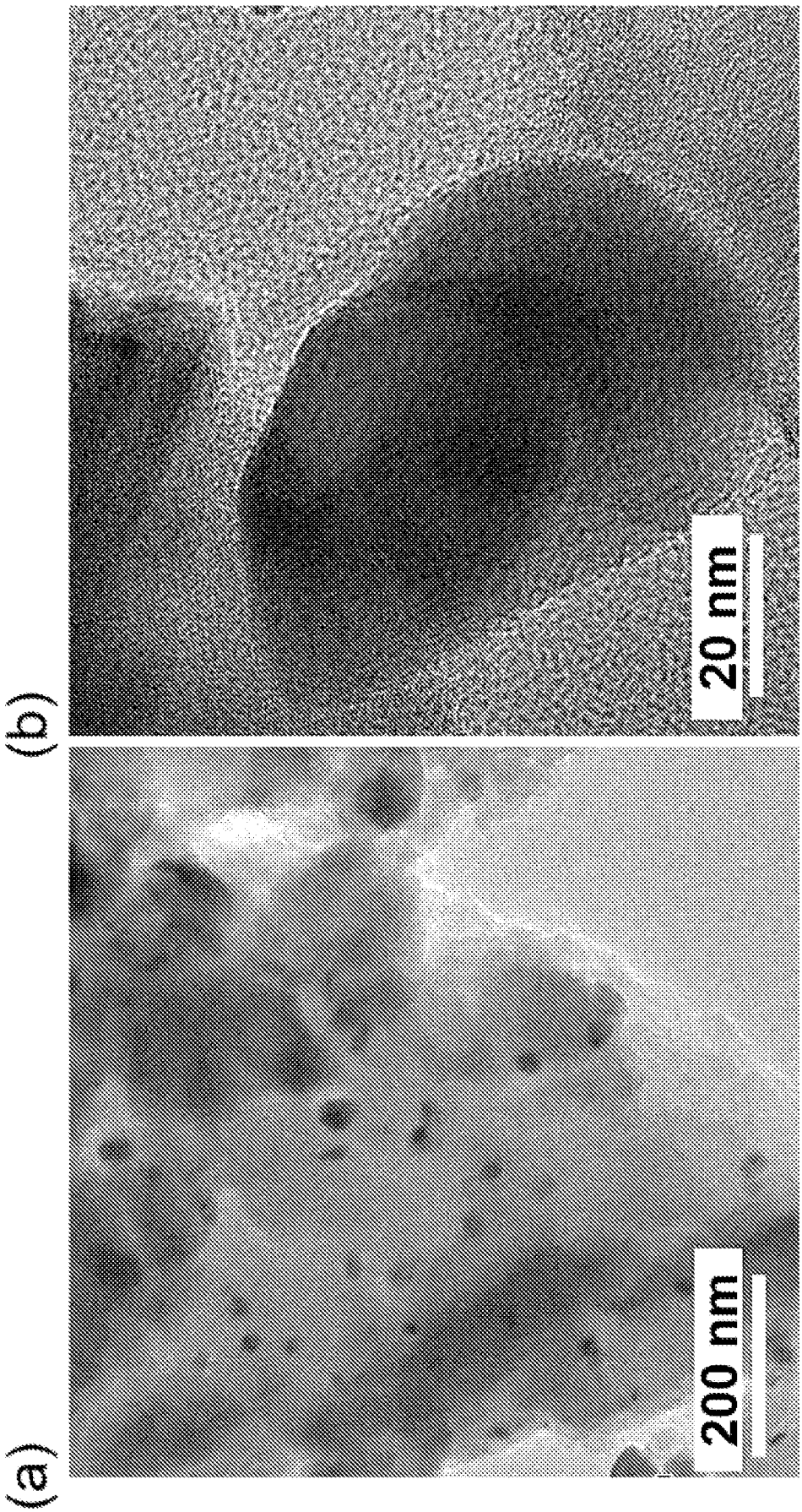

FIG. 14

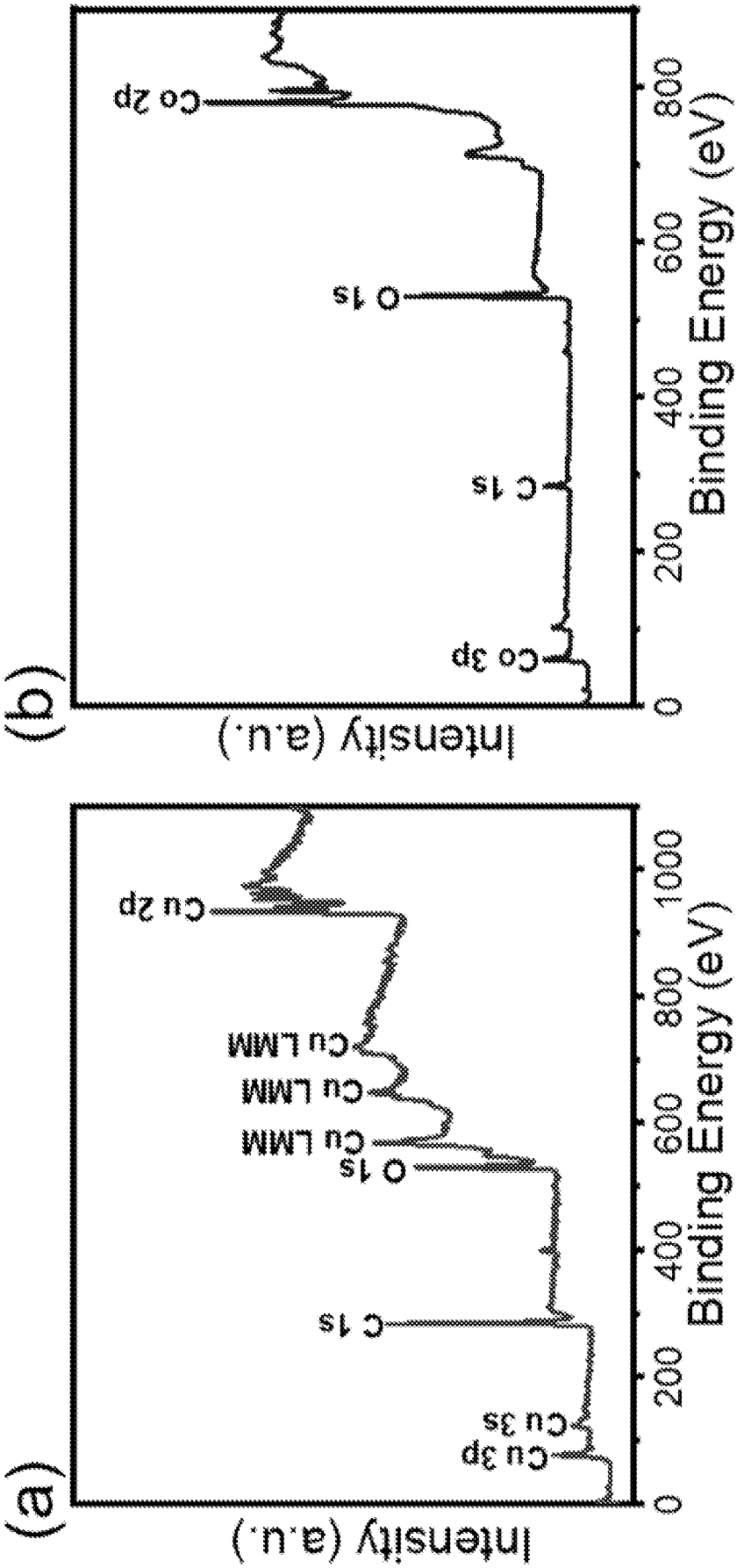
(a)
Intensity (a.u.)
Cu 3p
Cu 3s
C 1s
O 1s
Cu LMM
Cu LMM
Cu LMM
Cu 2p
0
200
400
600
800
1000
Binding Energy (eV)
(b)
Intensity (a.u.)
Co 3p
C 1s
O 1s
Co 2p
0
200
400
600
800
Binding Energy (eV)

FIG. 15

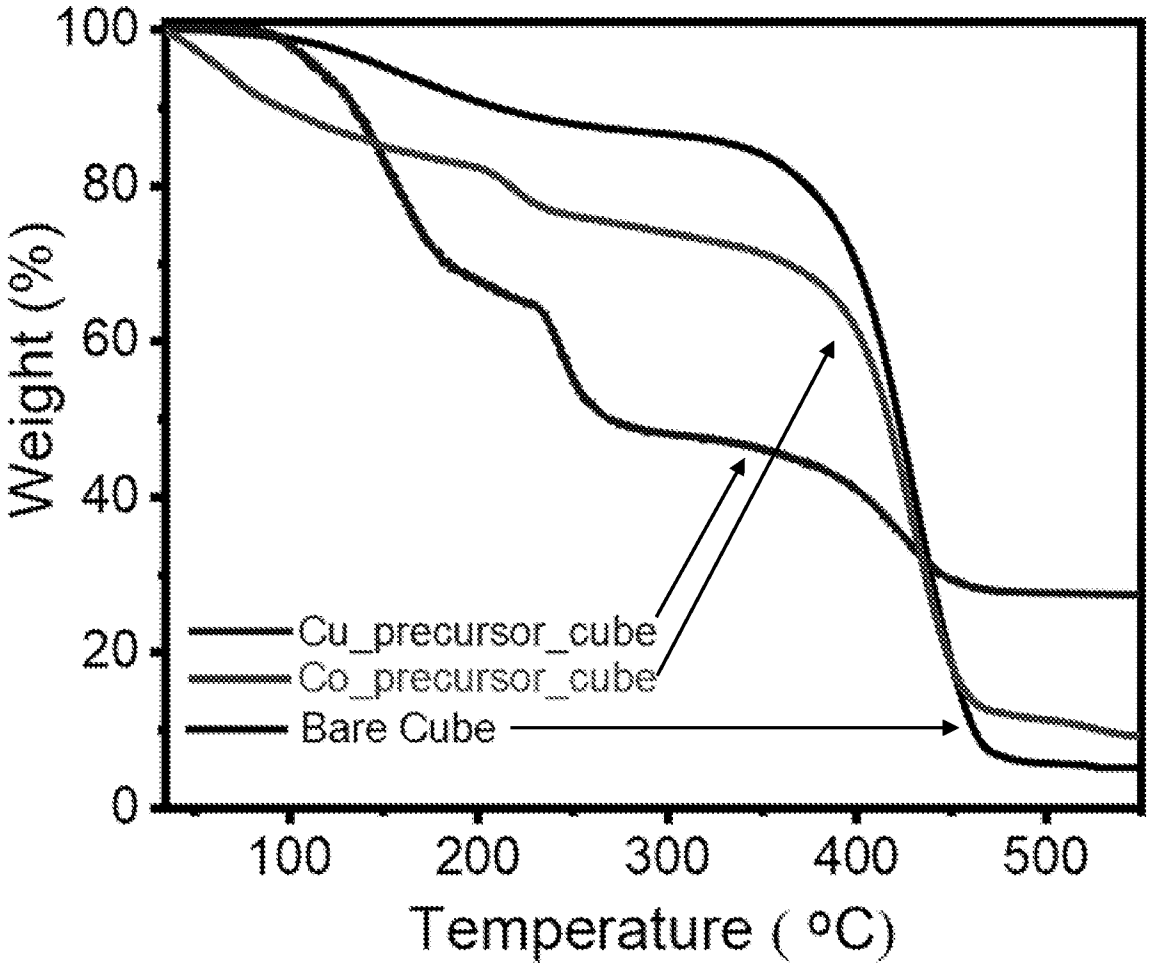
100
80
60
40
20
0
Weight (%)
100
200
300
400
500
Temperature (°C)
Cu_precursor_cube
Co_precursor_cube
Bare Cube

FIG. 16

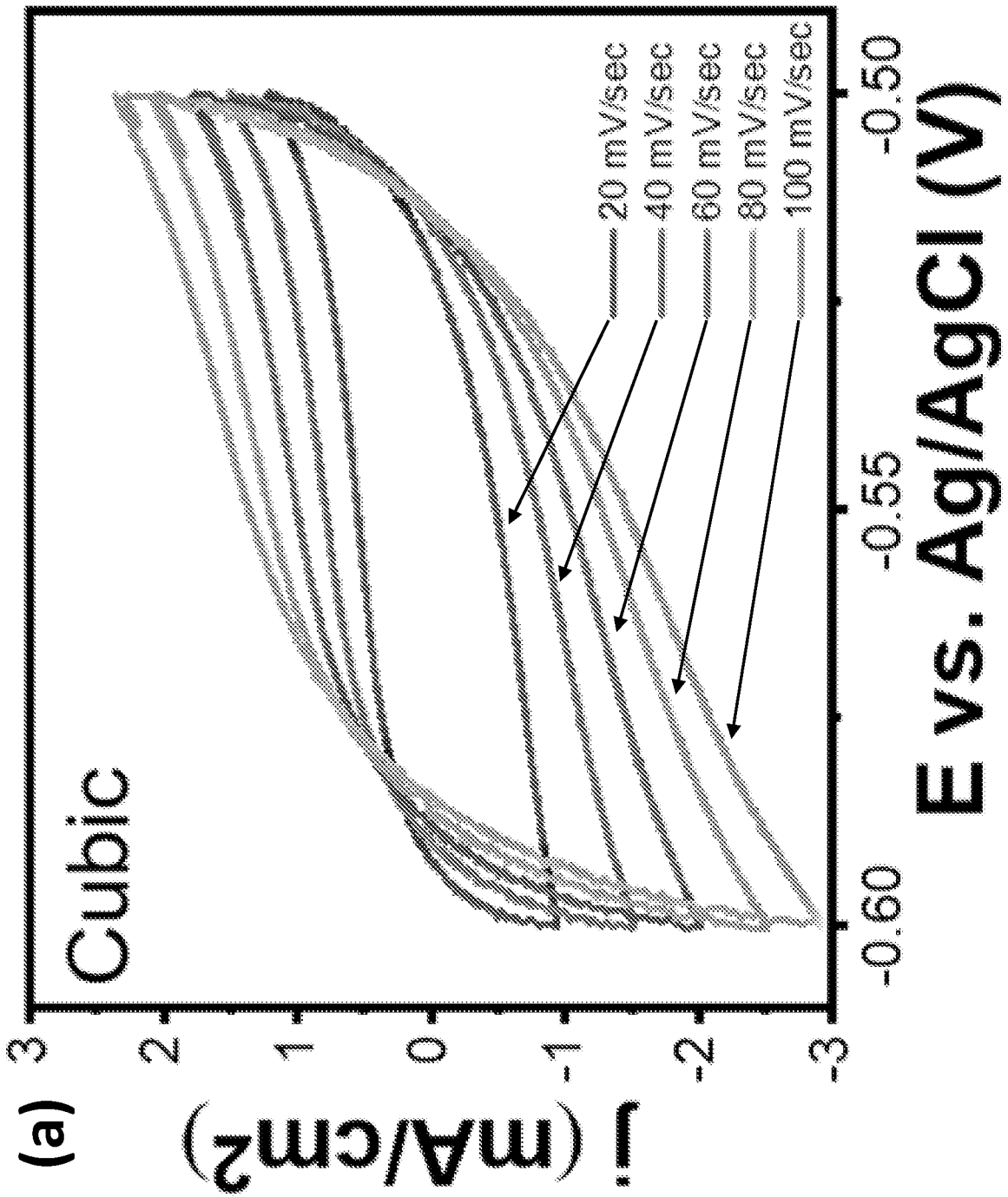
(a)
j (mA/cm2)
3
2
1
0
-1
-2
-3
Cubic
20 mV/sec
40 mV/sec
60 mV/sec
80 mV/sec
100 mV/sec
-0.60
-0.55
-0.50
E vs. Ag/AgCl (V)

FIG. 17

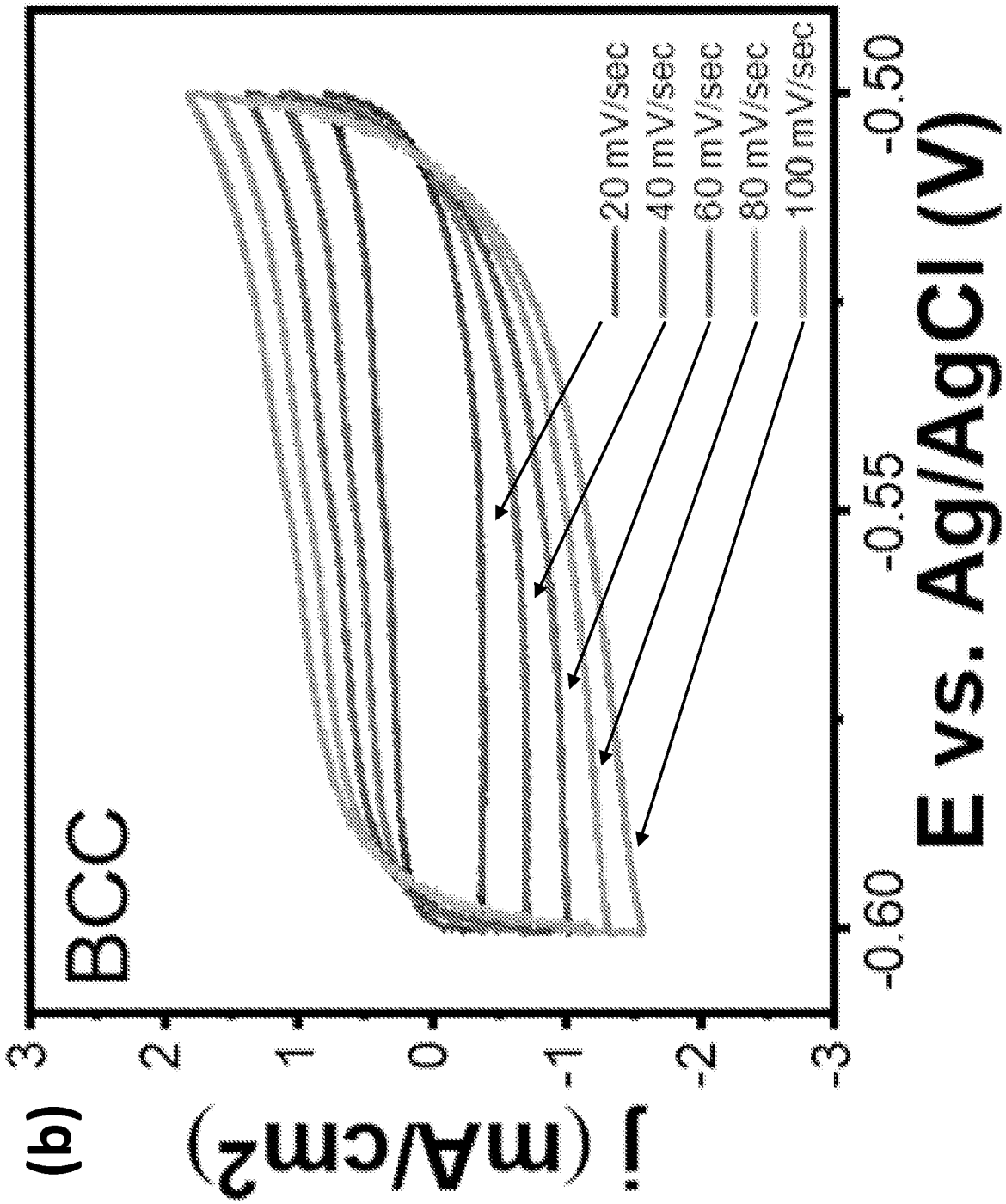

FIG. 17 (continued)

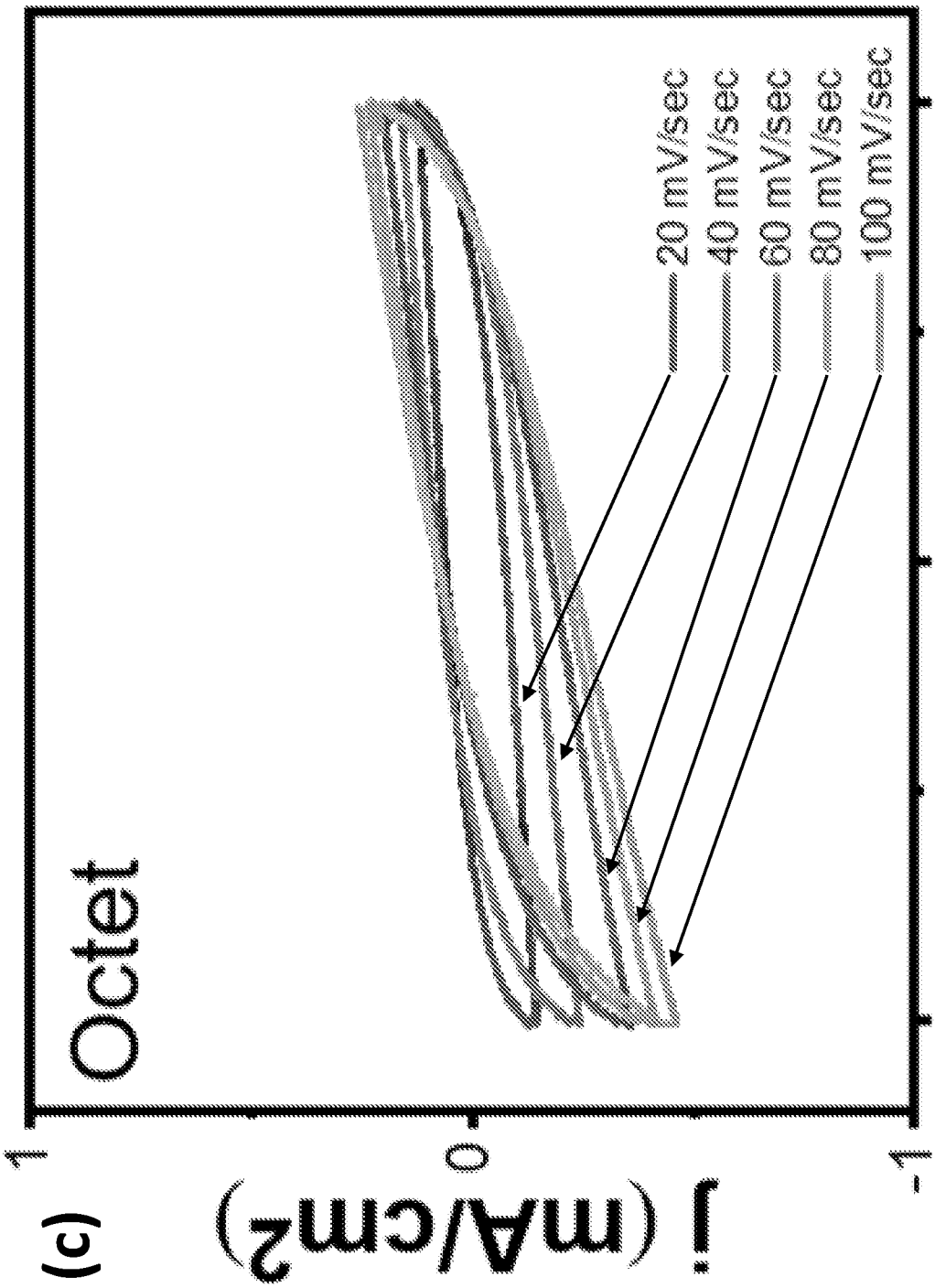

FIG. 17 (continued)

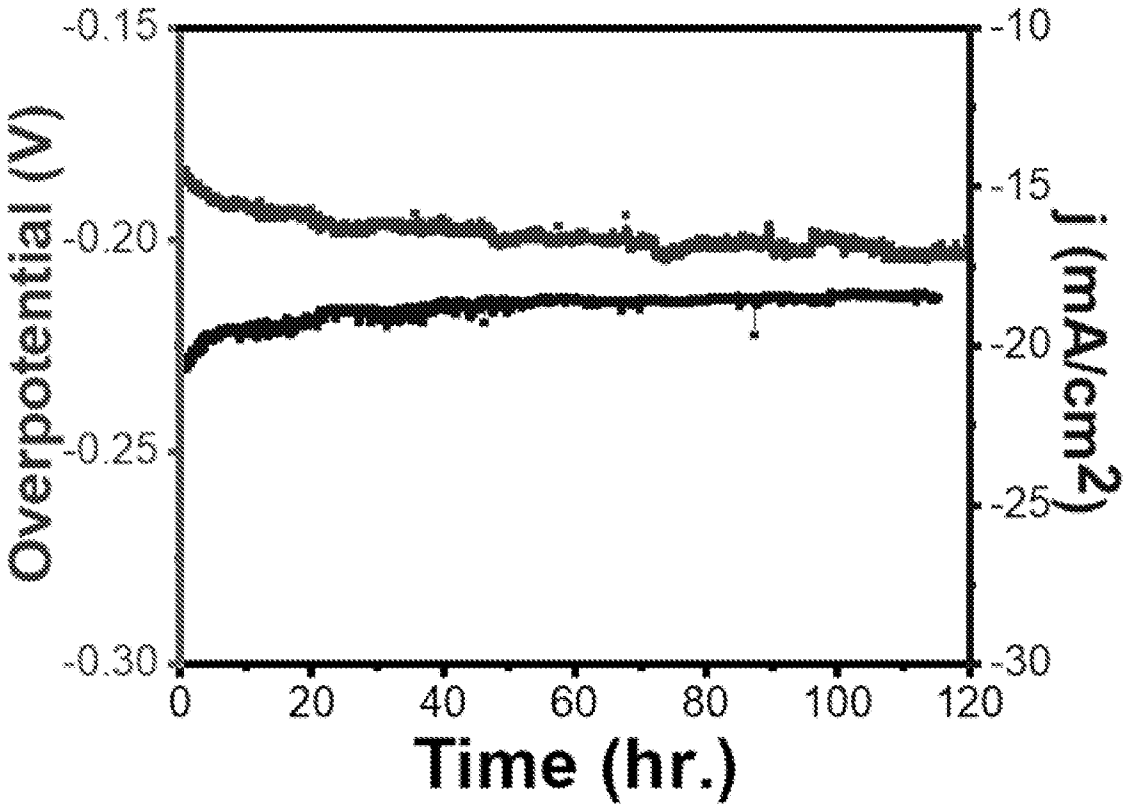
Overpotential (V)
-0.15
-0.20
-0.25
-0.30
j (mA/cm2)
-10
-15
-20
-25
-30
0
20
40
60
80
100
120
Time (hr.)

FIG. 18

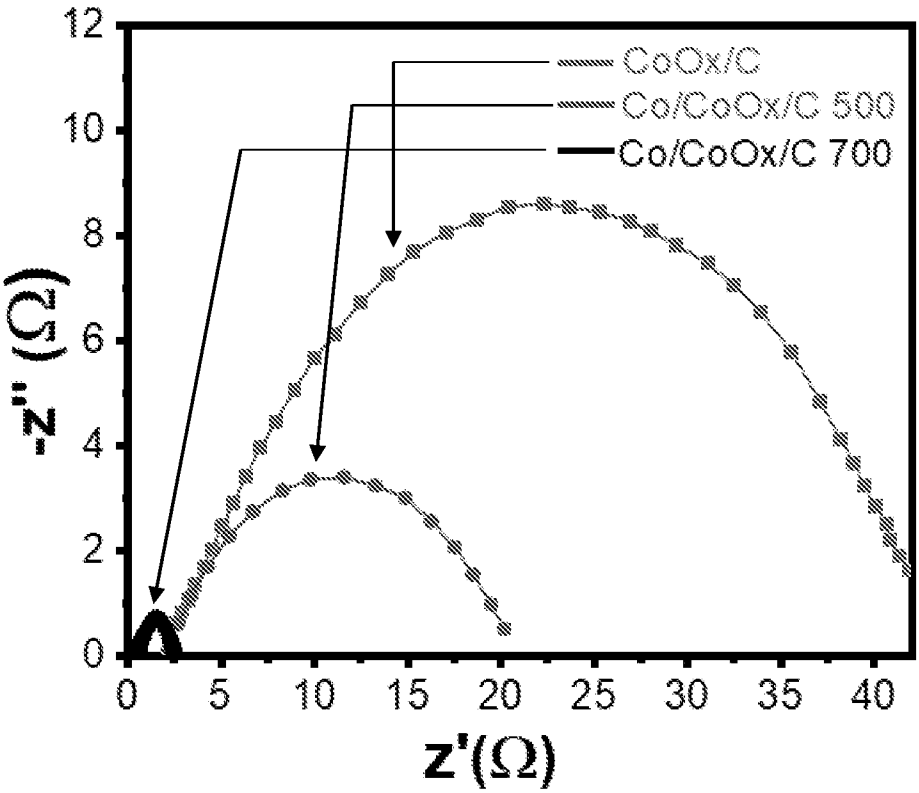
CoOx/C
Co/CoOx/C 500
Co/CoOx/C 700
-z'' (Ω)
0
2
4
6
8
10
12
0
5
10
15
20
25
30
35
40
z'(Ω)

FIG. 19

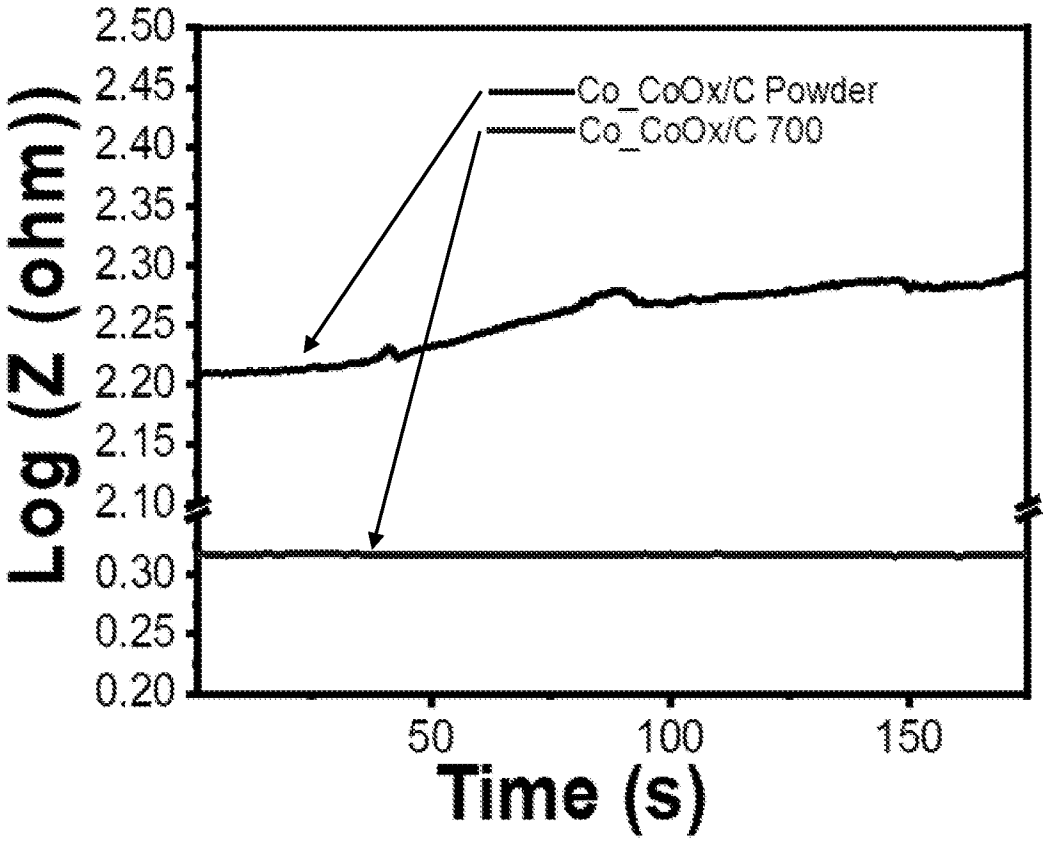
Log (Z (ohm))
2.50
2.45
2.40
2.35
2.30
2.25
2.20
2.15
2.10
0.30
0.25
0.20
Co_CoOx/C Powder
Co_CoOx/C 700
50
100
150
Time (s)

FIG. 20

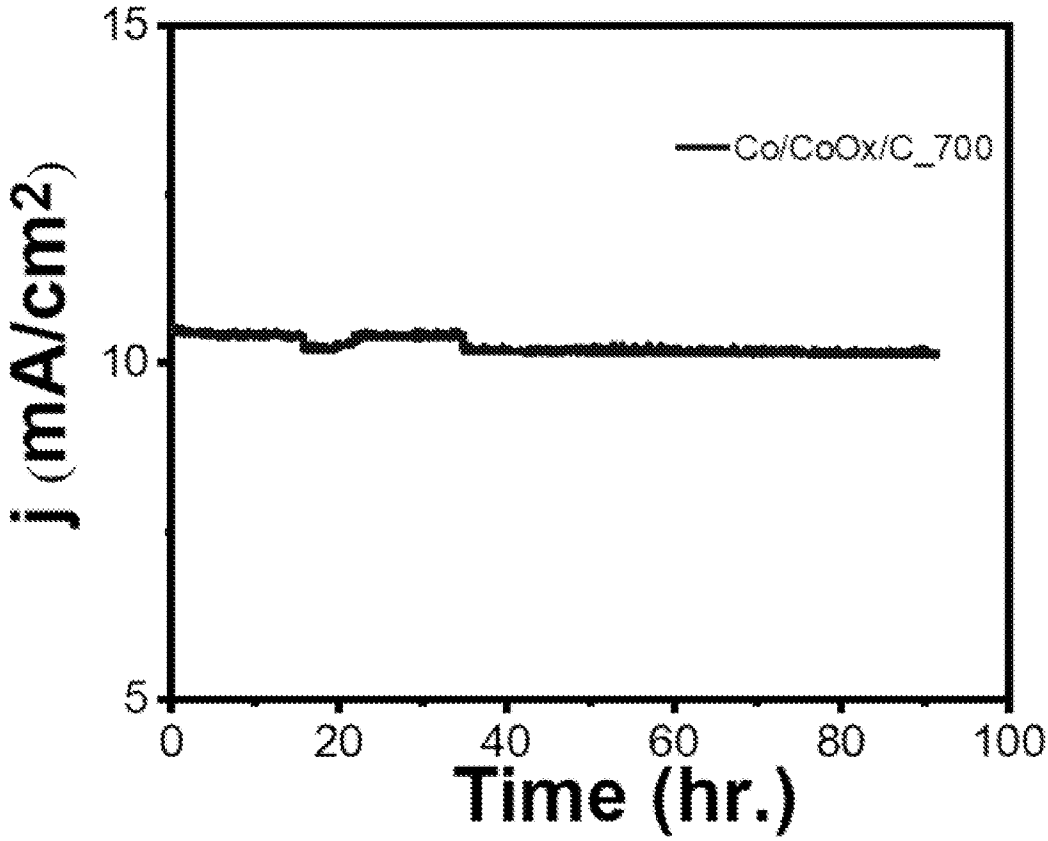
j (mA/cm2)
15
10
5
Co/CoOx/C_700
0
20
40
60
80
100
Time (hr.)

FIG. 21

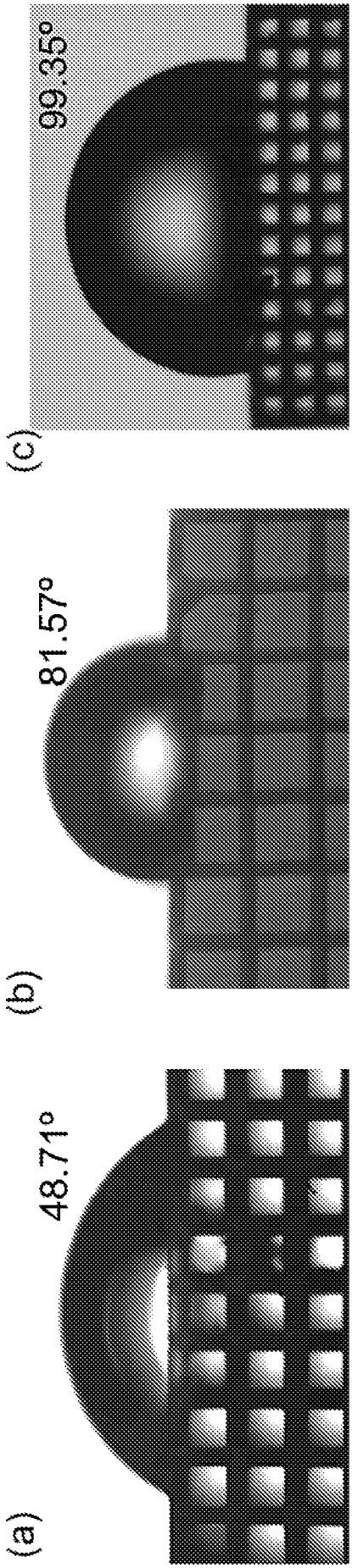

FIG. 22

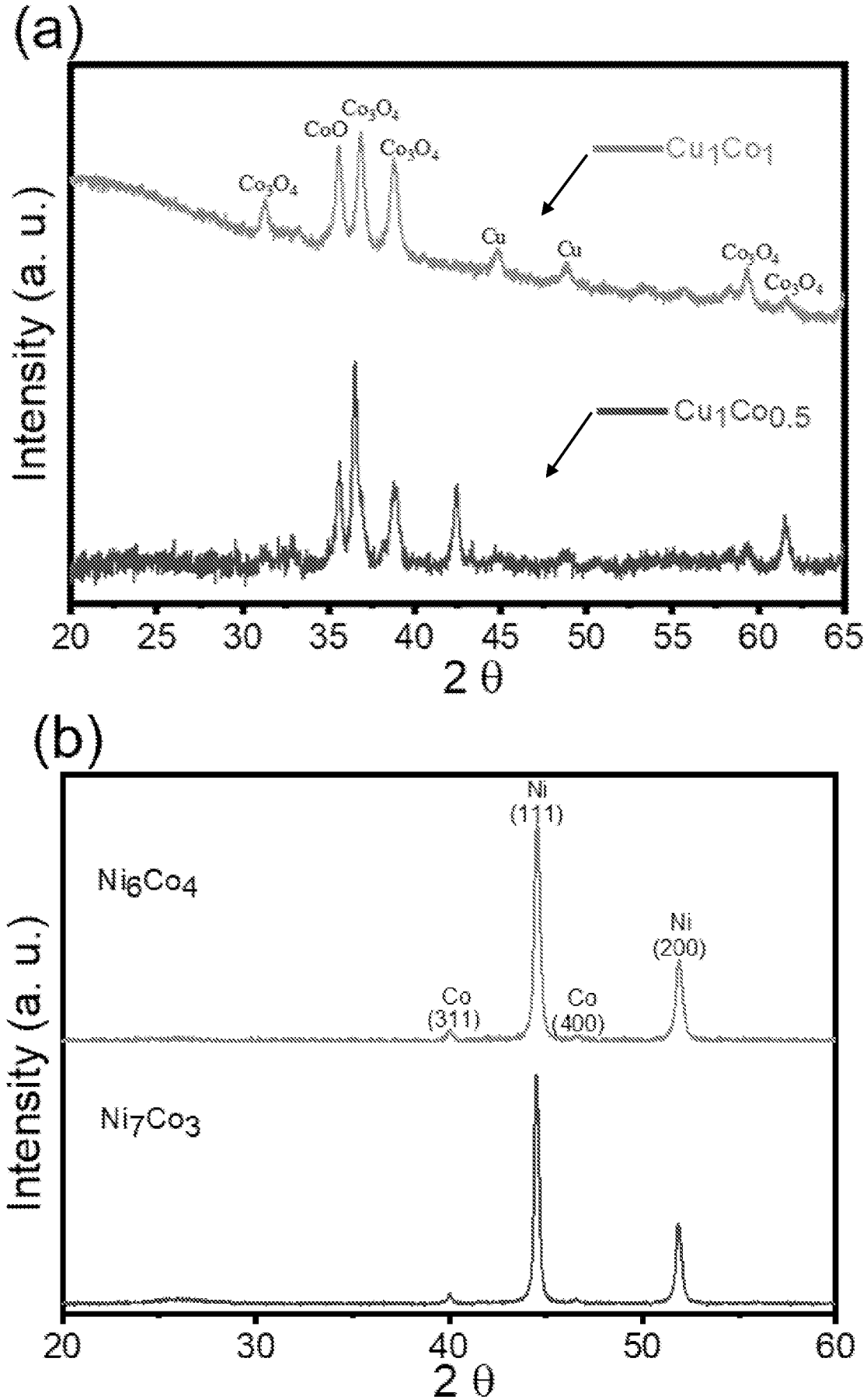
(a)
Intensity (a. u.)
Co_3O_4
CoO
Co_3O_4
Co_3O_4
Cu_1Co_1
Cu
Cu
Co_3O_4
Co_3O_4
$Cu_1Co_{0.5}$
20 25 30 35 40 45 50 55 60 65
2 θ
(b)
Intensity (a. u.)
Ni_6Co_4
Ni (111)
Ni (200)
Co (311)
Co (400)
Ni_7Co_3
20 30 40 50 60
2 θ

FIG. 23

Cu_1Co_1

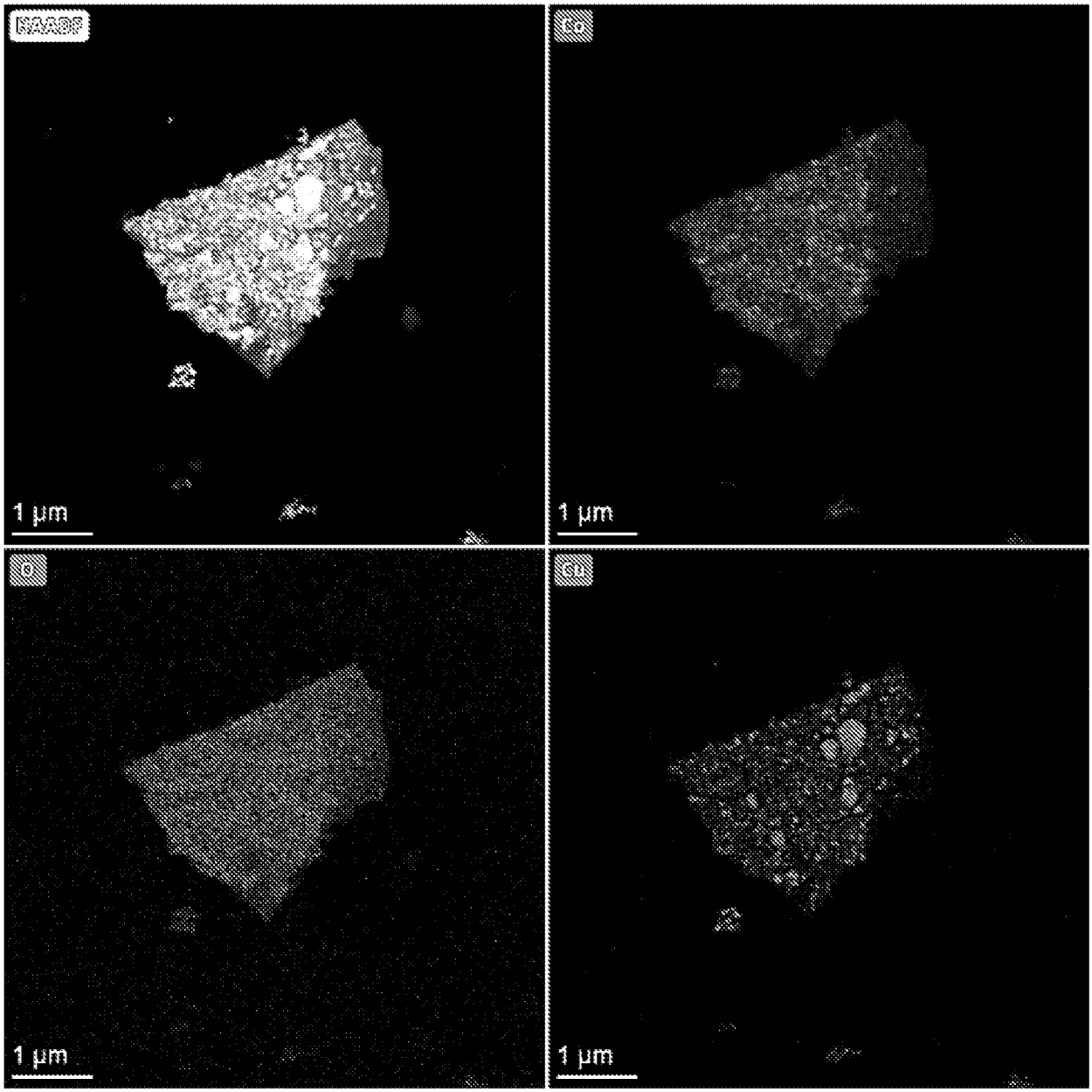

FIG. 24

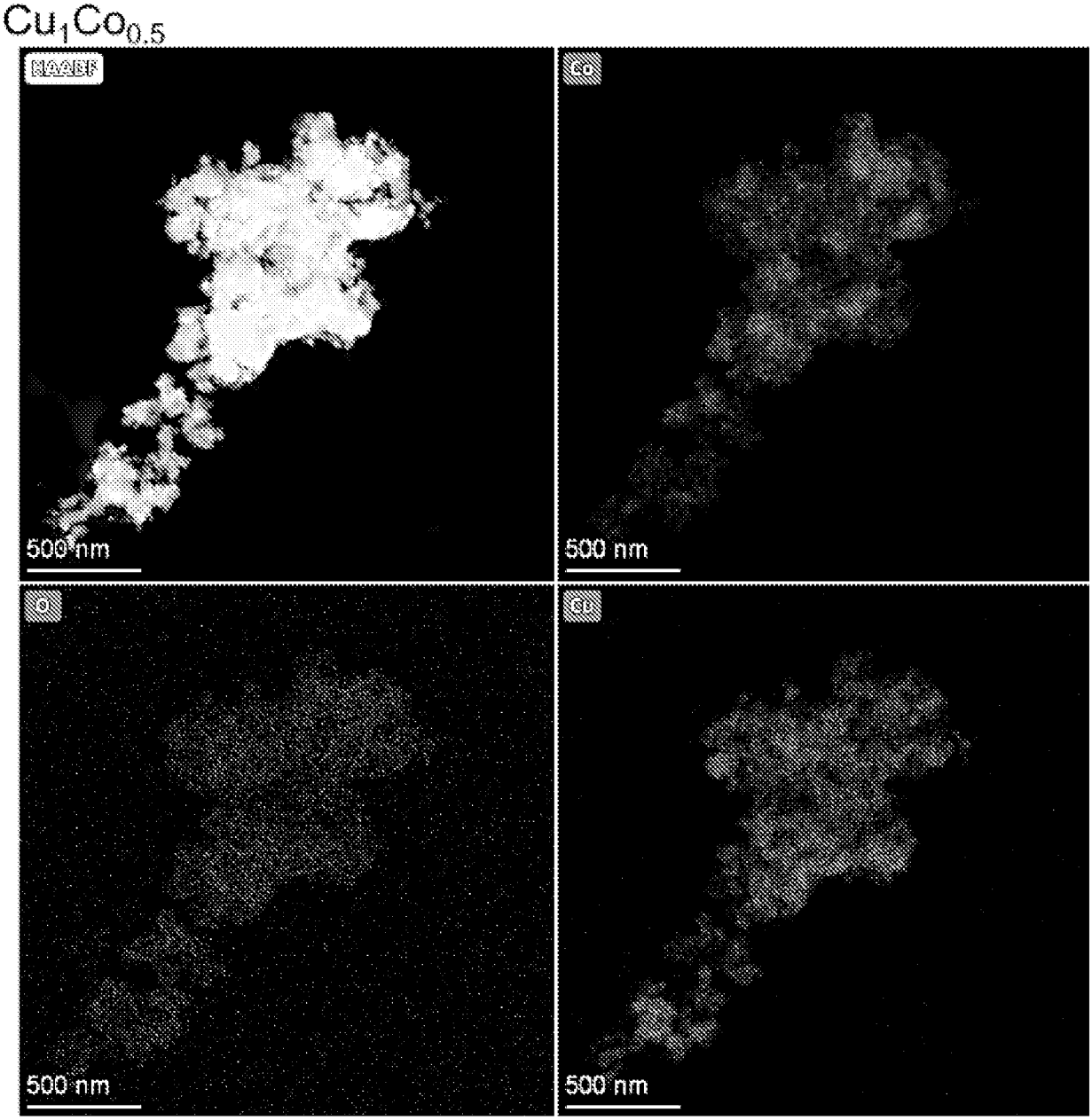

FIG. 24 (continued)

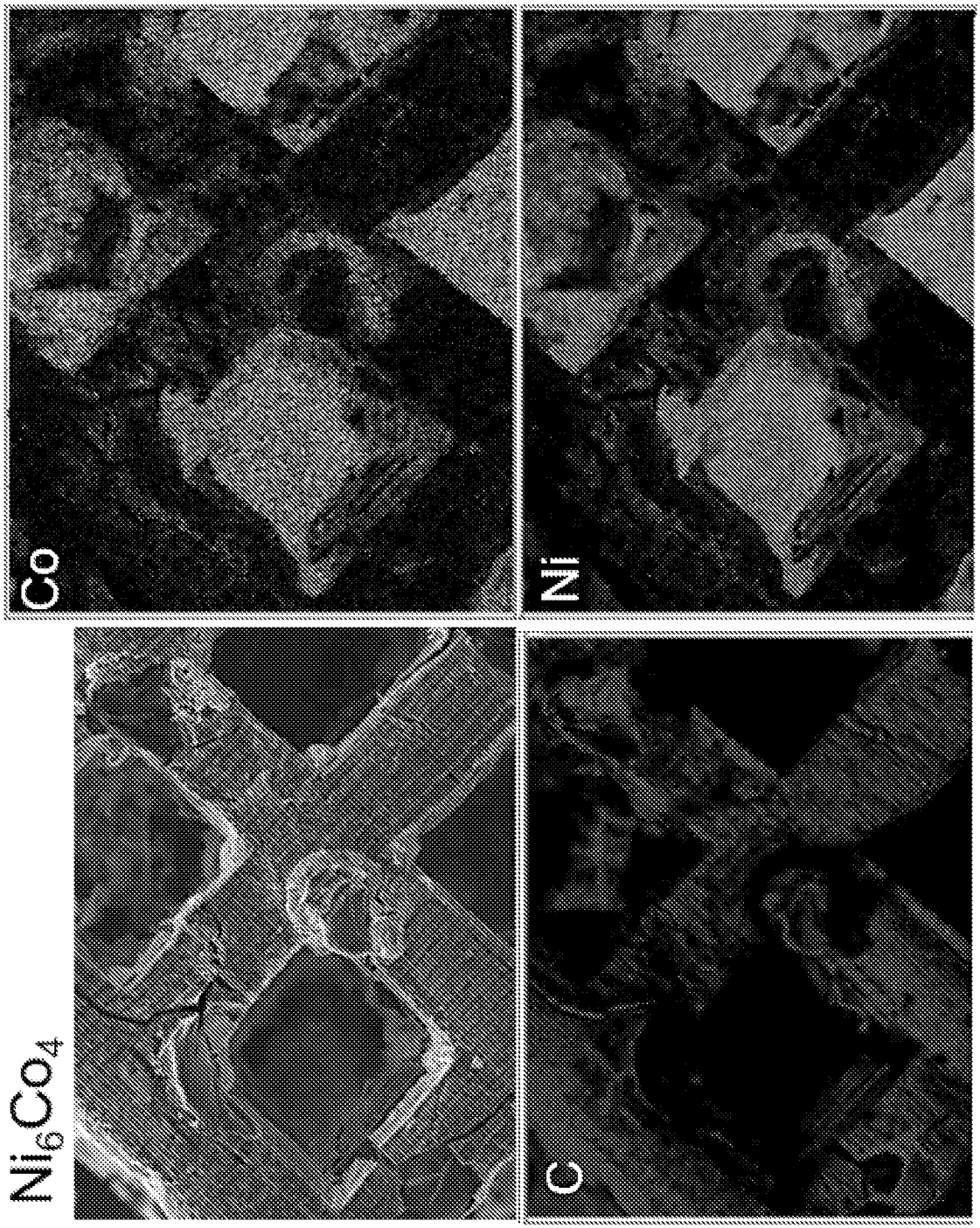

FIG. 25

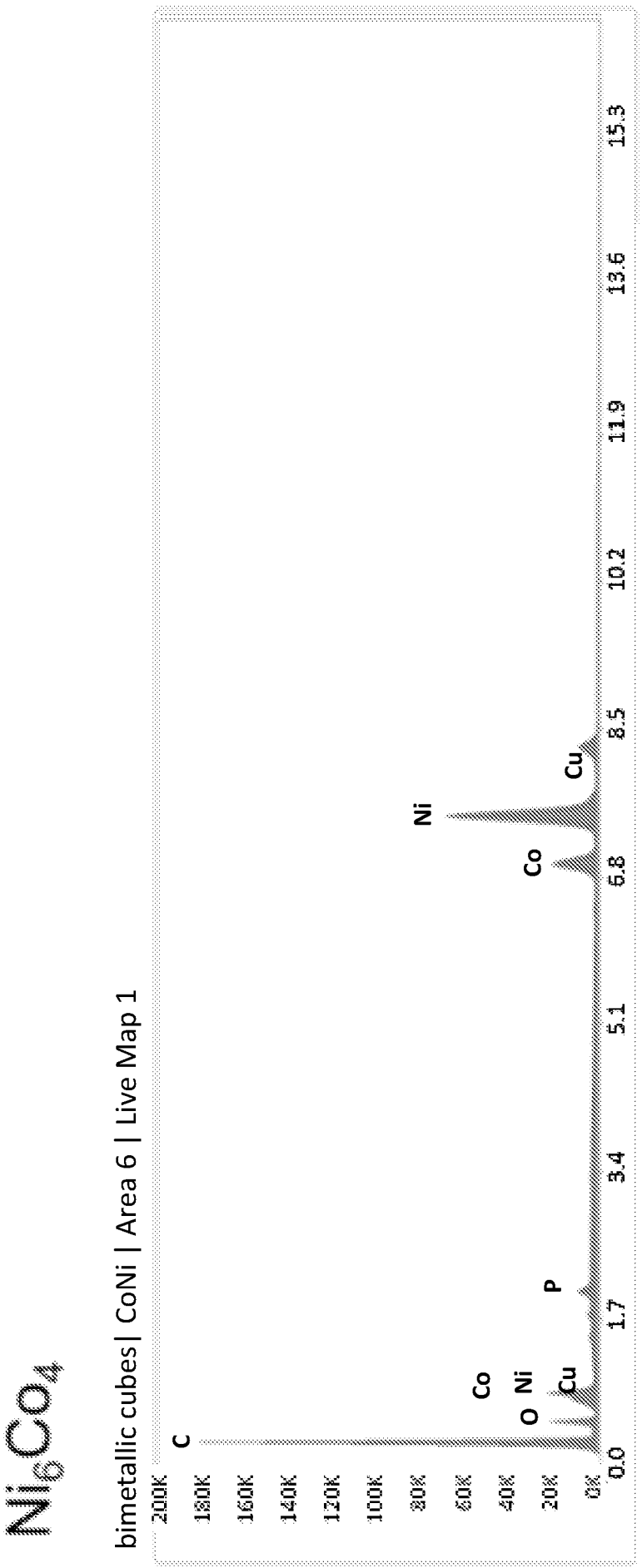

FIG. 25 (continued)

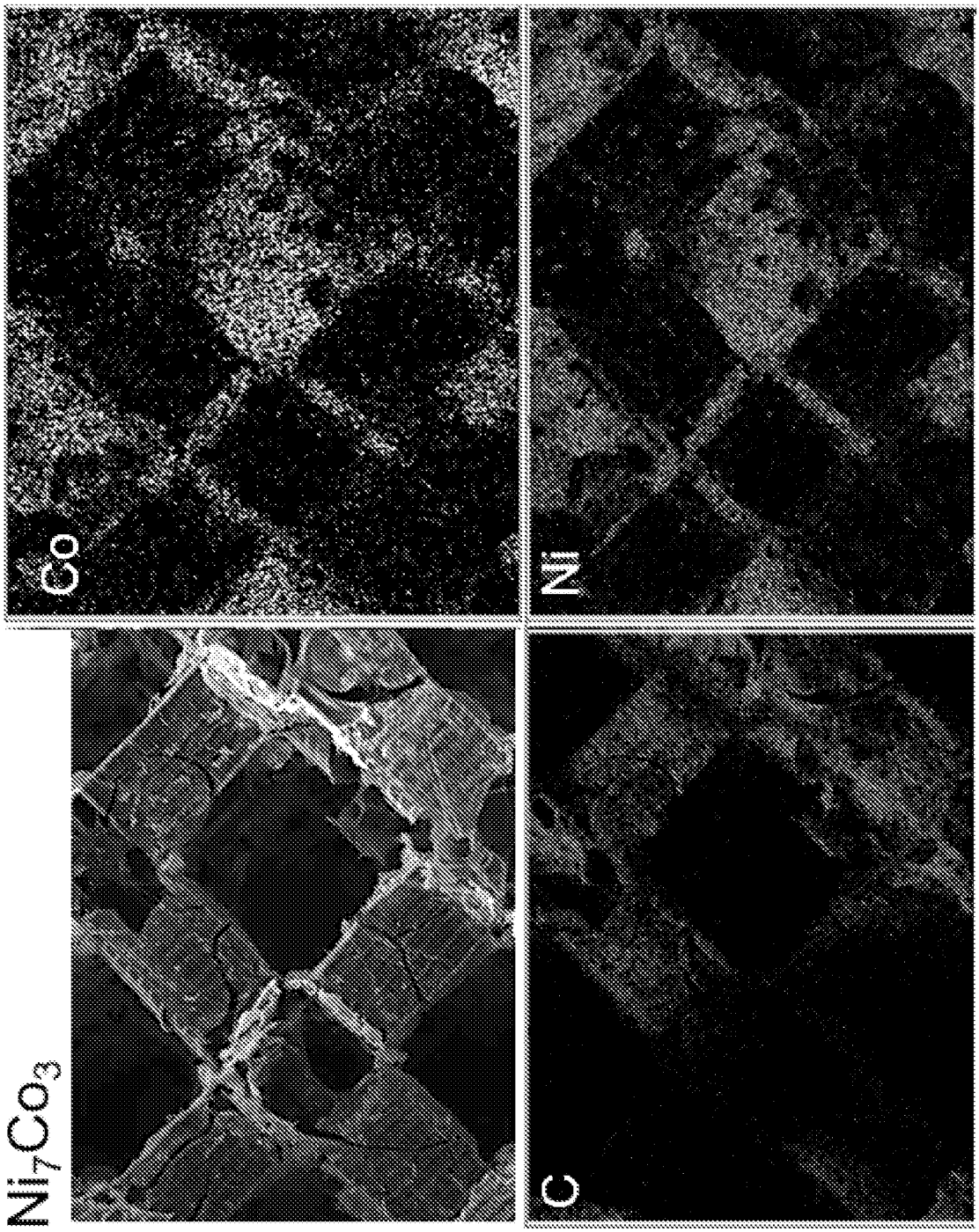

FIG. 25 (continued)

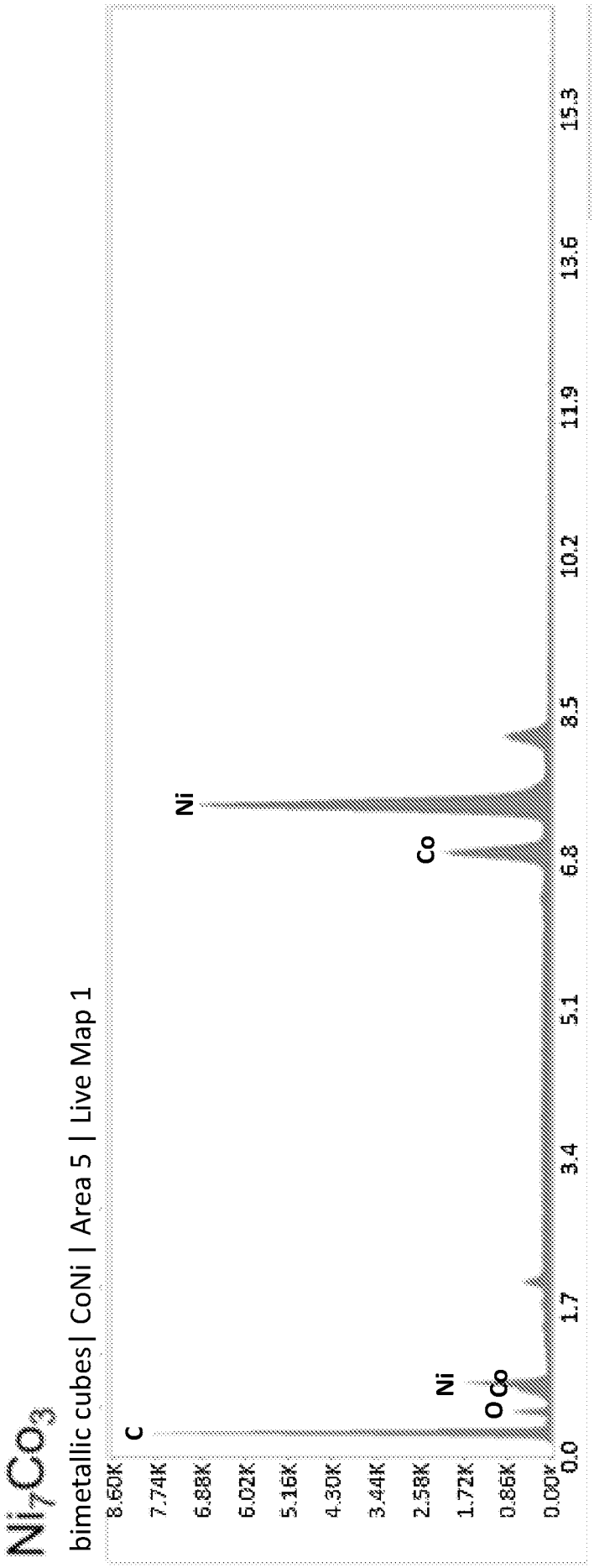

FIG. 25 (continued)

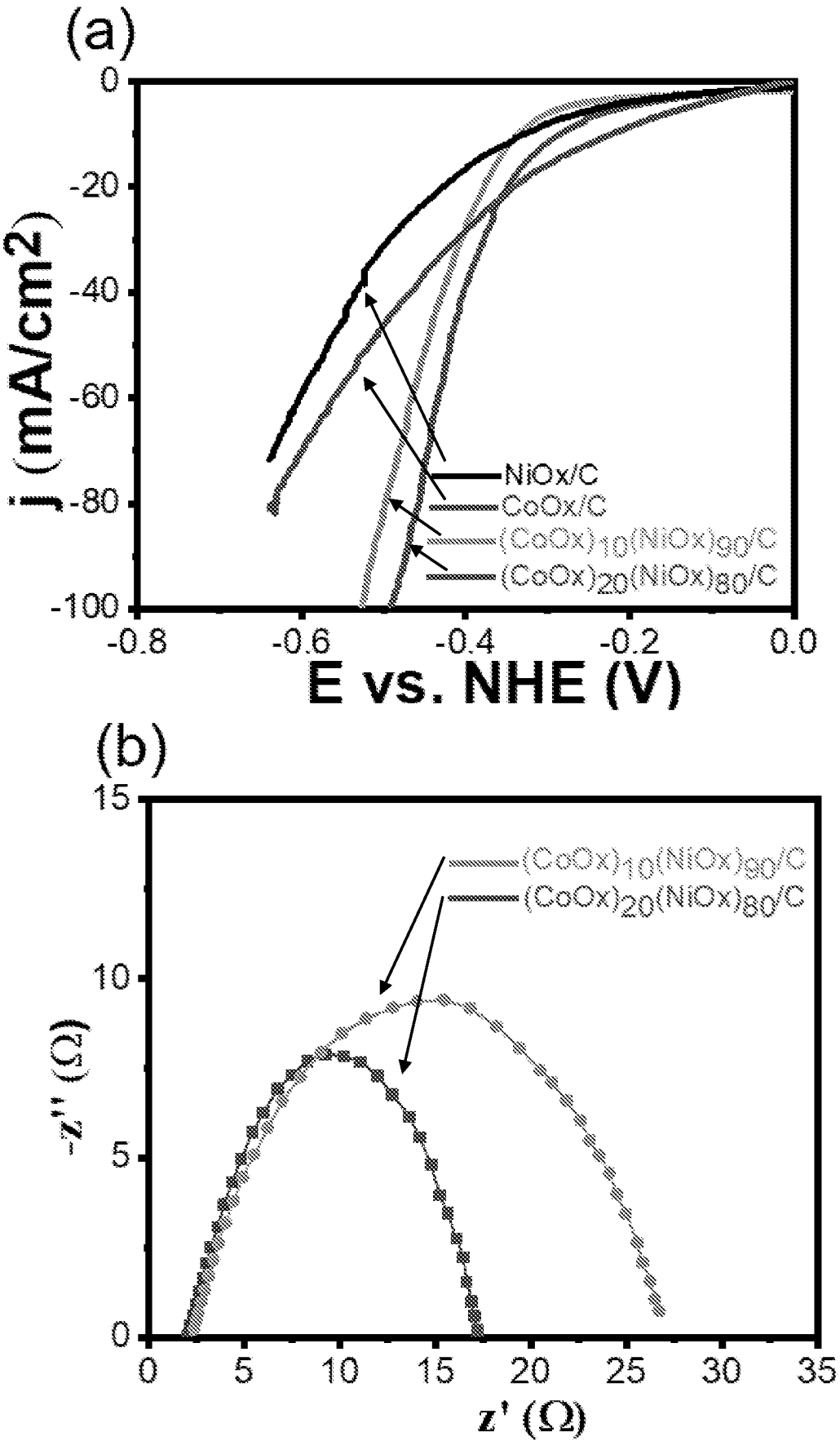
(a)
0
-20
-40
-60
-80
-100
j (mA/cm2)
-0.8
-0.6
-0.4
-0.2
0.0
E vs. NHE (V)
NiOx/C
CoOx/C
(CoOx)10(NiOx)90/C
(CoOx)20(NiOx)80/C
(b)
15
10
5
0
-z'' (Ω)
0
5
10
15
20
25
30
35
z' (Ω)
(CoOx)10(NiOx)90/C
(CoOx)20(NiOx)80/C

FIG. 26